Copyright Warning & Restrictions

The copyright law of the United States (Title 17, United States Code) governs the making of photocopies or other reproductions of copyrighted material.

Under certain conditions specified in the law, libraries and archives are authorized to furnish a photocopy or other reproduction. One of these specified conditions is that the photocopy or reproduction is not to be "used for any purpose other than private study, scholarship, or research." If a, user makes a request for, or later uses, a photocopy or reproduction for purposes in excess of "fair use" that user may be liable for copyright infringement,

This institution reserves the right to refuse to accept a copying order if, in its judgment, fulfillment of the order would involve violation of copyright law.

Please Note: The author retains the copyright while the New Jersey Institute of Technology reserves the right to distribute this thesis or dissertation

Printing note: If you do not wish to print this page, then select "Pages from: first page # to: last page #" on the print dialog screen

ABSTRACT

PARTICLE DEPOSITION FROM TURBULENT FLOW IN A DIVERGENT CHANNEL

by

Wai-Ting Huang

This dissertation presents a numerical analysis of particle deposition from a dilute gas-solid two-phase suspension in a divergent channel. The Lagrangian governing equations for particle motion include inertia force, viscous force, gravity force and image force from electrostatic charge on the particle. The incompressible two-dimensional turbulent flow field in a divergent channel is solved by employing a κ–ε modeling technique with FIDAP finite element CFD software. A computational procedure is developed to incorporate the flow field into numerical simulation of particle trajectories from which the fraction of deposition is determined. Several divergent channels (half divergent angles of 0°, 7.5°, 10° and 12.5°) coupled with the combination of dimensionless parameters (inertia parameter $0.01 \le S \le 100$, gravity parameter $0.01 \le G \le 100$ and charge parameter $0.00001 \le Q \le 10000$) are performed and the effects of these parameters on the deposition are determined. The mechanism of particle motion in a two-dimensional turbulent channel is understood from the analysis of particle trajectory and deposition.

PARTICLE DEPOSITION FROM TURBULENT FLOW IN A DIVERGENT CHANNEL

by
Wai-Ting Huang

A Dissertation
Submitted to the Faculty of
New Jersey Institute of Technology
in Partial Fulfillment of the Requirements for the Degree of
Doctor of Philosophy

Department of Mechanical Engineering

May 1997

APPROVAL PAGE

PARTICLE DEPOSITION FROM TURBULENT FLOW IN A DIVERGENT CHANNEL

Wai-Ting Huang

Dr. Rong Y. Chen, Disseration Advisor — Date
Professor of Mechanical Engineering and Associate Chairperson of the
Department of Mechanical Engineering, NJIT

Dr. John Droughton, Committee member — Date
Professor of Mechanical Engineering and Associate Chairperson of the
Department of Mechanical Engineering, NJIT

Dr. Ernest Geskin, Committee member — Date
Professor of Mechanical Engineering

Dr. Pushpendra Singh, Committee member — Date
Assistant Professor of Mechanical Engineering

Dr. Mengchu Zhou, Committee member — Date
Associate Professor of Electrical and Computer Engineering

BIOGRAPHICAL

Author: Wai-Ting Huang

Degree: Doctor of Philosophy

Date: May 1997

Undergraduate and Graduate Education:

- Doctor of Philosophy in Mechanical Engineering,
  New Jersey Institute of Technology, Newark, NJ, 1997
- Master of Science in Mechanical Engineering,
  New Jersey Institute of Technology, Newark, NJ, 1992
- Bachelor of Science in Mechanical Engineering,
  National Chung-Shin University, Tai-Chung, Taiwan, 1987

Major: Mechanical Engineering

To my parents and brothers for their patience and encouragement during these years.

ACKNOWLEDGMENT

The author will always remain indebted to his advisor, Professor Rong Chen, for his valuable suggestions, continuous guidance and supervision, and encouragement throughout this research.

The author wishes to express his sincere gratitude to Professor John Droughton, who has kindly read through the original manuscript and provided valuable suggestions. Also, many thanks are due to Professors Ernest Geskin, Pushpendra Singh and Mengchu Zhou for dedicating their time to serve as members of the committee.

The author is grateful to Professor Roman Dubrovsky for his constant assistance and advice during these years.

The author also appreciates the staff in the Department of Mechanical Engineering: Don Rosander and Jack Gidney for their time-to-time assistance.

Timely help and suggestions came from many good friends Wenlong Yao, Teng-Yao Hu, Frank Li, Ding Sun and S. Gorge.

Further acknowledgment is given to the Department of Mechanical Engineering of New Jersey Institute of Technology for the graduate assistantship and the opportunity of instructing courses during the academic years of 1993-1997.

TABLE OF CONTENTS

TABLE OF CONTENTS
(Continue)

TABLE OF CONTENTS
(Continue)

LIST OF TABLES

Table **Page**

LIST OF FIGURES

LIST OF FIGURES
(Continue)

NOMENCLATURE

C_D	Stoke's drag coefficient
Co	particle number density
d_p	particle diameter
f_x, f_y	image force components on a particle
F_D	viscous drag force
F_L	Saffman lift force
g	gravitational acceleration constant
G	Dimensionless gravity force parameter
h	half channel width at inlet plane
K	turbulence kinetic energy
K_m	correction factor for image force in a divergent channel
m_p	particle mass
n	number of image pairs
N	total number of image pairs
p	fluid pressure
q	electrostatic charge per particle
Q	dimensionless image force parameter
q_n	distance between the point charge to the primary image n
$q_{n'}$	distance between the point charge to the secondary image n'
Re	Reynolds number

NOMENCLATURE
(Contiune)

Re_p	Reynolds number of particle
S	dimensiionless inertia force parameter
t	time variable
T	dimensionless time variable
u,v	component of fluid velocity in x, y direction
u_p,v_p	component of particle velocity in x, y direction
u_o	fluid velocity at channel inlet
u', v'	flucturation velocity component of turbulent flow in x, y direction
U,V	dimensionless component of fluid velocity in X, Y direction
U_p,V_p	dimensionless component of particle velocity in X, Y direction
U_o	dimensionless fluid velocity at channel inlet
x_m	horizontal distance from the charge point to the center of image circle
x, y	horizontal and vertical coordinates
X, Y	dimensiomless horizontal and vertical coordinates
y_o	particle coordinate at inlet plane
y_l	particle coordinate at inlet plane where particles deposit on the lower wall
y_u	particle coordinate at inlet plane where particles deposit on the upper wall
Y_o	dimensionless particle coordinate at inlet plane
Y_l	dimensionless particle coordinate at inlet plane where particles deposit on the lower wall

NOMENCLATURE
(Contiune)

Y_u	dimensionless particle coordinate at inlet plane where particles deposit on the upper wall
α	turbulence kinetic energy constant
δ	characteristic length for turbulence dissipation
ε	turbulence dissipation
ε_o	permitivity of free space
θ	half divergent angle of a divergent channel
ρ	gas density
ρ_p	particle density
α_o	angle between the center line and the line from the charge point to the center
α_n	half angle subtended by the chord connecting the charge point to image n
$\alpha_{n'}$	half angle subtended by the chord connecting the charge point to image n'
β_n	angle between y-axis and the chord connecting the charge point to the primary image n
$\beta_{n'}$	angle between y-axis and the chord connecting the charge point to the secondary image n'
μ	viscosity of fluid
υ	kinematics viscosity

CHAPTER 1

INTRODUCTION

1.1 Practical Applications and General Introduction

Deposition of particles or aerosols from a fluid-solid suspension flow is an important aspect in numerous industrial, geophysical and biomedical applications such as semiconductor manufacture, air pollution control, and pharmaceutical processes. Some typical examples are:

Clean room technique: Many manufacturing industries including semiconductor, aerospace devices, optical instruments, and pharmaceutical industries require a low contaminant environment. Particulate contamination has a significant impact on both production rate and product quality due to the fact that these products are extremely sensitive to fine particles or aerosols. In order to improve the quality of clean rooms, the identification of contaminant particles, the proper control approach and removal methods have attracted much attention gradually.

Dust precipitators: Devices of dust collection are made for particulate control in a very wide variety of applications from air pollution control in the cement industry to family health control of allergy. The mechanical collectors make use of gravitational or inertial separation such as gravity or momentum settlers and cyclones. Electrical precipitators use electrical forces to enhance the deposition of particles and aerosols. Cartridge collectors use plated filters or fibrous mats for collection of contaminant particles. Wet process collectors and wet scrubbers use water to saturate the gas stream and encapsulate the particles in water.

Fluidized beds: A fluidized bed is a volume of inert particles, such as fine coal, which are supported by a grate-like air distributor. When air is blown through the bed mass, the solid particles are lifted and suspended by this air stream such that particles can move freely and the bed behaves like a fluid. Fluidized beds are widely used in chemical industries and pharmaceutical processes to promote proper heat transfer, chemical reactions or species mixture.

Spray injection: Combustion of powdered coal is used in many power plants world wide. This well-known technique involves injecting the fine coal powder into a combustion chamber by means of a carrier gas. The efficiency of power plants and the exhausting air pollution control rely on the procedure of introducing a gas-solid suspension flow. Dispersal of pesticides for agricultural purposes or public health applications sprays usually utilize two phase flows in the form of sprays of aerosols or suspended fine particles.

The knowledge of behavior of suspended particles in gas-solid two phase flows is important and it has been studied by many researchers for many years. In the applications mentioned above, particle movement in a gas stream is involved and usually accompanied by particles depositions upon surfaces bounding the gas stream. Typical cases in which particles depositions play an important role are air pollution control and clean room technique. Due to increasingly strict environmental regulations in reducing health hazards and nuisance dust, and preventing pollution like acid rain, the removal of particles and aerosols from gas-solid two phase flows has become a matter of importance and necessity.

Another important subject regarding particles behavior in gas-solid two-phase flow is turbulence. Turbulence usually occurs in industrial and engineering applications. For example, although in a clean room the typical mean air velocity is about 0.5 m/sec which

can be considered vertical laminar flow", the movements of people and machines can produce turbulence [1]. The exhaust gas stream from the boiler system in a power plant using coal is usually at high velocity so that it is considered as a turbulent flow from which the contaminant particles must be removed for the sake of air pollution control. Therefore the understanding of particulate behavior in a turbulent flow has become an essential topic in practical applications.

1.2 Fundamental of Turbulence

A typical description for turbulence is: a spatially varying mean flow with superimposed random fluctuations which are self-sustaining and enhance mixing, diffusion, entrainment and dissipation. An incompressible turbulent flow can be considered in two parts, the mean and the fluctuation [2]. For an arbitrary field variable q, its mean value is defined as

$$\bar{q} = \frac{1}{\delta t}\int_{t}^{t+\delta t} q\,dt \tag{1.1}$$

where the averaging time δt is long compared with the time scale of the turbulent motion. In transient problems δt has to be small compared with the time scale of the mean flow motion. Then variable q is decomposed as

$$q = \bar{q} + q' \tag{1.2}$$

where $\bar{q}$ represents the mean and q' represents the fluctuation associated with turbulence.

This decomposition is directly applied to the incompressible continuity equation and the nonlinear Navier-Stokes equation. When the time average is taken, the continuity and Navier-Stokes equations become

$$\frac{\partial u}{\partial x} + \frac{\partial v}{\partial y} + \frac{\partial w}{\partial z} = 0 \tag{1.3}$$

$$\rho \frac{D\overline{V}}{Dt} + \rho \frac{\partial}{\partial X_j}\left(\overline{u_i u_j}\right) = \rho g - \nabla \overline{p} + \mu \nabla^2 \overline{V} \tag{1.4}$$

If the time average has not been taken, one more equation appears

$$\frac{\partial u'}{\partial x} + \frac{\partial v'}{\partial y} + \frac{\partial w'}{\partial z} = 0 \tag{1.5}$$

It has shown that the incompressible continuity equation will be satisfied by the mean and fluctuating velocity components separately. Then the mean momentum equation is complicated by a new term which involves the turbulent inertia tensor $\overline{u'_i u'_j}$. This new term is never negligible in any turbulent flow and causes some analytic difficulties.

By introducing a stress term τ_{ij} for the turbulent inertia terms, equation (1.3) can be written as

$$\rho \frac{D\overline{V}}{Dt} = \rho g - \nabla \overline{p} + \nabla \cdot \tau_{ij} \tag{1.6}$$

where

$$\tau_{ij} = \mu\left(\frac{\partial u_i}{\partial x_j} + \frac{\partial u_j}{\partial x_i}\right) - \rho\overline{u'_i u'_j} \tag{1.7}$$

Laminar Turbulent

Then the energy equation for an incompressible flow with constant properties has been dealt with by the same manner and will become

$$\rho c_p \frac{D\overline{T}}{Dt} = -\frac{\partial}{\partial x_i}\left(q_i\right) + \overline{\Phi} \tag{1.8}$$

where the total-dissipation function $\overline{\Phi}$ is

$$\overline{\Phi} = \frac{\mu}{2}\overline{\left(\frac{\partial \overline{u}_i}{\partial x_j}+\frac{\partial u'_i}{\partial x_j}+\frac{\partial \overline{u}_j}{\partial x_i}+\frac{\partial u'_j}{\partial x_i}\right)^2} \tag{1.9}$$

and the total-heat-flux vector q_i, including molecular flux and turbulent flux, is

$$q_i = \underset{\text{Laminar}}{-k\frac{\partial \overline{T}}{\partial x_i}} + \underset{\text{Turbulent}}{\rho c_p \overline{u'_i T'}} \tag{1.10}$$

In a two-dimensional turbulent-boundary-layer flow, the dissipation function reduces approximately to

$$\overline{\Phi} \approx \frac{\partial \overline{u}}{\partial y}\left(\mu\frac{\partial \overline{u}}{\partial y} - \rho\overline{u'v'}\right) \tag{1.11}$$

Equations (1.3), (1.6), (1.7), (1.8), (1.9) and (1.10) are Reynolds-averaged basic differential equations for turbulent mean continuity, mean momentum, and mean thermal energy.

1.3 Fundamental of Particle Dynamics

1.3.1 Basic Mathematics of Particle Dynamics

From the mathematical point of view, there are two approaches to analyze particle dynamics. The first one is the Lagrangian approach that treats the dynamics of one single particle by a trajectory method and extends to a multiple particles system in a analogous manner. The general equation of motion is based upon an essential application of Newton's second law:

$$F = ma$$

where F includes all forces including viscous drag forces due to fluid, buoyancy and gravity forces, pressure gradient, and so on, m is the mass of a particle and a is the acceleration. This method had been derived in the 19^{th} century by Basset et al which has been widely studied. In this analysis the governing equations of particle dynamics are derived from Newton's second law and presented in detail in chapter three.

The second approach is the Eulerian method that considers the particulate phase as continuous and, after choosing a proper origin of coordinates, applies an intergal balance in order to derive the field and constitutive equations as functions of position and time, not to follow any specific particle path. This method which considers continuum mechanics of multiphase flow has been used since 1960.

Recently both methods have been studied intensively. Gas-solid two-phase flows involve many different phenomena such as particle-fluid interaction, particle-particle interaction, particle-wall interaction and the combined effects of existing force fields. The significance and magnitude of these effects vary in relation to each other. Therefore these two approaches are restricted to certain classes of applications. For instance, the solution for the motion of a single particle is not appropriate to determine the behavior of a group of particles within a limited domain. On the other hand, the approach of continuum mechanics can only be applied for the situation with valid continuum approximation, i.e., for small particle size, low particle inertia, high particulate concentration and negligible external force field. It cannot trace the trajectory of a single particle. It gives a general phase solution of configuration of multiphase flow.

1.3.2 Basic Physics of Particle Dynamics

The range of particle size of interest in gas-solid two phase flow varies from sub-micrometer to almost a millimeter. Both materials of composition and sources producing particles are factors in the determination of the particle size. Some typical example are shown in table 1-1.

Table 1.1 Range of aeroaol particle size

Material	Tobacco smoke	Oil smoke	Fog	Coal dust	Fly-ash
Approximate size (μm)	0.01-1	0.03-1	2-80	1-100	1-200

Table 1.1 shows that although the tobacco smoke and fly-ash of burned cigarette can be produced from the same source, their sizes are very different due to their different materials of composition.

The particulate shape is another important matter when particle size is the concern. In general, the particulate shape is not spherical. However, in this study the particles are considered as smooth, spherical, inert and homogeneous for the near thermodynamic equilibrium of particles with their surrounding. The particle concentration is far less than the gas molecule concentration, i.e., 10^5 per cubic centimeter, for a dilute two-phase flow. Some orders of magnitude for parameters of airborne particles in the atmosphere are shown in table 1.2.

The subscript p represents particle and subscript g represents gas, and d_p represents the diameter of the particle. In general, a particle is much larger than a gas molecule, i.e., the size ratio $d_p/d_g > 1$ and the mass ratio $m_p/m_g >> 1$.

Table 1.2 Fluid dynamic parameters of aerosol particle

	Airborne aerosol particle	Air at sea level
Number density per cubic centimeter	1.0E02 - 1.0 E05	1.0E19
Particle radius (cm)	1.0E-6 - 1.0E-3	1.9E-8 (N_2)
Particle mass (g)	1.0E-18 - 1.0E-9	4.73E-23
Particle charge (units of elementary charge)	0 - 1.0E2	weakly ionized single charge
Mean velocity (cm/sec)	1.0E-2 - 1.0E03	0 - 1.0E03
Characteristic length (L_i)	$L_p \approx d_p$	Flow geometry

1.4 The Theme and Summary of this Study

The motive of this study is to obtain knowledge of particulate behavior in a turbulent gas-solid two-phase flow by numerical analysis of the particle deposition on surfaces of a channel due to the combination of effects of gravity, particle inertia, flow viscosity and electrostatic image forces under a wide variety of situations. Due to the complexity of particle deposition phenomenon, the complete mechanism of the particulate phase has to be investigated, the significance of involved parameters has to be studied, and a mathematical model to simulate the fluid flow and particles deposition has to be built.

An incompressible, two-dimensional turbulent flow is taken into consideration with a dilute suspension of micro-size particles. Due to the fact that many practical applications of particles suspension have sufficiently low particle number density, i.e., less than 10^5 per cubic centimeter, the interaction of particle-fluid and particle-particle can be ignored. The motion of particles in this flow is the result of a combination of gravity, particle inertia,

fluid viscosity and electrostatic image force. Most of the previous researches regarding this subject concentrated on fully-developed flows in a parallel channel in vertical or horizontal orientation. This study will begin with a parallel horizontal channel and extend it to divergent channels under different divergent angles. The turbulent fluid phase is from developing flow to developed flow in order to perform a realistic simulation. Sophisticated CFD software based on the finite-element method is employed for the construction of the flow model and the simulation of flow phenomenon.

It has been shown experimentally that airborne particles or aerosols carrying electrostatic charge significantly affect the motion of particles and result in higher particle deposition rates than that based on the calculation for gravity force alone. This fact attracts much attention lately and many researchers have investigated this subject by means of a laminar flow of gas with particulate suspensions. However, this study considers turbulent flow in a divergent channel with those identified effects of gravity force, particle inertia, fluid viscosity and electrostatic image force in a wide variety of situations in order to obtain useful knowledge of particulate behavior. The governing equations based on the principle of Newton second law under the coupled effects mentioned above with associated boundary conditions are solved numerically by the forth order Runge-Kutta method. The particles depositions are obtained by solving the trajectory of particles. The coupled result of those effects mentioned above and the influence of fluid phase are discussed in detail.

In chapter two, a literature survey of many previous investigations is introduced in order to obtain a general understanding on this subject. In chapter three, the principle and algorithm of constructing a turbulent flow as well as the characterization of aerosol

particles and the governing equations of particulate motion involving electrostatic force are presented.

In chapter four, the numerical analysis of particle trajectory and the calculation of particles deposition are carried out with the forth order *Runge-Kutta* method. In chapter five, the results of particle deposition under different conditions are discussed and various dimensionless parameters are analyzed accordingly. The conclusion of this work and suggestions for further investigation are presented in chapter six.

CHAPTER 2

LITURATURE SURVEY

As mentioned in the previous chapter, many researchers have conducted investigations on gas-solid two phase flows. Due to the complexities of the flow, a large number of publications in both analytical and experimental aspects of many facets have been released. Obviously, it is impossible to review all these publications in this chapter. A brief survey that covers studies of particle suspension in a channel flow and related investigations of turbulence modeling is presented here.

In the late 1950s, Friedlander and Johnstone [3] performed an experiment to study the deposition rate of dust particles on the wall of a tube with an analysis of the mechanism of particle suspension carried by a turbulent stream of air. Two major effects of the net rate of particles deposition were identified as the rate of particles transported toward the wall and the rate of re-entrainment. The second effect could be reduced by means of allowing only a single layer of accumulated particles on the surface and taking precautions of ensuring adherence of all particles which would strike on the surface without rebounding.

An investigation of adherence of solid particles on solid surfaces was carried out by Corn [4] in early 1960s. The results showed that adherence is due to either electrical forces including contact potential difference, dipole effect, space charge and electronic structure, or liquid forces including flow viscosity effects and surface tension.

Stukel and Soo [5] conducted an experiment about the hydrodynamics of suspended magnesia particles in an air flow inside a parallel-plate channel under different

mass flow ratios of solid particles to air from 0.01 to 0.1 lb. particles per pound of air. The nature of the developing turbulent boundary layer for dilute suspensions was discovered. It was observed that the density of particles is higher at the wall than at the core because of the presence of charge on particles induced by surface contact. Furthermore, as analogous to rarefied gas motions, the slip velocity of a particle brought about by the lack of particle to particle collisions in the suspension at the wall was observed. It was concluded that similarity laws for the scaling of equipment for air pollution control should include the momentum transfer number, the electroviscous number and the Reynolds number in which the electroviscous number is especially important where the particles possess large charge-to- mass ratios.

Soo and Rodgers [6] conducted an intensive investigation on the electro-aerodynamic precipitator in which a set of high voltage electrodes provided an electric field between the electrodes and collecting plates. The particles in the dust-laden gas flow were carried by both the gas flow and the electric field toward the ground plates. The experimental results showed that such a precipitator reached consistently high efficiency (above 99%), and had compactness and light weight. As in the analytical study, Soo and Rodgers defined a sticking coefficient, η, which is related to particles drifting toward the plate being collected. This sticking coefficient was defined that η=1 for complete sticking and subsequent removal and η=0 for zero adhesion of particles on this wall.

In the early 1970s, Soo and Tung [7][8] conducted an analysis of a fully developed pipe flow of suspension in a turbulent fluid within a gravitational and electric force fields with a condition of shear flow field included. The parameters which affected the state of motion were identified as pipe flow Reynolds number, Froude number, diffusion-response

number, electro-diffusion number, momentum-transfer number and particle Kundson number. Later they extended this research to include the effects of deposition and entrainment of particles. Additional considerations were found to be the diffusion and settling under field forces, the sticking probability of a particle at the wall and that to a bed of similar particles.

Pich [9] derived an equi-penetration curve of particles at the inlet plane by means of the particle trajectory function. The particles below the equi-penetration curve are considered deposited on the wall and the deposition efficiency is obtained by integration of the product of particle velocity and the area between the equi-penetration curve and the boundary of the channel wall.

Peddieson [10][11] performed a theoretical study about the prediction of the performance of dust collectors in which a multi-phase flow exists. Later he studied the motion of a dust carrier gas suspension in the vicinity of a sphere or a circular cylinder which has been of interest for several engineering applications such as the sampling probe in a dust collection device for the purpose of monitoring.

A Lagrangian approach based on the concepts of the particle trajectory function and the limiting trajectory was developed in the mid 1970s by Wang [12] for the calculation of the precipitation efficiency of channels of different cross-section. The particle trajectory function he used is equivalent to the stream function of a virtual flow field in which the motion of particles are considered. The two dimensional laminar flows in flat channels and circular tubes, and the motion of small particles and gravitational force are considered in this analysis. According to this investigation, the use of a particle trajectory function provides a simple way to calculate the flow rate of particles through any area.

Eldighidy et al. [13] did some theoretical analysis on particles deposition in the entrance of a channel and that in a diffuser using the Eulerian approach. These studies have taken the effect of diffusion, the electrostatic repulsive force and adhesive force into consideration. The result showed that the effect of electrostatic charge played an important role in particle deposition and the surface adhesion has a smaller effect on the rate of deposition than the electrostatic charge does. Moreover, the rate of deposition and pressure gradient of flow were found to be greatly affected by the divergent angle in a diffusive flow. Because the point of separation occurs earlier at larger divergent angles, the rate of deposition increases rapidly with the increasing divergent angle in the case of presence of electric charge, and the rate of deposition decreases rapidly with increasing divergent angle in the case of absence of electric charge.

Taulbee and Yu [14] conducted an investigation of simultaneous diffusion and sedimentation of aerosol particles from both plug (uniform) and Poisouille (fully developed) flows in two dimensional channels. It was found that the fractional penetration depends on a parameter $q''=hV_g/D$ where h is the channel half width, V_g is the settling velocity of a particle, and D is the Brownian diffusion coefficient. The result showed that for $q'' < 0.1$, the particle loss was due to diffusion alone and for $q'' > 200$, the particles deposition was due to the settling, and in the range $0.1 < q'' < 200$, the particle deposition due to the combined mechanism was significantly smaller than the algebraic sum of deposition due to two independent mechanisms.

In the late 1970s, Yu and Chandra [15] analyzed the effects of the space-charge repulsive force and the electrostatic image force on the deposition of suspension of electrostatically charged particles in a fluid and compared the results with existing

experimental data. It was found that at the particle number density of 10^5 particles per cubic centimeter, the space charge force has a small effect on the deposition mechanism and the predominate effect is the image force. In this model of image force effect, the interactive force between particles is negligible and the deposition of each particle is independent of particle number density.

Thiagarajan and Yu [16] studied the precipitation of aerosols from laminar flows in both parallel-plate and cylindrical channels due to the simultaneous effect of gravitational and electrostatic image forces. The equations of particulate motion were derived for the case in which the inertia effect of the particle was negligible. The results showed that the particle deposition due to gravitational force alone is considerably lower than that due to electrostatic image force alone.

Chen [17] did a theoretical study of aerosols deposition in a long channel due to the effects of diffusive and electrostatic charge. The diffusion equation and the Poisson equation for flow of aerosol particles with electrostatic charge field force were solved by means of integral method based upon flow of gas with a uniform or parabolic velocity profile. It was found that the inverse of the centerline particle number density increased linearly with the product of the electrostatic parameter and the axial distance for flow near the channel inlet. The centerline particle number density, the penetration and the electric field force decreased exponentially with the axial distance for flow far from the channel inlet.

In the early 1980s, Chen and Gelber [18] studied the laminar flow of particle in a parallel-plate channel under effects of electrostatic charge field force, diffusion and gravitational force. Variations in particles deposition were determined by use of a

dimensionless parameter, charge-diffusion parameter, which is a ratio of the space electrostatic charge effect to the diffusion effect. Their result showed that when this parameter is greater than 50, the diffusion effect is negligible. When gravity force acting in the direction of flow was considered, a velocity ratio which is the terminal velocity of the particle to the mean velocity of fluid flow is introduced. In this case, the space electrostatic charge field force and the gravity force were considered and the velocity profile of fluid flow was either uniform or fully developed.

Furthermore, Chen et al [19] extended their previous investigation to include the effect of particle inertia on the deposition of highly charged aerosol particles of size less than 20 micrometer from both uniform and fully-developed laminar flows in a parallel-plate channel with grounded channel walls. This numerical analysis assumed that the primary deposition was due to the space charge. The image force, gravity force, diffusive force and inertia force were compared with charge force and viscous force by defining several dimensionless parameters. It was found that the diffusive force was negligible for particles of size less than 20 micrometer and the gravity force was also negligible for highly charged fine particles. The inertia effect was significant for highly charged particles of 10-20 micrometer diameter and deposition decreased with increasing inertia effect but might be negligible for particles of size less than 5 micrometer.

Two important events affected the investigations about suspended particles of flows in 1980s. First is the need from the rapidly growing manufacturing industries such as semiconductor which needed to reduce the micro contamination due to the higher density of integral circuits on a single chip. Second is the advancement of computational modeling techniques of turbulence by means of finite difference and finite element methods such that

this important physical phenomena can be studied by using finite element approaches and algorithms to simulate the different conditions. A very wide variety of publications of this subject are available so that, in the following section, two important papers are summarized first and then some publications regarding this study are presented.

Cooper [1][20] summarized the detail understanding of fine particles contaminant by introducing the effect on product, transport, sources, measurement and deposition mechanism of airborne particles of micro and sub-micro size in the semiconductor industry and provided a review of the needed micro contaminant control research to improve the effectiveness of removal of particles and future clean room technology. The research involves the identification of sources, transport modeling, aerosol characterization, deposition mechanism analysis and the technique of surface particle removal.

Ferziger et al [21] classified the methods of dealing with turbulent flows in two aspects that are the method of treating the fluctuations and the manner of handling the geometry of the flow field. The methods of computation of turbulence are classified into five major categories that are correlations, integral methods, Reynolds-Averaged equations, large eddy simulation and full simulation, and the selection of the method is based upon the conditions and geometry of flow to be dealt with. A classification of turbulent flows is also presented in order to provide a better understanding about turbulence for the sake of choosing a proper computation method and modeling approach.

Fichman et al [22] proposed a model of particle deposition from a turbulent flow to a smooth surface based on the calculation of particle trajectories only. This model was mainly based on the calculation of particle trajectories in the wall region by using a detailed description of the flow in this region. The deposited particles were assumed to come from

the space between two eddies. The limiting trajectory in the developed flow field must be obtained first in order to calculate the deposition. This task was done by solving the Lagrangean equations of particle motion including the lift force perpendicular to the flow direction that resulted from the shear flow in the streamline direction. It was found that the lift force is important in the deposition process.

Yu [23] conducted an investigation on the deposition of airborne dust particles due to electric charge force. The electric charge carried by these particles are found to increase the amount of inhaled particles deposited in the lung. It was shown that for environmental aerosols with particle concentrations below 10^5 particles per cubic centimeter, the electrostatic image force acting on the particle due to particle-wall interaction is responsible for the observed deposition enhancement. Comparisons of this result with available deposition data showed a very good agreement.

McLaughlin [24] studied the deposition of aerosol particles in a numerically simulated channel flow. A pseudo computer program is used to simulate the three-dimensional, time-dependent turbulent channel flow field and the trajectories of rigid spherical particles in that flow. The flow of a dilute particle concentration in a vertical channel without gravity effect was considered. It was found that when the particles were assigned at random initial locations with initial velocities equal to the local fluid velocity, the particles tend to accumulate in the viscous sublayer. At the edge of the viscous sublayer, the particles which deposit on the wall surface possess normal components of velocity that are comparable in magnitude to the intensity of the normal component of the velocity in the core of channel flow, i.e., of the order of magnitude of the friction velocity. A shear-induced lift force with the form derived by Saffman for laminar flow is found to be virtually

ineffective on particle trajectories, except within the viscous sublayer in which the Saffman lift force plays a significant role both in the inertial deposition of particles and in the accumulation of trapped particles.

Ramarao and Tien [25] performed an analytical study of aerosol deposition in a two-dimensional laminar stagnation flow under the combined effect of inertial impact, interception and gravity force. Analytical expressions of particle trajectories were obtained by ignoring the boundary layer effect near the deposition plane. If the effect of boundary layer was included, particle trajectory can only be solved numerically. The results showed that aerosol flux is uniform along the deposition plane which is true regardless of whether the effect of boundary layer is included or not, and that the inclusion of boundary layer in determination of deposition tends to increase the deposition flux and this effect decreases with increasing particle size. It was also found that, under certain limiting conditions, this analysis yielded identical results compared with those from previous investigations.

Chen et al [26] derived the equation of image force for a two-dimensional convergent channel by using the concept of an image circle. The analysis of particle deposition from uniform flows due to the electrostatic image force alone for convergent channels with convergent angles of 15°, 10°, 5° was studied. It was concluded that, in comparison with the parallel-plate channel, the depositions were found to be smaller than that near the entrance of convergent channels, but they increased as the axial distance was increased.

Arastoopour et al [27] developed a model of two-dimensional, steady state, two-phase hydrodynamic flow based upon multiphase flow equations of continuum mechanics that describe the behavior of dilute gas-solid flow in a vertical pipe. This model considered

particles as the same size and their boundary layers as a separate continuum phase. Furthermore, viscous dissipation forces and phase interaction forces were incorporated. It was found that gas-solid drag forces play an important role in describing the behavior of two-phase flow and it is pointed out that more fundamental research is necessary to obtain a suitable expression which is capable of describing the interactive forces between the gas phase and particulate phase at different regimes.

Abuzeid, Busuaina and Ahmadi [28] studied the motion of small suspended particles in a turbulent channel flow by using a Lagrangian simulation technique. The effects of Reynolds number, turbulence intensity and particle diameter were investigated. The result showed that turbulence fluctuations and Brownian motion have significant effects on the particle deposition mechanism; the turbulence fluctuations remain significant regardless of particle diameter while the Brownian effect becomes negligible as the particle diameter becomes greater than 1 μm; the turbulence intensity is shown to be directly proportional to the deposition rate. This analysis also concluded that, as Reynolds number increases, the rate of particle deposition increases as well.

Li and Ahmadi [29] extended the previous investigation to include effects of Brownian diffusion, Saffman lift force, gravity and particle-surface interactions in their computational model. Several simulations of deposition of various particle sizes were performed and the corresponding deposition velocities were evaluated and the effect of particles rebounding from the surface on the rate of particles deposition was also studied. It was shown that, for particles with diameter larger than 2 μm, gravitational force increases the deposition velocity significantly. In the vertical channel, the minimum deposition rate occurs for particles with diameters in the range of 1.0 - 5.0 μm and in the horizontal

channel, the minimum deposition rate shifts to the particle diameter range of 0.1 - 0.5 μm due to the effect of gravitational force. The effect of particle rebound becomes noticeable when the diameter of particle is larger than 10 μm.

Chen, Chiou and Sun [30] conducted a numerical investigation on the deposition of particles in a convergent channel with a wide range of parameters. In this analysis a laminar fluid flow of uniform and developing velocity profiles was used and the effects of particle inertia, gravity force, fluid viscous force, and electrostatic image force were included in the computational model. The governing equations were built upon a trajectory method to find the trajectory of each particle entering the channel and the deposition was based on the distance traveled by a particle to reach the wall. Depositions for different combinations of parameters were presented.

Goldberg [31] proposed a modified version of the Baldwin-Barth κ-$\Re$ two-equation turbulence model in which the near-wall function f_μ is based on the ratio of the large eddy and the Kolmogorov time scales. This modification is from κ–ε two equation model by taking $\Re \equiv \kappa^2 / \varepsilon$ and results in a robust, pointwise turbulence model applicable to both wall-bounded and free shear flows that, nevertheless, does not require explicit knowledge of local distance to walls, rendering it useful within both structured and unstructured computational frameworks for flow predictions involving complex geometry configurations. Several demonstrated flow cases were carried out by computer program PHOENICS 1.4 and the results were compared with the existing experimental data.

Squires and Eaton [32] investigated the effect of selective modification of turbulence by particles on κ-ε models for two-phase flows by using the data from direct numerical simulation of particle-laden isotropic turbulence. Simulation results were

obtained by using as many as 64^3 grid points and up to 10^6 particles, the ratio of particle time constant to large-eddy turbulence time scale from 0.14 to 1.50, and the parameter of particle mass loading as 0.0, 0.01, 0.1 and 1.0. The results showed that no significant change was made from this modified model to single-phase model for parameter of particle mass loading below approximately 0.2, and preferential concentration of lighter particles by turbulence generated vorticity fluctuations at higher particle mass loadings.

Bertodano et al [33] proposed an extension of the κ-ε model for bubbly two-phase flow. The basic assumption for this analysis is that the shear-induced turbulence and bubble-induced turbulence may be linearly superposed, and result in a model with two time constants which matches both homogeneous two-phase turbulence data and pipe data. The coefficient of the single-phase κ-ε model remained the same and only one additional coefficient is added: the virtual volume coefficient of the bubbles. The result was obtained by the computer program *PHOENICS* by using the adjusted under-relaxation false time-step parameter and against the existing experimental data.

Sun and Chen [34] performed a numerical analysis about the particle deposition from two-dimensional laminar flows in both convergent and divergent channels due to the coupled effect of particle inertia, gravitational force, fluid viscous force and electrostatic image force under different conditions. The computational model was built upon the governing equations of particles by using the Lagrangian trajectory method in order to obtain the particle traveling distance from the channel entrance to the channel wall or outlet. Considerations of flow separation in a divergent channel and the nature of the image force in a convergent channel or a divergent channel were also included. It was found that the closer the initial particle position to the channel wall may not mean faster deposition;

the longest deposition distance occurs in the range of Q/G=0.1 to 1 in either a convergent channel or a divergent channel; for Q/G<0.001, the deposition distance curves are almost the same; when Q/G>10, the gravitational force may be neglected. It was concluded that effects of gravitational force and electrostatic image force significantly influence the particle deposition.

Graham [35] performed a numerical simulation of turbulent particle dispersion by using an improved eddy interaction model of Hutchinson et al (1971). Three effects, which are crossing trajectory effect due to drift, particle inertia effect, and continuity effect, were observed under the considerations of an idealized situation of homogeneous, isotropic and stationary turbulence with a high particle/fluid density ratio, and the influence of gravity. It was found that by ensuring the consistency of various integral turbulence scales between the analytical theory and the eddy interaction model, the performance of this improved numerical method is guaranteed, and the inclusion of the gravity effect in this model has a clearly beneficial influence on the prediction of the dispersion coefficient between numerical and analytical results over a wide range of conditions.

In summary, earlier researchers used the Eulerian approach to obtain the solutions of laminar solid-gas two phase flow problems and used uniform flow profiles to simulate the turbulent flow field in a two-dimensional channel and a tube, like Soo and Yu. Most interest was given to the behavior of particles under effects of different forces. Later investigators used the Lagrangian approach to analyze the particle motion in both laminar and turbulent solid-gas two phase flow. Some researchers, like Li and Ahmadi, concentrated on the interaction between particle and particle, particles and channel wall, and particles and fluid flow. The investigations on particles deposition from a laminar

channel flow had been carried out by Yu, Chen, Lai, Chiou and Sun using particle trajectory methods with uniform, fully-developed and developing flow fields under a variety of effects such as gravity force and electrostatic force. However, particle deposition from a turbulent solid-gas two phase flow in a channel has not been studied yet.

Further analysis in this work is to study theoretically the aerosol particles deposition from two-dimensional, developing turbulent flows in a parallel-plate channel and a divergent channel due to the coupled effect of particle inertia, gravity, fluid viscosity and electrostatic image force under the consideration of dilute suspension with particle number density less than 10^5 per cubic centimeter.

CHAPTER 3

ANALYSIS

The main interest of this chapter is to evaluate the assumptions based on the considerations of the problem of gas-solid two-phase turbulent channel flow, to discuss the technique of turbulence modeling, and to present the derivation of the governing equations of particle dynamics.

In many areas of fluid mechanics in engineering application and industrial processes, the flow phenomenon is almost always turbulent. Another interesting fluid mechanism which is usually found in the same areas is gas-solid two-phase flow. Therefore, it is a matter of necessity to study these important fluid mechanisms. The focus of this work is that, by analyzing deposition of aerosol particles from a turbulent gas-solid two-phase flow in a two-dimensional divergent channel, better understanding of these complicated fluid mechanisms can be achieved.

3.1 Basic Assumptions and Flow Analysis

This analysis is carried out under the following assumptions and considerations.

(1) Steady incompressible flow.

(2) Uniform inlet velocity profile.

(3) Turbulent flow region.

(4) Thermally insulated channel walls without heat transfer.

(5) Electrically grounded channel walls.

(6) Dilute aerosol suspension with particles number density less than 10^5 / cm^3.

(7) Negligible deposited particle layer thickness.

(8) No interaction between particles.

(9) Mass density ratio of particle to gas, ρ_p / ρ_g, of the order of 10^3.

(10) Single size sphere particles.

(11) Under the effects of particle momentum, gravity, viscosity and electrostatic image forces.

In this work the fluid is air at atmosphere pressure and normal room temperature of 20 ^{0}C, with a steady freestream flow velocity of about 11 m/s. The Mach number is about 0.03 in this case. It is reasonable to consider this flow as incompressible and isotropic. Furthermore, the flow Reynolds number may range from thousands to hundreds of thousands that depends on the flow characteristic length. Therefore, it is considered as steady turbulence under these conditions.

In this analysis there is no heat transfer between the channel walls and the flow. This condition also applies on the gas-solid two-phase flow such that deposition of particles on the channel walls has no effect on the temperature of the flow field and channel walls.

As introduced in chapter 2, many researchers such as Yu and Chandra [15] have shown that the electrostatic image force plays an important role in the mechanism of particle deposition from a gas flow with dilute solid suspension. Dilute gas-solid two-phase flow are widely used in many chemical, gas, food processing and waste treatment industries [27]. Therefore, in this analysis, the channel walls are considered as electrically grounded and the particle phase is considered as a dilute suspension with a number density

of 10^5 per cm^3. Under these considerations the equations of electrostatic image forces acting on a single particle can be applied and adopted into the mathematical model.

As discussed in chapter one, the range of size of aerosol particle is from 0.01 μm to 200 μm. Considering the environment of this analysis, as mentioned previously, the sources of airborne particles are limited. Therefore, the particle size can be considered in the range from 0.1 μm to 10 μm in this analysis..

The Brownian diffusion force is an major effect in the concentration distribution of a cloud of sub-micro particles and it is treated as white noise with random frequency of appearance [29]. Since the particle size is set to be within a certain range and the particle phase is a dilute suspension in this analysis, it is considered to eliminated this effect.

Although it has been shown in table 1-2 that the mass ratio of aerosol particle to atmosphere is very big, considering the sources of airborne aerosol particles as introduced in chapter two, the mass ratio of particle to atmosphere is taken as 10^3 in this analysis. Therefore, the forces of fluid pressure gradient and apparent mass are considerably smaller. They are considered negligible under these conditions.

Furthermore, with aerosol particles of limited size, mass and quantity, the cumulative clusters of deposited particles on the surface of the channel walls is out of consideration in this analysis. The surface and mass of the channel walls are considered constant regardless of deposited particles. Similarly, the interactions between particles are negligible due to the consideration of dilute suspension. It is assumed that the particulate phase can be represented by a single mean size of spherical shape so that all particles are considered to have the same diameter.

One major force acting on a particle is the drag force due to the fluid viscosity. Since the flow is incompressible, the drag force and drag coefficient are obtained by Stokes law as shown below.

Stokes drag: $$F_D = 3\pi\mu d_p\left(u - u_p\right) \tag{3.1.1}$$

Drag coefficient: $$C_D = 24 / \mathrm{Re}_p \qquad \text{for } \mathrm{Re}_p < 1 \tag{3.1.2}$$

Definition: $$C_D = \frac{F_D}{\left(\pi d_p^{\,2} / 4\right)\left(\rho u^2 / 2\right)} \tag{3.1.3}$$

where Re_p is the relative Reynolds number of a particle with respect to the fluid flow, ρ is the density of fluid, u is the velocity of the fluid, and d_p is the diameter of a particle.

According to the experimental result by Soo and Zhu [36], the relative speed of a particle with respect to the carrier fluid is about 10% ~ 15% of the flow speed. For example, taking $d_p = 1\ \mu m$, $u = 11$ m/s, u_p' as the relative speed of a particle, and atmosphere at 20^0C as the carrier fluid. Then:

$$u_p' = 1.65 \text{ m/s}$$

$$\mathrm{Re}_p = 0.11 < 1$$

Therefore, in this analysis the drag coefficient is taken as equation (3.1.2).

As for the gravity and buoyancy forces on particles, it is obvious that, regardless of particle size, the gravity force acting on the aerosol particle is much greater than the buoyancy when $\rho_g / \rho_p < 0.001$. Therefore the buoyancy force is neglected and the gravity force is considered as having an effect on the aerosol particle in this analysis.

Since the flow is developing in the two-dimensional channel, the effect of the boundary-layer must be considered. Due to the flow viscosity, the instantaneous flow field

is a function of the entire history of the particulate motion that is the Basset force. Klinzing [37] gave three examples to indicate the magnitude of Basset force and it was concluded that, for mass ratio of particle to gas equal to 10^3, the Basset force is less than 10% of the Stokes drag force. Other researchers such as Ahmadi [28] had shown that Basset force is negligible for aerosol particles. Therefore it is reasonable to exclude the Basset force in this analysis.

Another important subject regarding boundary-layer is the Saffman lift force on particles in a gas-solid two-phase flow. The Saffman lift force is induced by a velocity gradient in a shear flow and the comparison of this force, F_L, to Stokes drag force, F_D, is given as follows.

$$\frac{|F_L|}{|F_D|} \propto \left[\frac{d_p{}^2 (du/dy)}{\nu} \right]^{1/2} \tag{3.1.4}$$

McLaughlin [24] had shown that the Saffman lift force affects larger particles but has negligible effects on small particles with comparison to the normal component of the Stokes drag force. So, the exclusion of the Saffman lift force in this analysis is reasonable.

As a summary of the above explanations on the assumptions made at the beginning of this chapter, the gravity, viscosity, particle inertia, and electrostatic image forces are taken into consideration. The governing equations of particle dynamics based on the coupled effects by these forces are described in the following sections.

3.2 Analysis of Two-dimensional Turbulent Channel Flow

For almost a century, many researchers have accomplished enormous investigations and many mathematical models have been established in order to simulate turbulent flows. However, due to the nature of turbulent flows that depends, not only the fluid properties, such as density, viscosity, velocity and so on, but also the flow geometry configuration, such as channel flow, open surface flow, flow past an object, and so on, there is no mathematical model which can handle all kind of flow problems. Therefore, it is essential that, in order to perform a reliable simulation of a flow problem, a proper mathematical model must be chosen according to the problem to be solved.

The flow problem in this work is an isotropic turbulent air flow in a two-dimensional divergent channel with constant incoming flow at the inlet. This problem involves two important subjects which are, flow separation due to a divergent channel, and flow relaminarization due to gradually widened channel width. These two effects greatly influence the velocity distribution of channel flow because they tend to change the flow pattern in opposite directions.

The following analysis is continued from the continuity equation (1.3), momentum equation (1.6) and energy equation (1.8). Since the turbulent flow in a two-dimensional channel is the concern, the boundary layer must be dealt with. Figure 3.1 represents the flow problem in this work and the following assumptions are made under the consideration of two-dimensional channel.

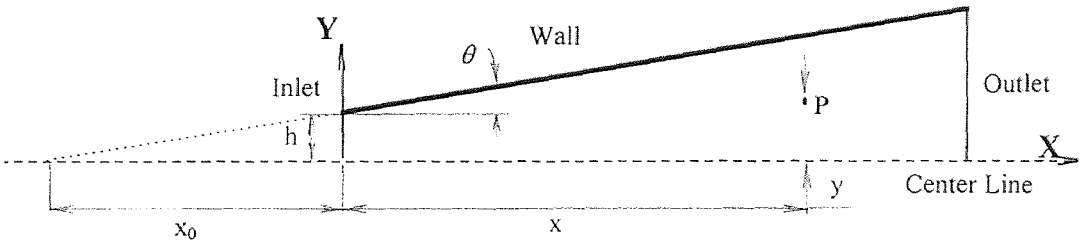

Fig. 3.1 Divergent channel for turbulent flow simulation

(1) Boundary layer thickness $\delta(x) << x$

(2) $\bar{v} << \bar{u}$

(3) $\dfrac{\partial}{\partial x} << \dfrac{\partial}{\partial y}$

(4) $\bar{w} = 0$ and $\dfrac{\partial}{\partial z} = 0$

Then the boundary-layer approximations for incompressible flow can be obtained as shown below.

continuity: $$\frac{\partial \bar{u}}{\partial x} + \frac{\partial \bar{v}}{\partial y} = 0 \qquad (3.2.1)$$

x momentum: $$\bar{u}\frac{\partial \bar{u}}{\partial x} + \bar{v}\frac{\partial \bar{u}}{\partial y} \approx U_O \frac{dU_O}{dx} + \frac{1}{\rho}\frac{\partial \tau}{\partial y} \qquad (3.2.2)$$

y momentum: $$\frac{\partial p}{\partial y} \approx -\rho \frac{\partial \overline{v'^2}}{\partial y} \qquad (3.2.3)$$

thermal energy: $$\rho c_p \left(\bar{u}\frac{\partial \bar{T}}{\partial x} + \bar{v}\frac{\partial \bar{T}}{\partial y} \right) \approx \frac{\partial q}{\partial y} + \tau \frac{\partial \bar{u}}{\partial y} \qquad (3.2.4)$$

turbulent heat flux: $$q = k\frac{\partial \bar{T}}{\partial y} - \rho c_p \overline{v'T'} \qquad (3.2.5)$$

turbulent shear stress: $$\tau = \mu \frac{\partial \bar{u}}{\partial y} - \rho \overline{u'v'} \qquad (3.2.6)$$

where U_o is the freestream velocity at the inlet of the channel.

One obvious attempt to add "turbulence conservation" relations to the time averaged equations [3.1] is a relation for the turbulence kinetic energy K of the fluctuations which is defined as described below.

$$K = \frac{1}{2}\left(\overline{u'u'} + \overline{v'v'} + \overline{w'w'}\right) = \frac{1}{2}\overline{u_i' u_i'} \qquad (3.2.7)$$

$$\frac{DK}{Dt} = -\frac{\partial}{\partial x_i}\left[\overline{u_i'\left(\frac{1}{2}u_j'u_j' + \frac{p'}{\rho}\right)}\right] - \overline{u_i'u_j'}\frac{\partial \bar{u}_j}{\partial x_i}$$

rate of change of turbulent energy — convective diffusion — production

$$+\frac{\partial}{\partial x_i}\left[\overline{\nu u_j'\left(\frac{\partial u_i'}{\partial x_j} + \frac{\partial u_j'}{\partial x_i}\right)}\right] - \overline{\nu \frac{\partial u_j'}{\partial x_i}\left(\frac{\partial u_i'}{\partial x_j} + \frac{\partial u_j'}{\partial x_i}\right)} \qquad (3.2.8)$$

work done by turbulent viscous dissipation — turbulent viscous dissipation

After certain operations on those equations above, the turbulence energy equation in the two-dimensional boundary-layer form as shown below.

$$\bar{u}\frac{\partial K}{\partial x} + \bar{v}\frac{\partial K}{\partial y} \approx -\frac{\partial}{\partial y}\left[\overline{v'\left(\frac{1}{2}u_i'u_i' + \frac{p'}{\rho}\right)}\right] + \frac{\tau}{\rho}\frac{\partial \bar{u}}{\partial y} - \varepsilon \qquad (3.2.9)$$

where $\varepsilon = -\nu\overline{\frac{\partial u_i'}{\partial x_j}\frac{\partial u_j'}{\partial x_i}}$ = turbulent dissipation

However, this equation involves two additional turbulence parameters. The pressure-strain term which is the first term at right-hand side of equation (3.2.9) and the turbulence dissipation. In 1972, a seminal paper by Jones and Launder [38] lead to an open door of turbulence modeling. They modeled both turbulence energy and dissipation equations such that two resulting models are given for fully elliptic (nonboundary-layer) high-Reynolds-number flow as shown below.

energy:
$$\frac{DK}{Dt} \approx \frac{\partial}{\partial x_j}\left(\frac{\nu_t}{\sigma_K}\frac{\partial K}{\partial x_j}\right) + \nu_t \frac{\partial \overline{u_i}}{\partial x_j}\left(\frac{\partial \overline{u_i}}{\partial x_j} + \frac{\partial \overline{u_j}}{\partial x_i}\right) - \varepsilon \qquad (3.2.10)$$

dissipation:
$$\frac{D\varepsilon}{Dt} \approx \frac{\partial}{\partial x_j}\left(\frac{\nu_t}{\sigma_\varepsilon}\frac{\partial \varepsilon}{\partial x_j}\right) + C_1 \nu_t \frac{\varepsilon}{K}\frac{\partial \overline{u_i}}{\partial x_j}\left(\frac{\partial \overline{u_i}}{\partial x_j} + \frac{\partial \overline{u_j}}{\partial x_i}\right) - C_2 \frac{\varepsilon^2}{K} \qquad (3.2.11)$$

where ν_t is the eddy viscosity, σ_K and σ_ε are effective "Prandtl numbers" relating eddy diffusion of K and ε to the momentum eddy viscosity in the following manner.

$$\sigma_K = \nu_t / \nu_K \qquad \sigma_\varepsilon = \nu_t / \nu_\varepsilon \qquad \nu_t = \frac{C_\mu K^2}{\varepsilon}$$

The five empirical constants in these modeling equations have the following recommendations for attached boundary-layer calculations.

$$C_\mu = 0.09 \quad C_1 = 1.44 \quad C_2 = 1.92 \quad \sigma_K = 1.0 \quad \sigma_\varepsilon = 1.3 \qquad (3.1.12)$$

These values are not universal but have to be modified according to the flow problem to be solved.

In 1981, many investigations on incompressible and compressible flows had been assembled for the Standford Conference [39]. It was concluded that K–ε turbulence model

produced reliable results in some particular cases but the dissipation relation must be used with great caution for flow problems with irregular geometry. An interesting case presented in the 1981 Standford Conference is that a flow undergoes reverse transition or relaminarization [40][41]. A flow in a divergent channel, as shown in figure 3.1.1, is the typical example. In this case, turbulent shear decreases faster than the rms fluctuations, but both decay slowly over tens or hundreds of diameters. Dissipation exceeds turbulent production during the expansion and is considered as the stabilizing effect of acceleration on the flow field. It was found that, with certain successful results, the widely used K-ε model of Jones and Launder was proposed to predict this type of flow.

For this reason the simulation of turbulent flow in a two-dimensional divergent channel in this work is carried out by *FIDAP* computer software using the K-ε model which is considered the suitable and well-adopted mathematical model for this flow problem.

3.3 Analysis of Particle Dynamics

According to figure 3.1, the motion of a single particle, P, with sphere shape of diameter d_p and mass m_p under the coupled forces in a two-dimensional turbulent channel flow can be described by Newton's second law. As discussed in the first section of this chapter, the coupled forces include the gravity, viscous, electrostatic image forces on a particle, and the inertia momentum of the particle itself. The governing equations of particle motion are shown below.

x direction:
$$m_p \frac{d u_p}{dt} = 6\pi\mu d_p\left(u - u_p\right) + f_x \qquad (3.3.1)$$

y direction: $$m_p \frac{d v_p}{dt} = 6\pi\mu d_p\left(u - u_p\right) - m_p g + f_y \qquad (3.3.2)$$

Where u_p and v_p are particle velocities in the x and y direction respectively, g is the gravity acceleration, and f_x and f_y are electrostatic image forces on a particle in the x and y directions respectively. Because a dilute solid suspension is assumed, the velocity distributions of the gas phase, u and v, are obtained from numerical simulation of the fluid phase above and then adopted in the resulting flow field into these governing equations.

Since channel walls are considered electrically grounded, a particle with charge q in a two-dimensional channel induces successive images on both walls. The solution to this image-force condition is carried out by constructing the mirror images of a single charge q according to the zero potential walls. As shown in figure 3.1, the equations of image forces on a single particle P with charge q are given by the following expressions.

x direction: $$f_x = \frac{q^2}{4\pi\varepsilon_0}\left[\sum_{n=1}^{N}(-1)^n \frac{\sin\beta_n}{q_n^{\,2}} + \sum_{n=1}^{N-1}(-1)^n \frac{\sin\beta_{n'}}{q_{n'}^{\,2}}\right] \qquad (3.3.6)$$

y direction: $$f_y = \frac{-q^2}{4\pi\varepsilon_0}\left[\sum_{n=1}^{N}(-1)^n \frac{\cos\beta_n}{q_n^{\,2}} - \sum_{n=1}^{N-1}(-1)^n \frac{\cos\beta_{n'}}{q_{n'}^{\,2}}\right] \qquad (3.3.7)$$

where $N = \pi/(2\theta)$

β_n = angle between the x-axis and the chord connecting the charge q to the primary image n

$\beta_{n'}$ = angle between the x-axis and the chord connecting the charge q to the

secondary image n'

q_n = distance between the charge q to the primary image n

$q_{n'}$ = distance between the charge q to the secondary image n'

Detailed formulation of the image method is shown in the reference [26]

Due to the fact that the axial image force , f_x, should be zero when particle P is at the inlet plane of a divergent channel, and will gradually increase to its theoretical strength when particle P travels certain distance in the channel, the consideration of a correction factor K_m is necessary. Some researchers have derived the formula of this correction factor [34] that is also been employed in this analysis. Detailed description of this subject is shown in appendix A. Therefore the electrostatic image force on a particle in the x direction becomes as shown form below.

correction factor: $$f_x' = K_m f_x \tag{3.3.8}$$

where $K_m = \left(x_i / x_o\right)^{1/3}$.

CHAPTER 4

METHOD OF SOLUTION

In this chapter we will discuss the steps and methods that are needed in obtaining the solution to the deposition of particles in two-dimensional channels. We may divide the process of analysis into three steps. The first step is the numerical simulation of turbulent flow in a two-dimensional channel using computer software *FIDAP*. The second step is the solution of the particle trajectory with the velocity field obtained in first step applied to equations of motion for the particles. The third step is the calculation of particle deposition from the particle trajectories.

4.1 Turbulence Modeling

As mentioned in chapter three, the K-ε model is used to simulate the turbulent flow in a two-dimensional channel. There are two primary parameters to be determined which are turbulence kinetic energy K and turbulence dissipation ε. The evaluation of these two parameters mainly depend on the flow type and the flow geometry. The fluid dynamic problem in this work is classified as a shear-free flow and the following equation is used to calculate the turbulence kinetic energy K.

$$\text{turbulence kinetic energy:} \qquad K = \alpha u_o^2 \quad (\alpha = 0 \sim 0.001) \qquad (4.1)$$

where α is a constant to be determined and u_o is the flow freestream velocity.

The second parameter, turbulence dissipation ε, can be obtained after the turbulence kinetic energy is obtained. The following formula in conjunction with equation (4.1) is used.

turbulence dissipation: $$\varepsilon = \frac{K^{3/2}}{\delta_l} \approx \frac{K^{3/2}}{0.1\delta} \tag{4.2}$$

where δ is the characteristic length. In this analysis the characteristic length of flow problem is selected to be the half width of the two-dimensional channel at the inlet plane.

Another important subject in turbulence modeling is the relaxation factor. Although there are some recommended values for this parameter, it is not universal for every flow problem. This parameter strongly influences the convergence of computation and the final solution. Therefore we will test the new model on flow problems with already known results so that the parameter of relaxation can be fine tuned until reliable results are produced.

Besides those parameters discussed above, several subjects must be dealt with in the numerical turbulence modeling. The first one is the solution algorithm which is used to calculate the solution in the iteration process. Although the *segregated* method has been suggested, after several tests it was found that the *successive substitution* method would give a better result. Therefore in this work the *successive substitution* method is used for all cases of turbulence simulations.

The second one is the choice of *upwind* parameters which significantly affect the convergence of the solution during the iteration process. This one also need to be tested and

fine tuned to an optimized set of parameters. Detail of these methods are presented in appendix B.

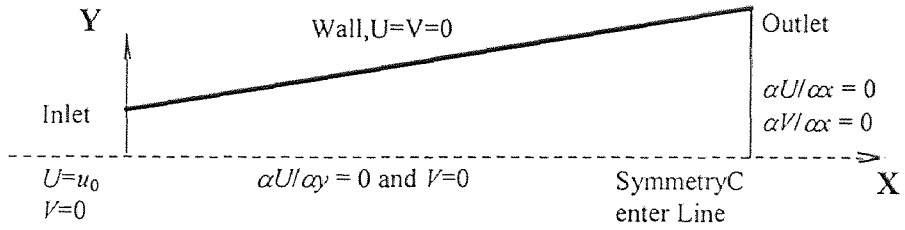

Figure 4.1 Boundary conditions of turbulent channel flow simulation

The boundary conditions of this turbulence simulation are shown in figure 4.1. Several flow problems with known results have been tested and all parameters discussed above have been modified to produce a reliable solution. Once this is completed, these parameters are used in the numerical simulation of the turbulent flow problem in this analysis. One example of numerical simulation compared to experimental results is presented in the next chapter by using these optimized parameters. Those programs used for the turbulence simulation in this work are presented in appendix C.

4.2 Solution of Particle Trajectories

When a particle initially at $t = t_0$, located at $x = x_0$ and $y = y_0$ is moving in a flow field, its trajectory can be obtained by the following integration over a time period.

x direction:
$$x = \int_{t_0}^{t} u_p dt' + x_0 \tag{4.3}$$

y direction: $$y = \int_{t_0}^{t} v_p dt' + y_0 \qquad (4.4)$$

in which u_p and v_p are determined from momentum equations (3.3.1) and (3.3.2) respectively.

x direction: $$m_p \frac{d u_p}{dt} = 6\pi\mu d_p\left(u - u_p\right) + f_x \qquad (3.3.1)$$

y direction: $$m_p \frac{d v_p}{dt} = 6\pi\mu d_p\left(u - u_p\right) - m_p g + f_y \qquad (3.3.2)$$

The following dimensionless parameters are substituted into equations (3.3.1), (3.3.2), (4.3) and (4.4). After these substitutions the governing equations become dimensionless forms.

$$T = \frac{t u_0}{h}$$
$$X = \frac{x}{h} \quad \text{and} \quad Y = \frac{y}{h} \qquad (4.5)$$
$$U = \frac{u}{u_0} \quad \text{and} \quad V = \frac{v}{v_0}$$

In these equations particle velocity components u_p and v_p are expressed as

$$u_p = \frac{dx}{dt} \quad \text{and} \quad v_p = \frac{dy}{dt} \qquad (4.6)$$

Equations (3.3.1) and (3.3.2) are non-dimensionalized in the following steps.

x direction:
$$m_p \frac{u_0^2}{h} \frac{d^2 X}{d T^2} = 6\pi\mu d_p u_0 \left(U - \frac{dX}{dT} \right) + f_x \tag{4.7}$$

y direction:
$$m_p \frac{u_0^2}{h} \frac{d^2 Y}{d T^2} = 6\pi\mu d_p u_0 \left(V - \frac{dY}{dT} \right) - m_p g + f_y \tag{4.8}$$

Because term $6\pi\mu d_p u_0$ is a constant, these two equations can be divided by this term as shown below.

x direction:
$$\frac{m_p u_0}{6\pi\mu d_p h} \frac{d^2 X}{d T^2} = U - \frac{dX}{dT} + \frac{f_x}{6\pi\mu d_p u_0} \tag{4.9}$$

y direction:
$$\frac{m_p u_0}{6\pi\mu d_p h} \frac{d^2 Y}{d T^2} = V - \frac{dY}{dT} - \frac{m_p g}{6\pi\mu d_p u_0} + \frac{f_y}{6\pi\mu d_p u_0} \tag{4.10}$$

The following dimensionless parameters are also defined to simplify the governing momentum equations (4.9) and (4.10).

$$S = \frac{\text{inertia force}}{\text{viscous force}} = \frac{m_p u_0}{6\pi\mu d_p h} \tag{4.11}$$

$$G = \frac{\text{gravity force}}{\text{viscous force}} = \frac{m_p g}{6\pi\mu d_p u_0} \tag{4.12}$$

$$Q = \frac{\text{charge force}}{\text{viscous force}} = \frac{q^2}{(4\pi\varepsilon_0)(6\pi\mu d_p u_0) h^2} \tag{4.13}$$

The governing equations become the following dimensionless forms.

x direction: $$S\frac{d^2X}{dT^2} = U - \frac{dX}{dT} + Q F_x' \tag{4.14}$$

y direction: $$S\frac{d^2Y}{dT^2} = V - \frac{dY}{dT} - G + Q F_y \tag{4.15}$$

where F_x and F_y are shown below.

$$F_x = -h^2\left[\sum_{n=1}^{N}(-1)^n \frac{\sin\beta_n}{q_n^2} + \sum_{n=1}^{N-1}(-1)^n \frac{\sin\beta_{n'}}{q_{n'}^2}\right] \tag{4.16}$$

$$F_y = -h^2\left[\sum_{n=1}^{N}(-1)^n \frac{\cos\beta_n}{q_n^2} - \sum_{n=1}^{N-1}(-1)^n \frac{\cos\beta_{n'}}{q_{n'}^2}\right] \tag{4.17}$$

In this analysis the axial component of the image force is in this modified form:

$$F_x' = K_m F_x \quad \text{and} \quad K_m = \left(x/x_o\right)^{1/3} \tag{4.16'}$$

4.3 Initial Conditions and Boundary Conditions

According to the assumptions discussed in chapter 3 and figure 3.1, the initial conditions and boundary conditions of a particle trajectory are as follows:

4.3.1 Initial Conditions

In this study 115 particles entering the inlet plane are traced. The initial positions of these 115 incoming particles are located at the inlet plane from $Y_0 = 0.998h$ to $Y_0 = -0.998h$. The

upper plane wall is located at $y = h$ and the lower plane wall is located at $y = -h$ at the inlet plane. Therefore the initial conditions of a particle trajectory can be described as below.

$$
\begin{aligned}
&t = 0 \\
&x = 0 \quad \text{and} \quad y = y_0, \qquad \text{for } -h < y_0 < h \\
&u_p = \frac{dx}{dt} = u_0 \text{ and } v_p = \frac{dy}{dt} = 0 \\
&w_h = h
\end{aligned}
\tag{4.18}
$$

where w_h is the half width of divergent channel at x.

After substituting equation (4.5) into equation (4.18), the initial conditions become

$$
\begin{aligned}
&T = 0 \\
&X = 0 \text{ and } Y = Y_0, \quad \text{for } -1 < Y < 1 \\
&U_p = \frac{dX}{dt} = 1 \text{ and } V_p = \frac{dY}{dt} = 0 \\
&W_h = 1
\end{aligned}
\tag{4.19}
$$

4.3.2 Boundary Conditions

(1) There is no slip between particle and channel walls. When $Y = 1$ or $Y = -1$, it is considered that the particle is deposited on the channel walls and will stick to the wall.

(2) In this analysis the length of the channel ranges from $40h$ to $50h$. When a particle travels to the channel outlet plane without reaching channel walls, i.e. $-1 < Y < 1$, it is considered to leave the channel without deposition, i.e. penetrate the channel.

Besides these initial conditions and boundary conditions discussed above, the solutions of equations (4.14) and (4.15) require prescribed dimensionless parameters S, G and Q and the half-divergent angle θ . The range of these parameters used in this analysis are

$$S = 0.01, 0.1, 1, 10, 100$$

$$G = 0.01, 0.1, 1, 10, 100$$

$$Q = 0.00001, 0.0001, 0.001, 0.01, 0.1, 1, 10, 100, 1000, 10000$$

$$\theta = 0^0, 7.5^0, 10^0, 12.5^0$$

A forth order Runge-Kutta method is used to carry out the solution for particle trajectory. Once all 115 particle trajectories are obtained, the fraction of particle deposition can be determined as discussed in the next section.

4.4 Fraction of Particle Deposition

Based on the conservation of mass of solid phase, the fraction of particle deposition is defined as the ratio of the total number of particles deposited on the channel walls at a given distance to the total number of particles entering the channel. The determination of deposition fraction can be written as follows.

$$\left[\begin{array}{l}\text{Fraction of deposition at} \\ \text{given axial distance X}\end{array}\right] = \frac{\left[\begin{array}{l}\text{total number of particles deposited on} \\ \text{the wall from inlet to X}\end{array}\right]}{\left[\begin{array}{l}\text{total number of particles entering} \\ \text{the channel at inlet}\end{array}\right]}$$

$$= \frac{\int_{-h}^{y_l} \rho_p u_p \, dy + \int_{y_u}^{h} \rho_p u_p \, dy}{\int_{-h}^{h} \rho_p u_p \, dy} \tag{4.20}$$

where y_l and y_u are two critical numbers which are discussed as follows.

According to the limiting trajectories by Pich [9], it is defined that those particles entering the channel between -h and y_l will deposit on the lower channel wall, those particles entering the channel between y_u and h will deposite on the upper channel wall, and those particles entering the channel between y_l and y_u will penetrate the channel. It is noted that, although the flow field is symmetric, the particulate distribution will not be symmetric because of the coupled forces.

The dimensionless form of fraction of particle deposition can be written as follows.

$$\text{Fraction of particle deposition} = \frac{\int_{-1}^{Y_l} \rho_p U_p \, dY + \int_{Y_u}^{1} \rho_p U_p \, dY}{\int_{-1}^{1} \rho_p U_p \, dY} = 1 - \frac{1}{2}(Y_u - Y_l) \tag{4.21}$$

where $Y_l = y_l / h$, $Y_u = y_u / h$, and $U_p = 1$ at $X = 0$.

CHAPTER 5

RESULTS AND DISCUSSIONS

In this chapter the results of numerical simulation on the deposition of particles in turbulent channel flows are presented and discussed. First the turbulence model used in this analysis is tested and compared with experimental data. The flow fields of parallel-plate channel and two types of divergent channels are compared. Then the particle depositions from turbulent channel flows in two types of divergent channels are compared and the influence of flow fields to particle motion is discussed.

5.1 Comparison of Numerical Simulation and Experiment

To test the turbulence model employed in this work, the experimental results of Acharga et al [42] is compared with the numerical simulation using the turbulence model described in chapter 4 section 4.2.

The test section as shown in figure 5.1 consists of a parallel plate channel with a two-dimensional square rib mounted on the lower surface of the wall. This problem involves flow separation, reversed flow and flow reattachment due to the rib. The square rib with width and height of h = 6.35 mm is placed 15 h downstream of the inlet plane of the channel. The channel is spaced at H = 61 mm. Air at 22^{0} C and 1 atmospheric pressure enters the channel with uniform velocity at 3.6 m/s. The flow is considered to reach its prescribed fully-developed velocity profile at 30h down stream of the rib. Under these conditions the Reynolds number based on the height of the rib is 1500.

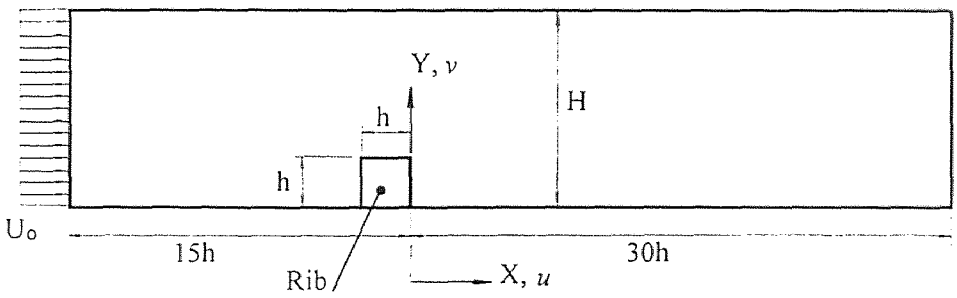

Figure 5.1 Test section of experimental measurement

The main concern is the flow reattachment which includes the reversed flow region behind the rib. The comparison of flow velocity profile from the numerical turbulence model with the experimental measurement is shown in figure 5.2.

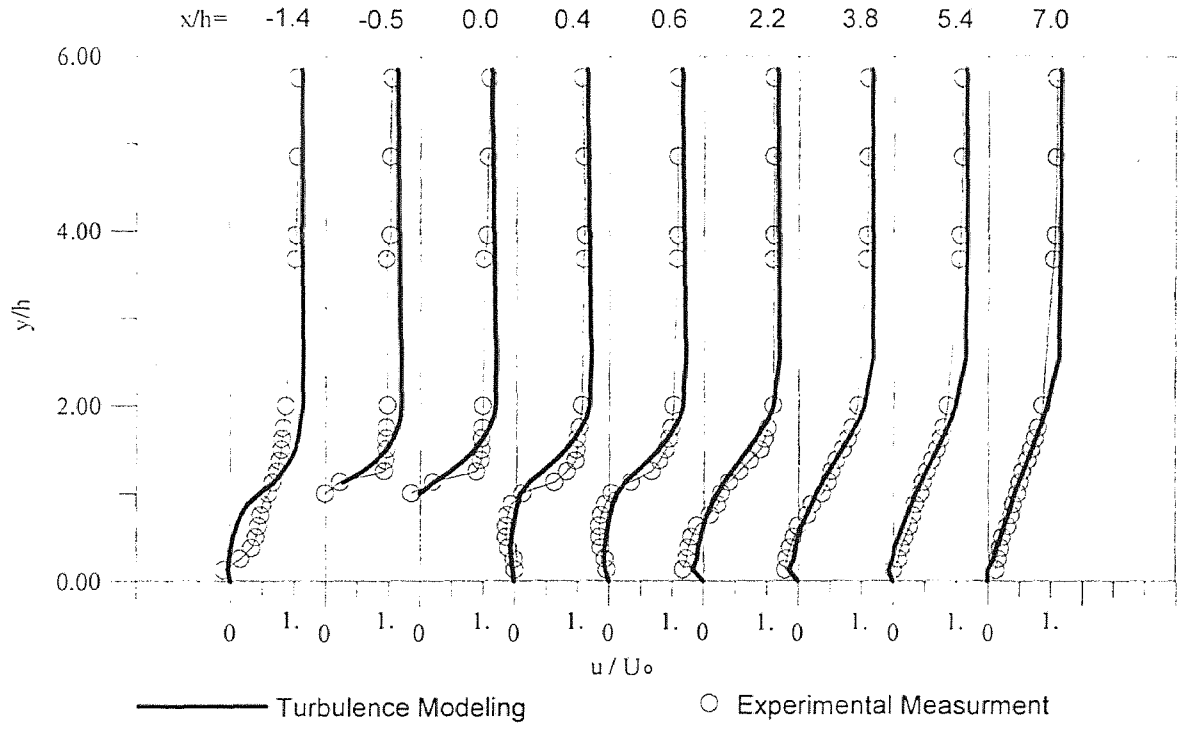

Figure 5.2 Comparison of velocity profile from experimental measurement and numerical simulation

The comparison in figure 5.2 includes the region before the rib, the rib, and the region of flow reattachment. It is clear that the result of the numerical simulation is in good agreement with the experimental measurement. The measured length of flow reattachment is 6.3h ± 0.9h [42]. The length of flow reattachment from the numerical simulation is 7.0h. The length of flow reattachment is defined as the distance measured from the rib to the point where the reversed flow ends.

Observing figure 5.2, the largest difference between the numerical simulation and experimental measurement is from x/h = -1.4 to x/h = 0 where fluid approaches the rib, moves against it and passes over it. Fluid below the line of the top surface of rib, i.e. $y/h \leq 1$, must move upward or backward after it reaches the rib. Therefore the mechanism of flow motion in this region is as complicated as the flow reattachment. However, its importance in practical application and theoretical research is much less than that of the flow reattachment.

From figure 5.2 it is clear that, after the flow passes the rib, the velocity profiles of the numerical simulation are very close to the experimental measurement. The difference between them can be found in three regions which are the first region of $y/h \leq 1$, the second region of y/h = 1 to 2 and the third region of y/h = 2 to 4. In the first region which is the reversed flow region the numerical simulation under-predicts the flow velocity. In the second region the result of the numerical simulation is still underpredicted while in the third region the numerical simulation overpredicts the flow velocity. Referring [42] this difference can be considered as the characteristic of κ-ε turbulence modeling. Acharga et al [42] performed a numerical simulation using a modified κ-ε model and obtained a similar

result. In conclusion, the numerical turbulence model used in this analysis is considered reliable.

5.2 Comparison of Flow Fields

The flow development in a divergent channel differs from that of a parallel-plate channel considerably. In this section flow fields in two divergent channels and a parallel-plate channel are discussed and compared.

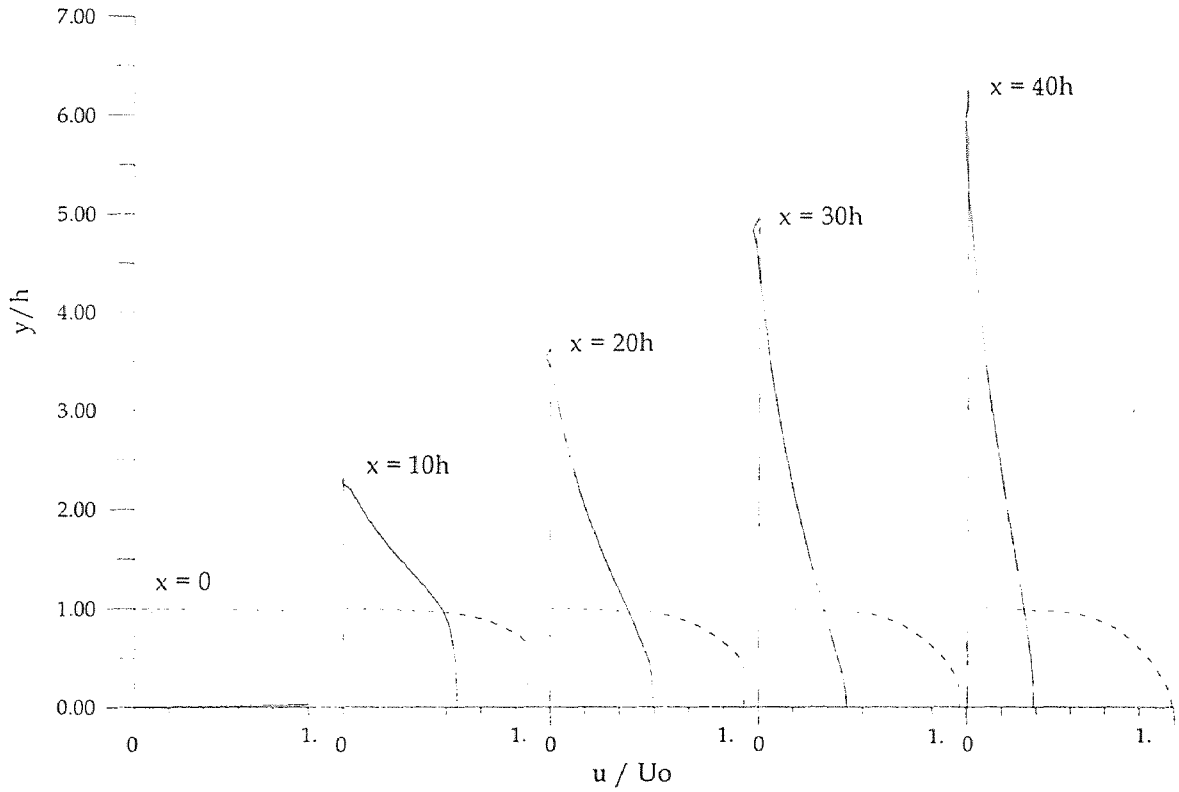

Figure 5.3 Developing of velocity profile (u) in a parallel-plate channel and a divergent channel with $\theta=7.5^{\circ}$

Figure 5.3 show the velocity development in a parallel-plate channel and a divergent channel having 7.5° half divergent angle. In a parallel-plate channel the width

and the flow area are constant while in a divergent channel the channel width and the flow area are increasing in the direction of flow. As a uniform flow enters a channel the boundary layer grows near the wall and tends to force the fluid to move toward the center core. Thus the center-line velocity in a parallelflow -plate channel increases as the boundary layer grows downstream. The pressure decreases downstream in a parallel-plate channel.

However in the 7.5° divergent channel the increase in flow area reduces the overall velocity and increases the pressure. For fluid near the wall, the flow may start to reverse itself or reach the point of separation which is defined as the point at which the velocity gradient, du/dy, is zero at the wall. The point of separation for a 7.5° divergent channel is at $x = 10h$ where h is the half width of the channel at the inlet plane. For flow beyond the point of separation, a thin layer of reversed flow builds up. Particles in this region will experience a retarded force and slow down their axial velocity and may increase the deposition. However the channel width is also increasing and a particle in a divergent channel will have to travel a greater distance to the wall than that of a particle in a parallel-plate channel. The combined effects of flow velocity and channel width on the deposition of particles under viscous, gravity, electrostatic and inertia forces has to be investigated.

Moreover, as shown in figure 5.4, the turbulent flow in a divergent channel moves forward and outwards. It is thought that the particle suspension will be carried by the fluid phase toward the channel walls and the particle deposition will be enhanced by the turbulent flow field.

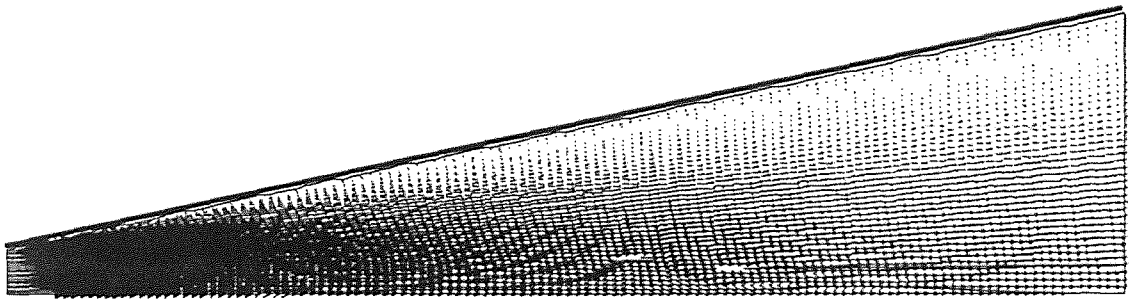

Figure 5.4 Vector of flow velocity in a divergent channel with θ=7.5°

As mentioned in the previous chapter, the first type of divergent channel is straight from the inlet to the outlet with axial length 40*h*. The second type of divergent channel is the first one with a parallel section connected to the outlet. Although both channels have the same divergent angle, the reversed flow regions in both channels are not the same. As shown in figure 5.5(a) through 5.5(c), the reversed flow region in the first type channel is a little bigger than that in the second type channel.

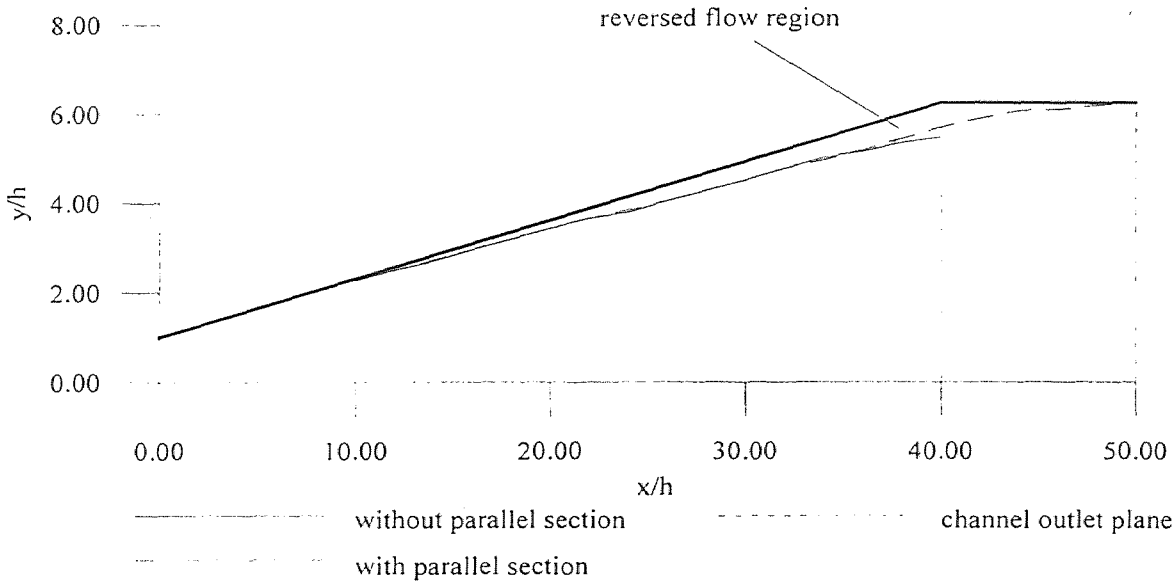

Figure 5.5(a) Reversed flow region in two types of divergent channel with θ=7.5°

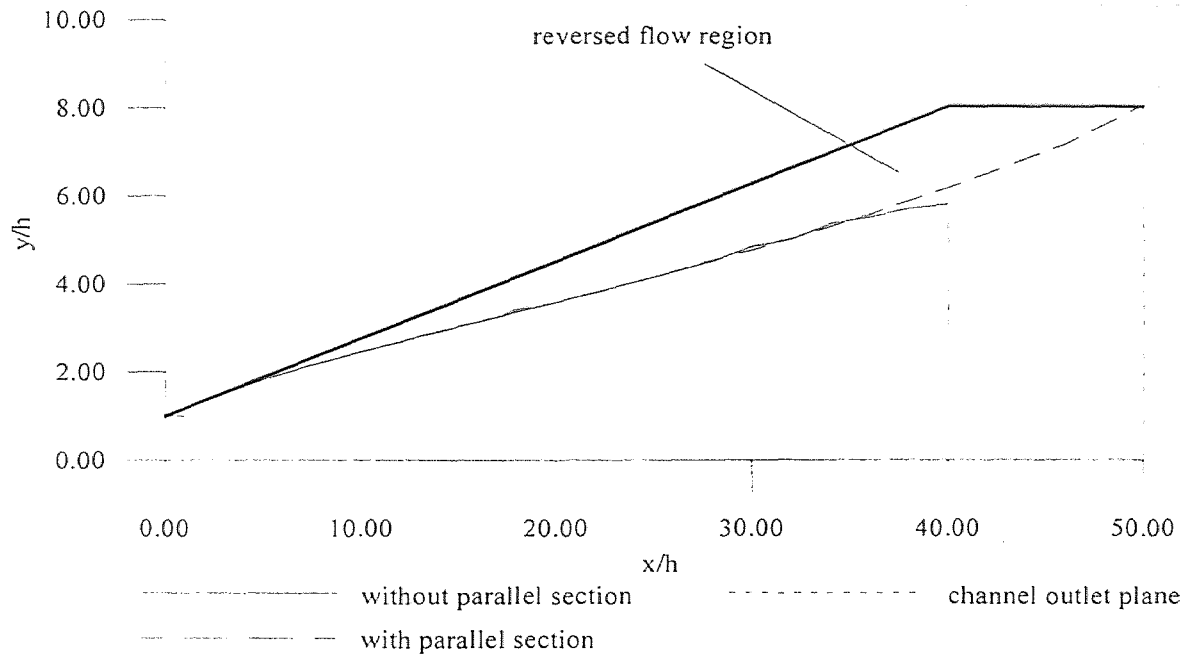

Figure 5.5(b) (*continue*) Reversed flow region in two types of divergent channel with $\theta=10^{o}$

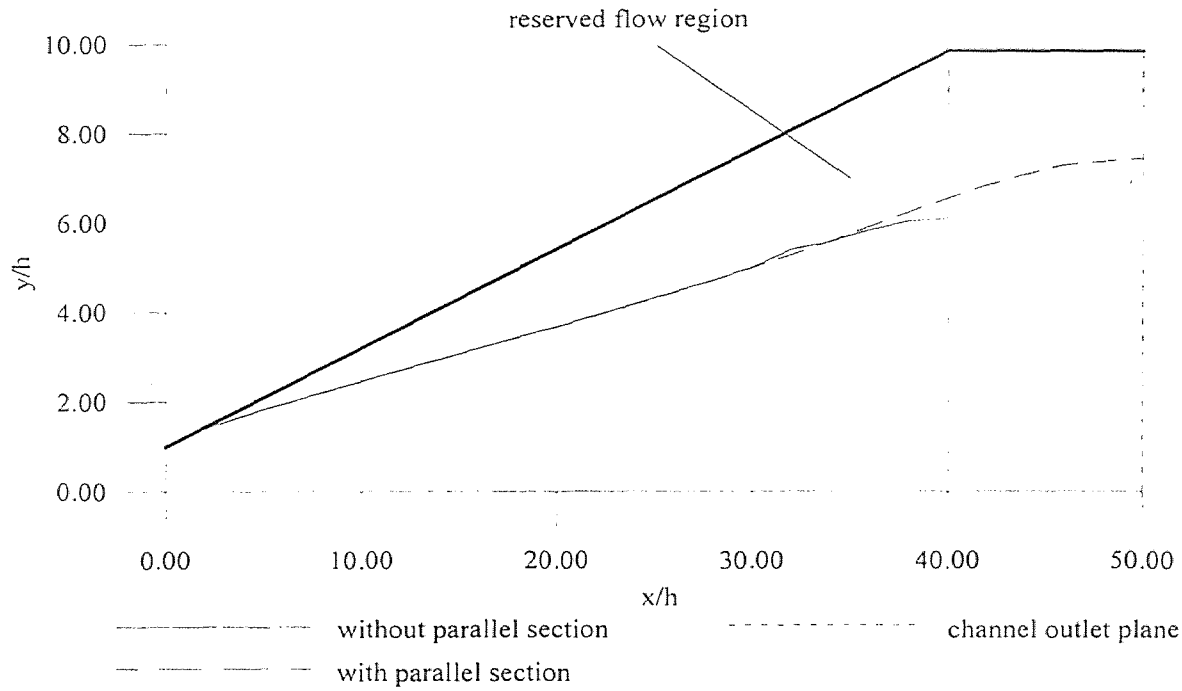

Figure 5.5(c) (*continue*) Reversed flow region in two types of divergent channel with $\theta=12.5^{o}$

As shown in figure 5.5(a), in a channel with 7.5° half divergent angle, the flow separation occurs at a distance of $10h$ and the reversed flow region is not large in both type of divergent channels. The main interest is that, in a second type channel, the reversed flow region decreases in the parallel section until it reaches the outlet plane. While the reversed flow region in the first type channel continues to increase until it reaches the outlet plane.

Figure 5.5(b) shows that the reversed flow region in a channel with a 10° half divergent angle increases significantly. The flow separation occurs at distance of $4h$ that is much closer to the channel inlet plane. In a second type channel, the reversed flow region decreases in the parallel section until it reaches the outlet plane. It can be considered that, when fluid goes into the parallel section, the decrease of turbulence dissipation is faster than the production of turbulence. Therefore the fluid phase in this section might become relaminarized in the parallel section.

Figure 5.5(c) shows the comparison of the reversed flow region in a channel with a 12.5° half divergent angle. The flow separation occurs at distance of $2h$ in the first type channel and it occurs at distance of $4h$ in the second type channel. The reversed flow regions in both channels are very close and much larger than the previous cases. Almost 1/3 of the channel area is covered by the reversed flow region. Furthermore the reversed flow region in the second type channel does not decrease in the parallel section but still occupies 25% of the channel area. This is understood that, due to the larger divergent angle, the decrease of turbulence dissipation is not greater than the production of turbulence. Therefore the flow field in the parallel section can be considered to remain at a certain degree of turbulence. It can be considered that the flow fields in both channels are not different from each other.

In conclusion, the divergent angle affects the flow field in the divergent channel significantly. In the cases of channels with 7.5° and 10° half divergent angles, the parallel section plays an important role but it has less effect on a channel with a 12.5° half divergent angle. This is due to the larger divergent angle which generates instability in the flow field. The area of reversed flow region increases with increasing divergent angle.

5.3 Particle Deposition Distance

When a particle enters a channel, it continues to move downstream until it reaches the channel wall and deposits on the wall or it may leave or penerate the channel without reaching the wall. The axial distance traveled by the particle from the inlet plane of a channel to the point of deposition is defined as the deposition distance Xd which is a dimensionless parameter obtained by dividing the actual axial distance by half the channel width, h, at inlet plane of a divergent channel. This distance depends on the initial position of the particle at the inlet plane and also depends on parameters such as inertia parameter S, gravity parameter G and charge parameter Q.

As shown in figure 5.6, the deposition distance changes dramatically with changes in the gravity parameter G, charge parameter Q, and particle inertia parameter S. It is noted that, although the stalled flow field in a divergent channel may slow down a particle, the increase in channel width downstream also affects particle deposition because a particle must travel a longer distance in a divergent channel to reach the channel wall than it does in a parallel-plate channel.

Another important thing that must be noticed is that a particle which is closer to the upper channel wall may not deposit on the wall faster than others do on the lower wall. The

reason is that when a particle moves near the upper wall surface, the fluid phase applies a viscous force to push it away from the wall in a parallel-plate channel and push it toward the wall in a divergent channel. Meanwhile, the induced electrostatic image force pulls it toward the wall surface and the gravity force pulls it away from the upper wall at the same time. These combined forces may cancel one another and allow it to travel farther downstream.

As discussed in chapter three, the electrostatic image force induced by a particle on the walls of a divergent channel not only pulls the particle toward the wall surface, but also pulls it backward to the channel entrance. Therefore its trajectory is affected by many factors. The different combinations of the coupled effects of viscous, gravity, particle inertia and electrostatic image forces produce different influences on the mechanism of particle motion.

In order to compare the effects of channel geometry on the motion of a particle we may compare the motion of a particle in a parallel-plate channel to that in a 7.5^{o} half divergent angle channel. From the equations of motion (eq. 3.2 and 3.3) we find that viscous, gravity and image forces affect the motion of a particle. The viscous force depends on v (the fluid velocity in the y-direction) and u (the fluid velocity in the x-direction) respectively. The gravity force is a constant for a given particle. The image force on a particle toward a wall depends on the distance between the particle and the wall.

From the flow analysis using *FIDAP* software package we find that near the wall v is directed away from the wall in the parallel-plate channel and is toward the wall in a divergent channel. The axial velocity u decreases near the wall at a lower pace in the parallel-plate channel than that in a divergent channel. Thus the fluid velocity tends to

enhance the deposition in a divergent channel. However, the velocity v in the reversed flow region in a divergent channel tends to move away from the channel wall so that the reversed flow region may give a negative influence on particle deposition.

Unlike in a parallel-plate channel where the particle experiences relatively constant or slightly increased image force as it moves downstream, a particle in a divergent channel will experience a smaller image force toward the wall due to increase in the distance between the particle and the wall. Moreover there is a negative image force in the x-direction in a divergent channel. Therefore the effect of the image force may reduce the deposition in a divergent channel.

The combined effects of flow velocity and geometrical changes on the particle deposition are presented in next section.

5.3.1 Effects of Particle Size

In this section the relation between parameters S, G, Q and particle size is discussed before further discussion in order to give a better understanding about the relation of these parameters. Referring to chapter 4, the definition of dimensionless parameters S, G and Q are:

$$S = \frac{\text{inertia force}}{\text{viscous force}} = \frac{m_p u_0}{6\pi\mu d_p h} \tag{4.11}$$

$$G = \frac{\text{gravity force}}{\text{viscous force}} = \frac{m_p g}{6\pi\mu d_p u_0} \tag{4.12}$$

$$Q = \frac{\text{charge force}}{\text{viscous force}} = \frac{q^2}{(4\pi\,\varepsilon_0)(6\pi\mu\, d_p\, u_0)\, h^2} \qquad (4.13)$$

Based on a spherical particle with the same particle composition, i.e. same density, particle mass m_p is proportional to particle volume and particle charge q is proportional to particle surface area, the volume and surface of a sphere object with diameter d_p are:

$$\text{Volume} = \frac{1}{6}\pi\, d_p^3 \qquad \text{and} \qquad \text{Surface} = \pi\, d_p^2 \qquad (5.1)$$

From equations 4.11, 4.12, 4.13 and 5.1 it is very clear that for flow in a given channel particle inertia is proportional to d_p^3, gravity force on a particle is also proportional to d_p^3, electrostatic charge of a particle is proportional to d_p^2 and charge force on a particle is proportional to d_p^4, and viscous force is proportional to d_p only; where d_p is the diameter of a spherical particle.

Therefore when the particle diameter increases by a factor of 10, those dimensionless parameters will become S'=100S, G'=100G and Q'=1000Q where S', G' and Q' represent the parameters of larger particles. If the particle diameter decreases as a factor of 10, then those dimensionless parameters will become S'=0.01S, G'=0.01G and Q'=0.001Q. The new smaller particle becomes another combination of parameters. It is obvious that, for the same particle composition, S and G change at the same rate but Q does not. Moreover, if the density of particle composition increases, G and S increase proportionally but Q depends on the electrostatic charge of the particle.

From the above discussion it is concluded that a larger particle gives higher Q and, thus, a higher image force per unit mass than a smaller particle does under same conditions. Therefore a smaller particle is more sensitive to the influence from image forces than a larger particle. In other words, a particle with greater S and G is less affected by change of Q than a particle with small S and G. The following discussions are intended to investigate the significance of gravity, inertia, electrostatic image forces and channel configuration on a particle deposition distance.

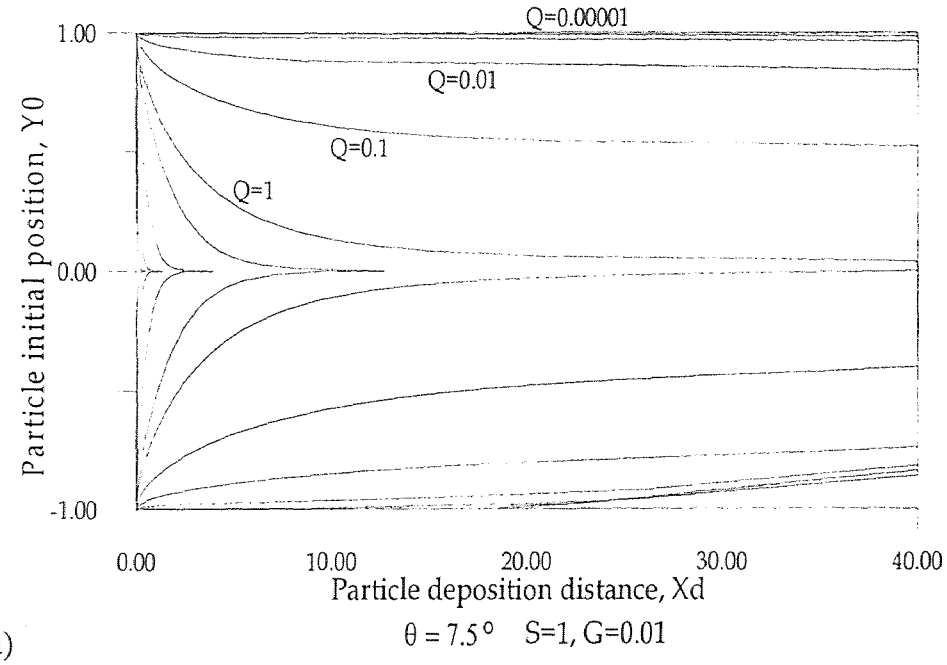

(a)

Figure 5.6 Deposition distance with S=1 and variable G and Q

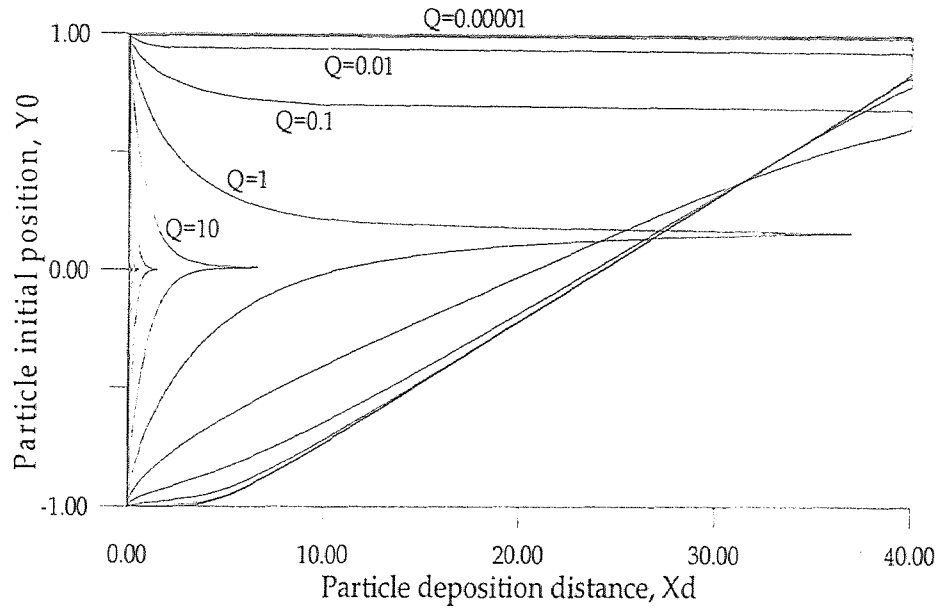

(b) $\theta = 7.5°$ S=1, G=0.1

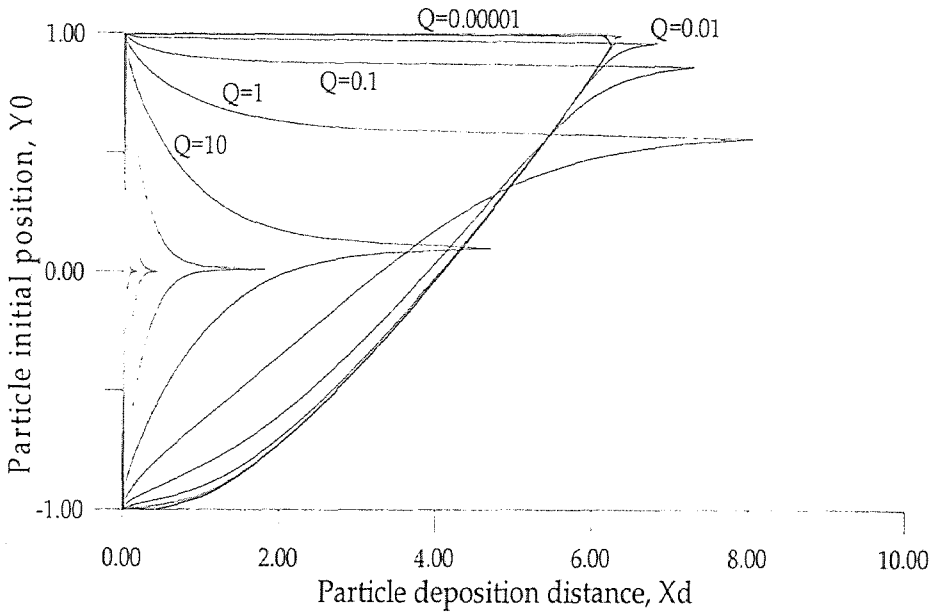

(c) $\theta = 7.5°$ S=1, G=1

Figure 5.6 (*continue*) Deposition distance with S=1 and variable G and Q

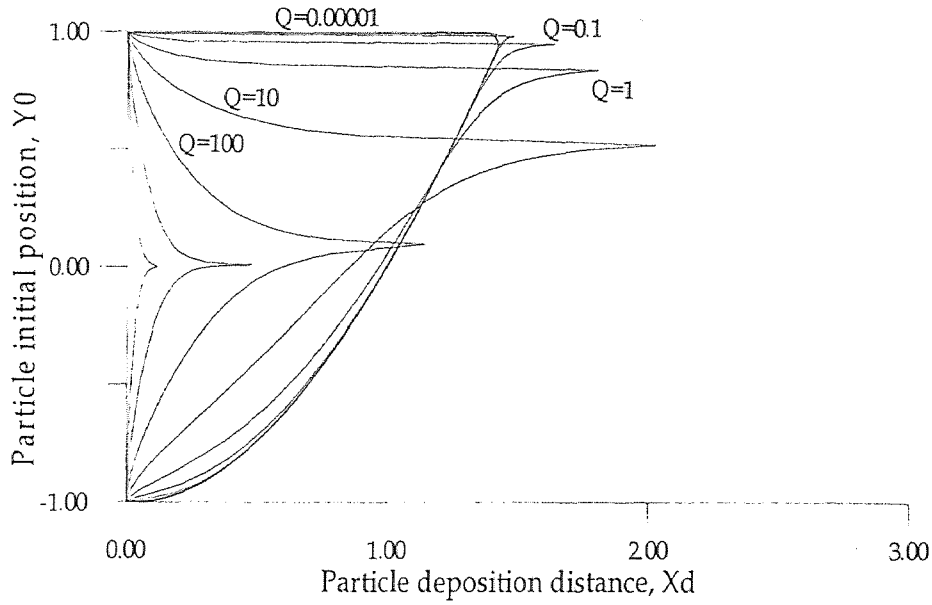

(d) $\theta = 7.5°$ S=1, G=10

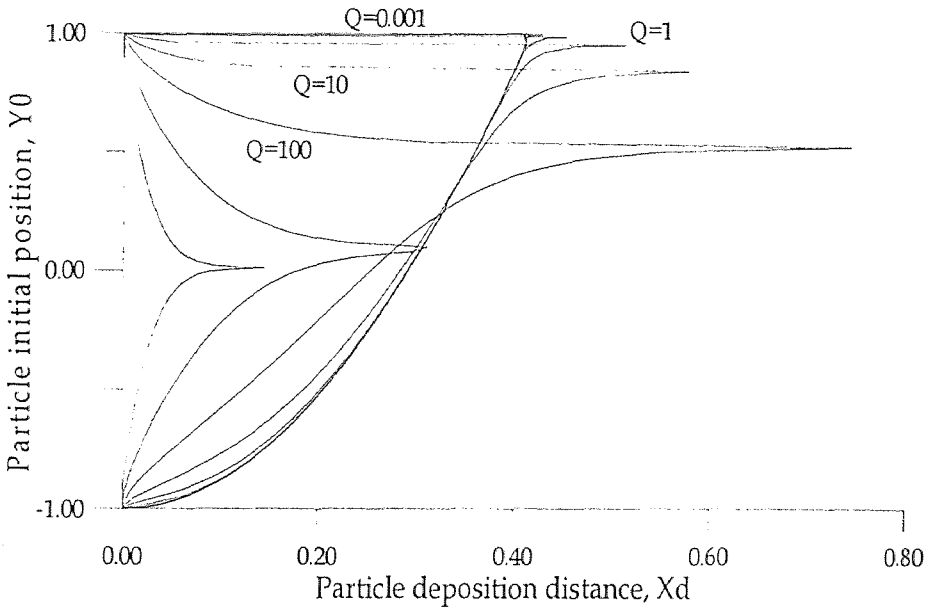

(e) $\theta = 7.5°$ S=1, G=100

Figure 5.6 (*continue*) Deposition distance with S=1 and variable G and Q

5.3.2 Effects of Gravity Force

Figures 5.6(a) through 5.6(e) show curves of particle deposition distance in a divergent channel (of the first type) with $\theta=7.5^{o}$, S=1 and variable Q and G. It is interesting to note that when the gravity force is G=0.01 all curves are almost symmetric with respect to the center line of the channel as shown in figure 5.6(a). It can be considered that a small gravity force has very limited influence on particles thus they are mainly dominated by the image force. Since the channel is symmetric with respect to its center line, curves of particle deposition distance are also symmetric. The only minor asymmetric part in figure 5.6(a) is for particles very close to the lower wall where the gravity force has taken its toll and attracts a few more particles on the lower channel wall.

At higher value of G, deposition distance curves are no longer symmetric except those with large Q. Observing figures 5.6(a) through 5.6(e) which have the same S with increasing G, the change in the shape of the deposition distance curve from G=0.01 in figure 5.6(a) to G=0.1 in figure 5.6(b) is very striking. It is noted that as the gravity force is increasing, only particles with high value of Q remain symmetric. For example, it takes $Q \geq 1$, 10, 100 and 1000 to remain symmetric for G=0.1, 1, 10 and 100 respectively. Thus for $Q/G \geq 10$ the gravity effect may be neglected.

Another noticeable effect is the balance between gravity force and image force from the upper wall. Observing figure 5.6(b), (c), (d) and (e) it is found that a particle with Q/G=1 near the upper wall travels the longest distance. This is understood as a particle is in an equilibrium situation such that it may travel a very long distance until the balance between gravity force and image force from the upper wall is broken. As mentioned at the beginning of section 5.3, in a divergent channel gravity force in a given flow is constant and

image force depends on the distance between a particle and the channel walls. When a particle travels a long distance in a divergent channel, the image force decreases as the channel width increases. Therefore the balance between gravity and image forces disappears and that particle is out of equilibrium and will move toward a wall.

Increasing the gravity force improves particle deposition in terms of shorter deposition distances at any given Q. For example, taking Q=1 from figure 5.6(b) through 5.6(e) the longest deposition Xd is 37.5, 8.1, 1.8 and 0.52 for G=0.1, 1, 10 and 100 respectively. Figure 5.7(a) through 5.7(c) show deposition distances for Q=1 and $\theta=7.5^{o}$ under different G and S. It is very clear that when the ratio Q/S is small, i.e. 0.1 or smaller, the gravity force strongly affects the particle motion and results in a rapid decrease in deposition distance as G is increased to be $G/S \geq 1$. However, referring to section 4.2 and 5.3.1, the situation of $G/S \geq 1$ is hardly to be found for a particle suspension in a turbulent flow field with high initial velocity.

From these figures we can also discern the following facts. Firstly, when $Q/S \geq 1$; all particles are deposited in the channel for $G/S > 0.1$. Secondly, at the same G/S ratio the deposition distance is shorter when the value of G is higher. Therefore, if we increase the diameter of a particle in a channel flow its G/S value remain the same but the larger particle will have shorter deposition distance since the larger particle has a higher G value. This is true when Q remains constant and will be also true when Q increases.

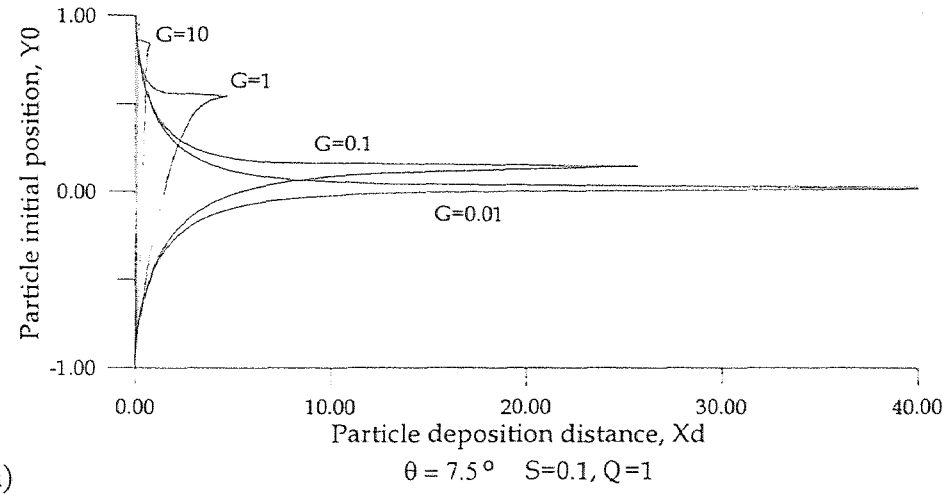

(a)

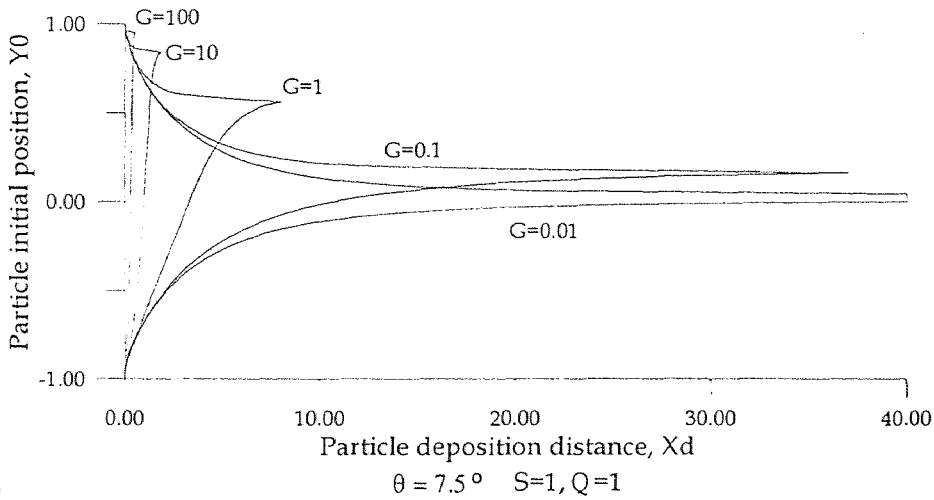

(b)

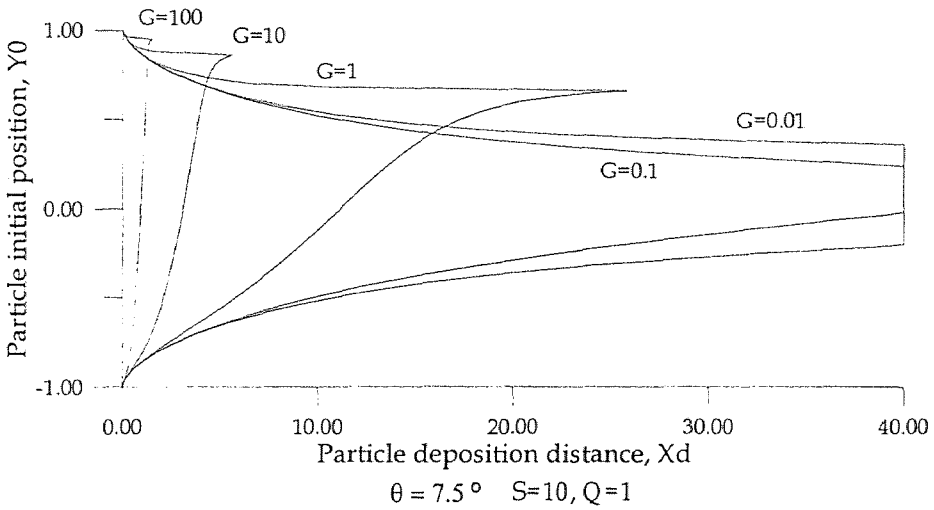

(c)

Figure 5.7 Deposition distance curves with Q=1 and variable S and G

In summary, the gravity force makes the deposition distance curve skew toward the upper wall and become asymmetric. Thus more particles will deposit on the bottom wall of the channel. When $Q/G \geq 10$ the gravity effects may be neglected and the deposition distance curve is almost symmetric with respect to the center line. Larger particles give a higher G value but its S value also increases in the same order and G/S remain the same. However, a larger particle will deposit in a shorter distance than a smaller particle.

5.3.3 Inertia Force Effects

Figures 5.8(a) through 5.8(e) present deposition distances at G=1 under various S and Q. It is seen that as S increases while Q maintains a constant, deposition distance increases and more particles penetrate the channel. In other word, for particles with G constant and S increasing it requires higher Q to provide the same amount of deposition. For example, in figure 5.8(e) at G=1 and S=100 it takes $Q > 10$ to deposit all particles but for cases with $S \leq 10$ (i.e. figures 5.8(a) through 5.8(d)) all particles are deposited even if Q=0. Physically, to maintain G constant and S increasing, we may keep the particle size constant and reduce the channel half width h. However by reducing h by a factor of 10, we find that S will increase by a factor of 10 and with no change in charge q then Q will increase by a factor of 100 which will cause more deposition. From figure 5.7(a) through 5.7(c) and figure 5.8(a) through 5.8(e) it was found that when $S/G \leq 10$ all particles are deposited in a divergent channel with $\theta \leq 12.5^{o}$.

It can be said that as the inertia is increased the deposition distance also increases and the deposition distance curve is stretched in the axial direction which implies less deposition. For example in figure 5.9 where the effects of S on deposition distance at Q=1

and G=1 are displayed, the deposition distance Xd = 3.3, 4.7, 8.1 and 26 for S=0.01, 0.1, 1 and 10 respectively. When S=100 in figure 5.9, most particles penetrate the channel. As a mater of fact it was found from figure 5.8(e) that unless Q is sufficiently higher some particles will penetrate the channel when S/G $\geq$100.

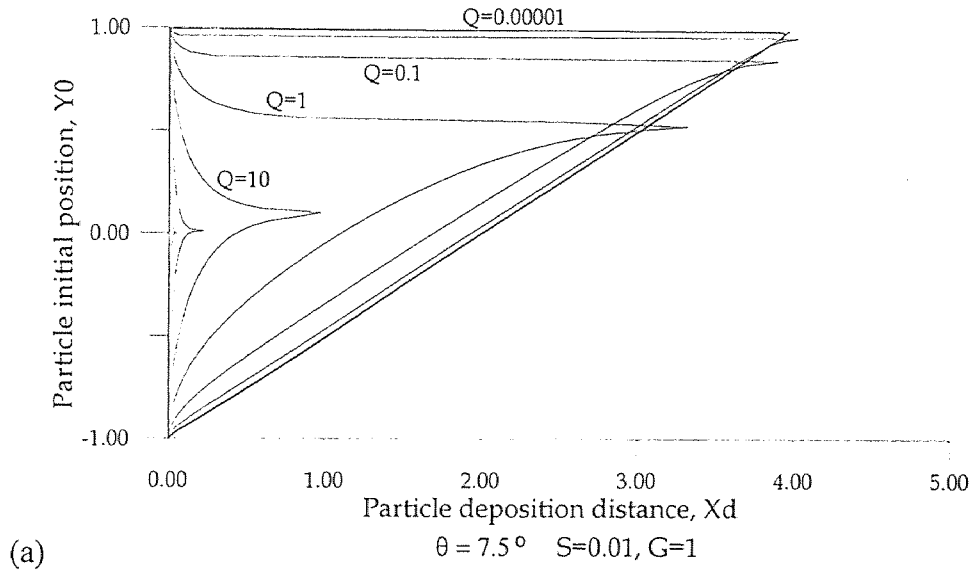

(a)

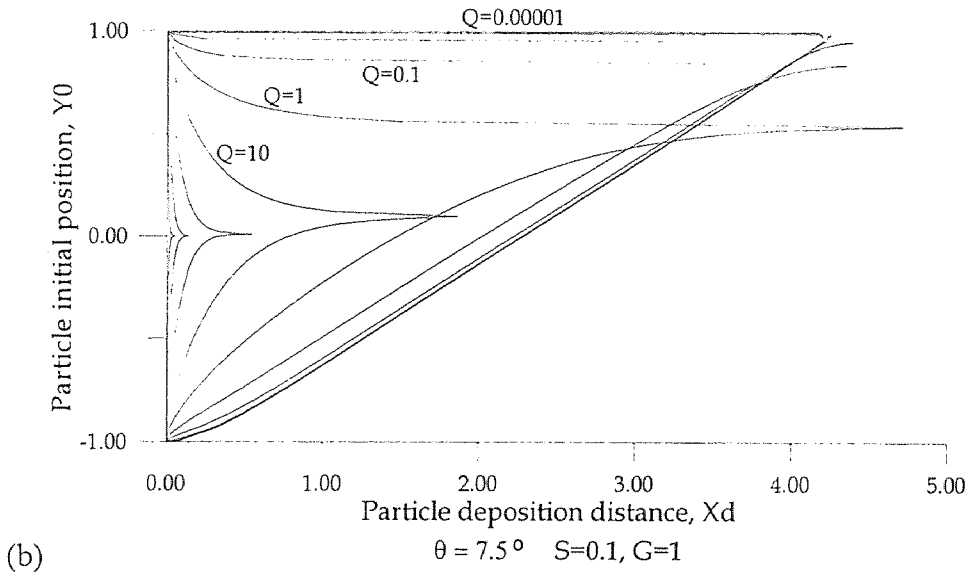

(b)

Figure 5.8 Particle deposition distance with G=1 and variable S and Q

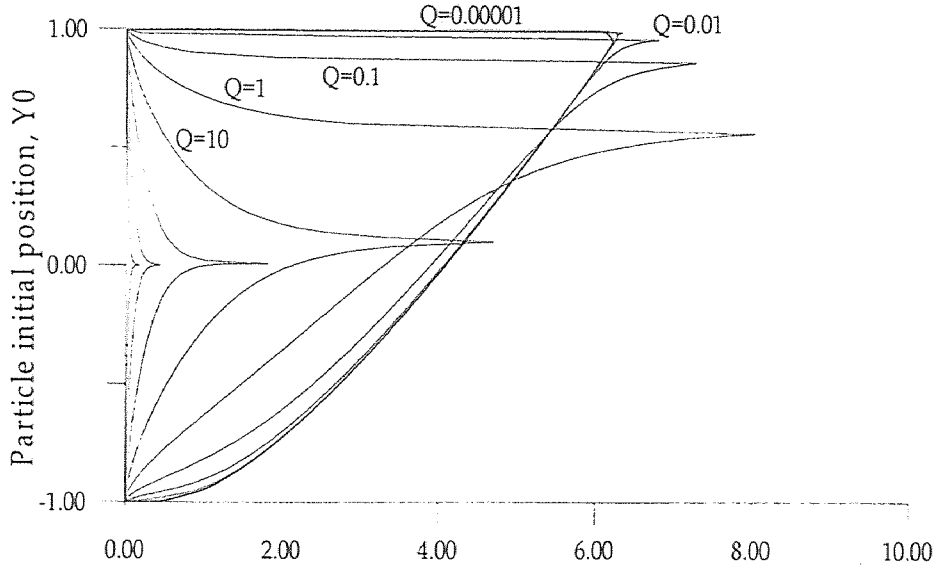

(c) $\theta = 7.5°$ S=1, G=1

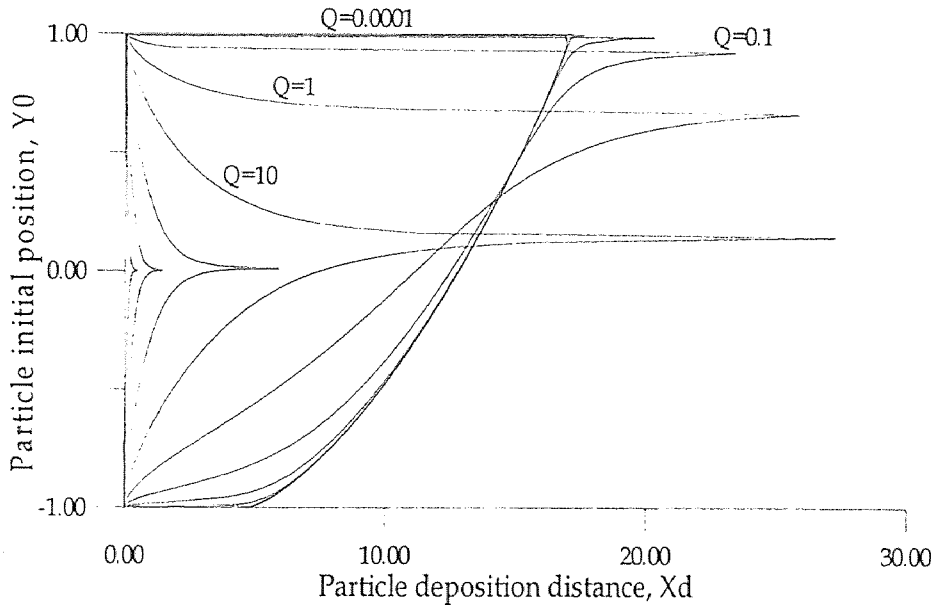

(d) $\theta = 7.5°$ S=10, G=1

Figure 5.8 (*continue*) Particle deposition distance with G=1 and variable S and Q

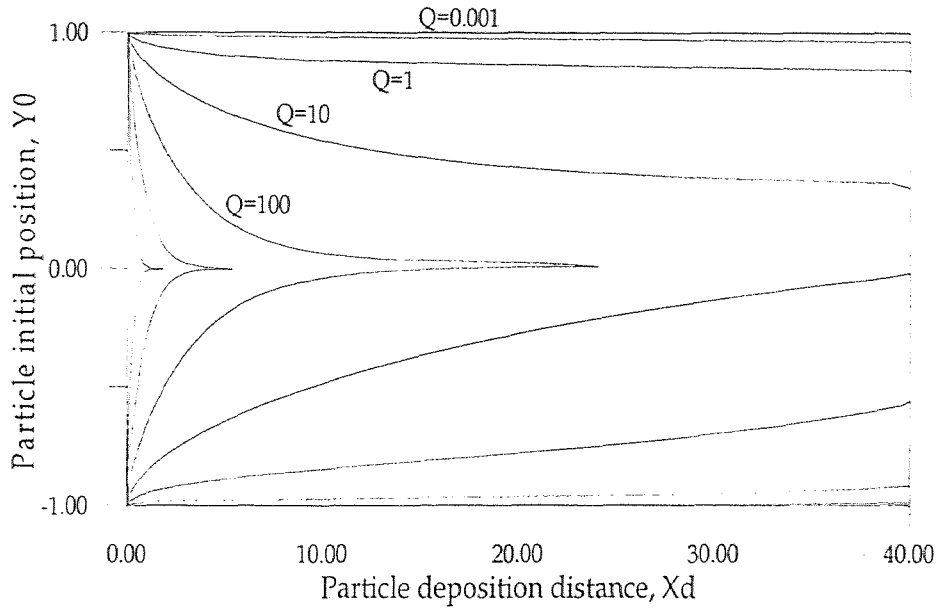

(e)

Figure 5.8 (*continue*) Particle deposition distance with G=1 and variable S and Q

From the definitions of S and G as shown in section 5.3.1 the inertia parameter S is proportional to the inlet velocity U_o but the gravity parameter is inversely proportional to U_o. Thus S is much prominent in a turbulent flow than that in a laminar flow since U_o is much higher in a turbulent flow.

In summary, the inertia force prevents particles from changing their velocity and increasing the inertia force increases the deposition distance and thus decreases the deposition. When the particle size is increased by a factor its S and G both increase at the same rate. However the increase in gravity effects overcome the increase in inertia effects and particles tend to have shorter deposition distances. When the flow velocity is increased the inertia effects increase and the gravity effects decrease. This will result in longer deposition distances.

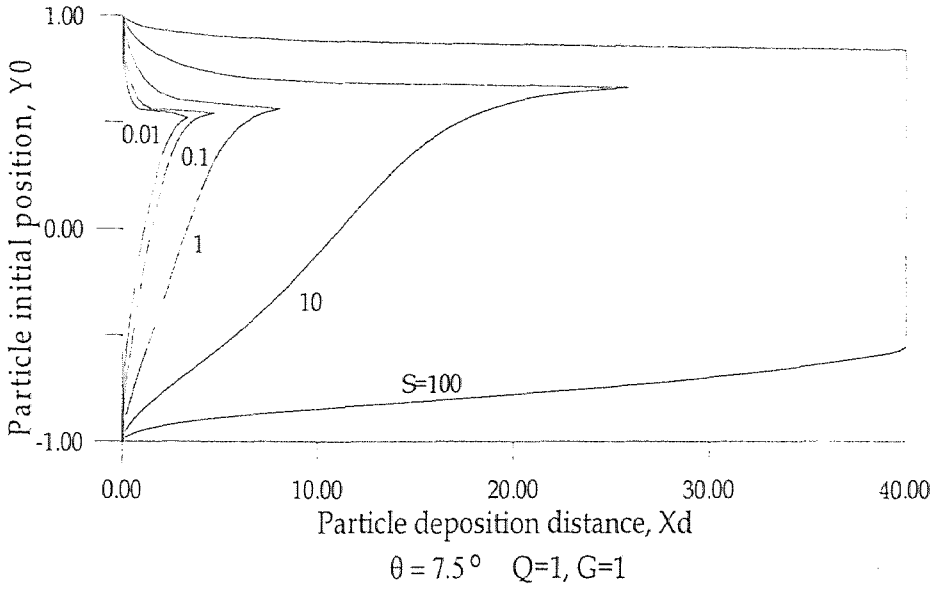

Figure 5.9 Particle deposition distance for Q=G=1 and variable S

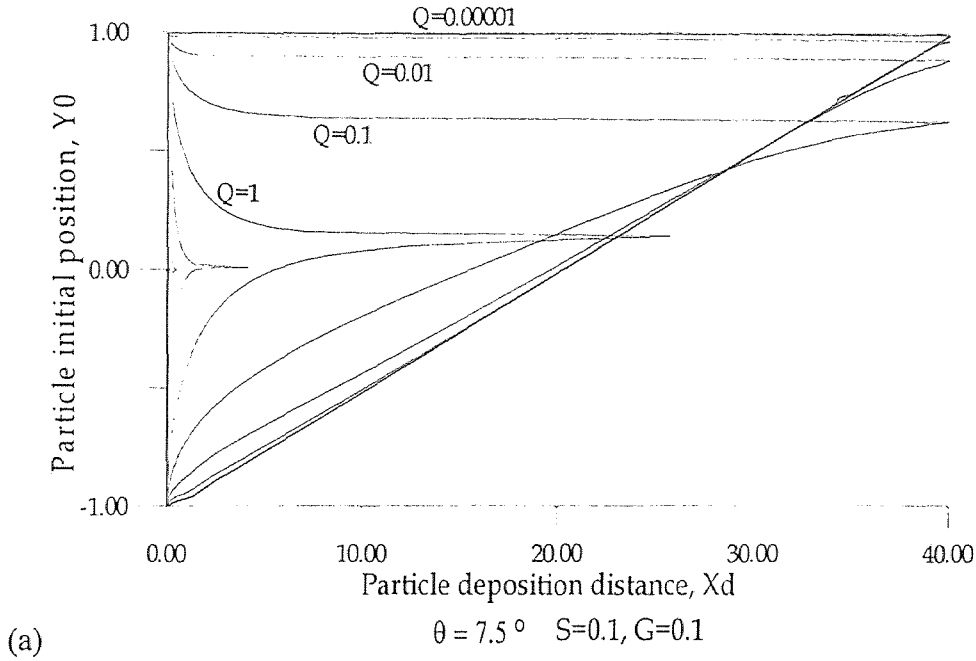

(a)

Figure 5.10 Particle deposition distance with S/G=1 and variable Q

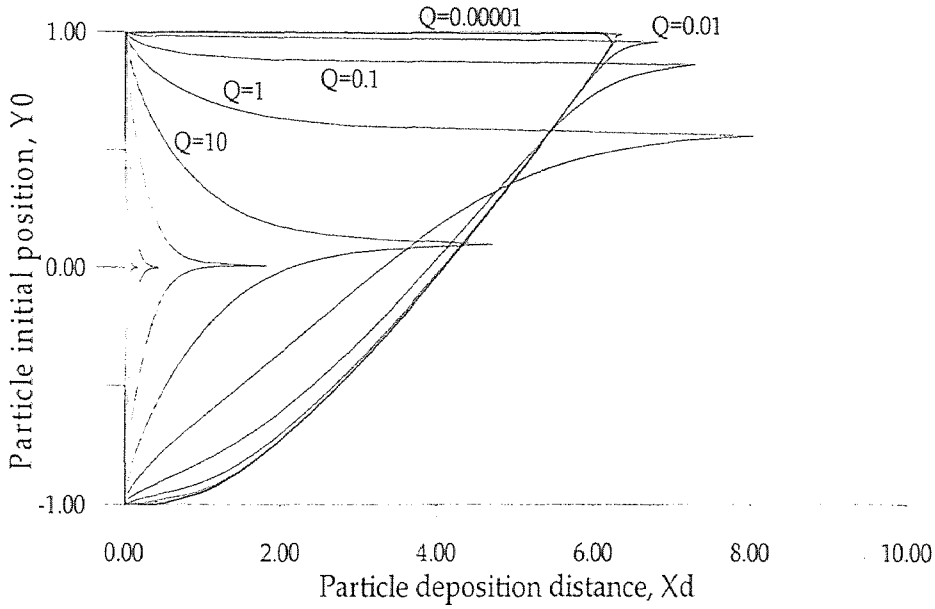

(b) θ = 7.5° S=1, G=1

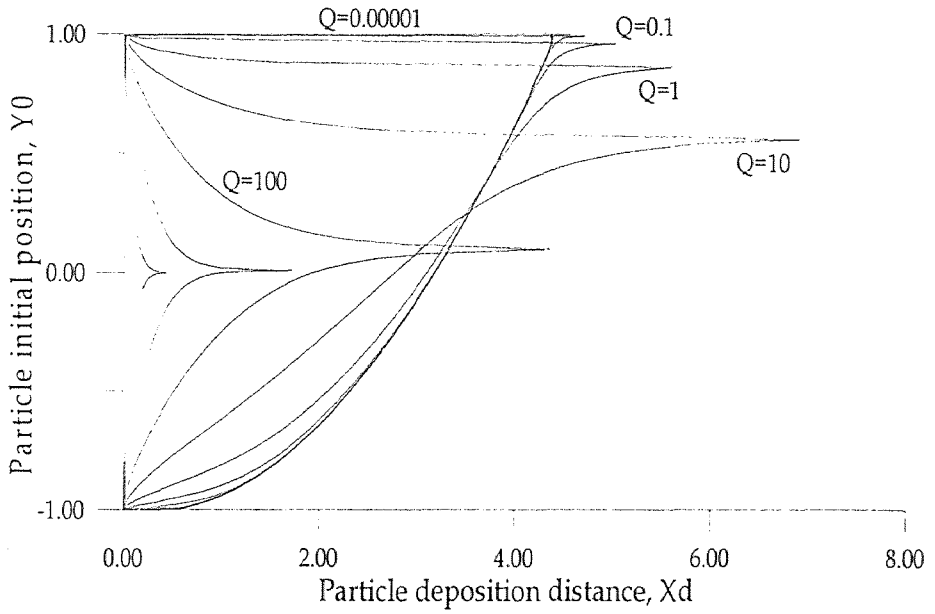

(c) θ = 7.5° S=10, G=10

Figure 5.10 (*continue*) Particle deposition distance with S/G=1 and variable Q

5.3.4 Effects of Image Force

Image force plays two different roles in the mechanism of particle deposition in a divergent channel. The first one is to attract particles toward the channel walls and the second one is to balance gravity forces by image forces from the upper wall resulting in a longest deposition distance. In figure 5.6(a) through 5.6(e) each figure has a particle deposition distance at S=1 and given G for variable values of Q. They have one thing in common; that, a larger Q makes particle deposition distance curves symmetric with respect to the centerline of the channel and gives shorter deposition distances. For example, from figure 5.6(c) with S=G=1 the longest deposition distance Xd is 0.45, 1.85, 4.7, and 8.1 for Q=1000, 100, 10 and 1 respectively and curves with $Q \geq 10$ are almost symmetric. When $Q < 1$ deposition distance curves are dramatically skewed toward the upper wall and become asymmetric. It is understood that as the image force decreases the gravity force dominates the particle motion and only the particle very close to the upper channel wall remains under the effect of the image force. As a particle moves downstream the image force decreases due to gradually increased channel width and the gravity force finally pulls that particle toward the bottom wall. This is observed in figure 5.6 that for $Q/G \leq 0.01$ almost all curves come together indicating the charge effects are negligible in comparison with the gravity effects.

Figures 5.10(a), (b) and (c) present deposition distances in a 7.5° divergent channel at S=G=0.1, 1 and 10 respectively under variable Q. It is seen that the deposition distance decreases with increasing particle size and this decrease is more significant at small particle size. The sensitivity of particle size to image force on particle deposition is shown in figure 5.11 in which the Y axis is the longest deposition distance and the X axis is the change of

image force in terms of the ratio of image force to gravity force Q/G. Therefore the slope of these curves can be considered as the rate of change of longest deposition distance with respect to the rate of change of image force. Observing figure 5.11, it is found that slope of curve 1 with S=G=0.1 is much greater than slopes of curve 2 with S=G=1 and curve 3 of S=G=10. Moreover, in figure 5.11 a change from one curve to another curve can be considered as a change of particle size. The change of slope from curve 1 to curve 2 is also much greater than that from curve 2 to curve 3. This has shown that the image force has greater influence on a smaller particle than a larger particle.

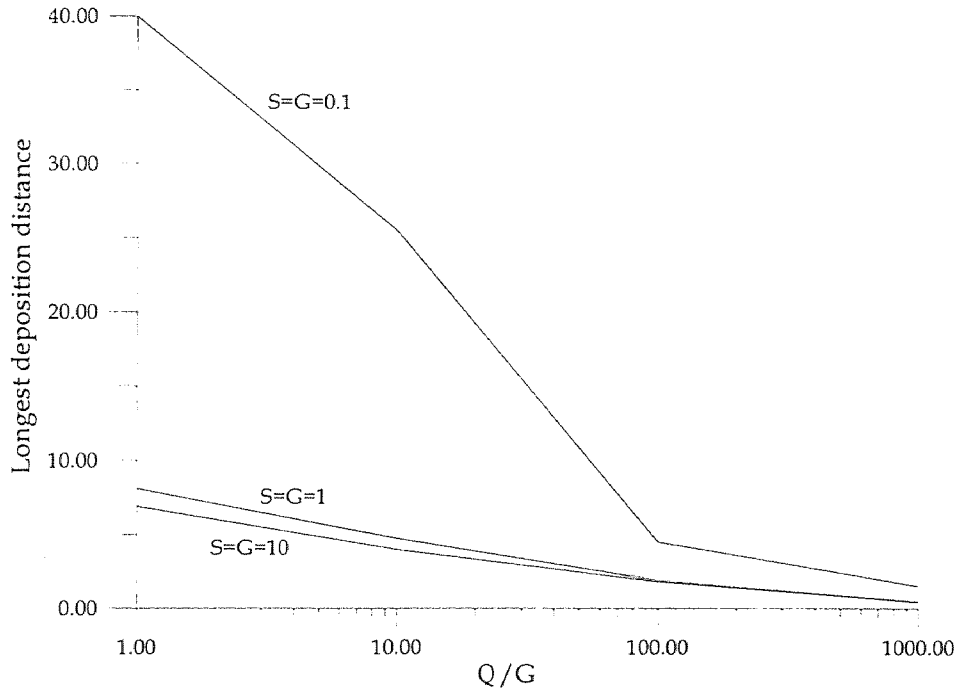

Figure 5.11 Effectiveness of image force on deposition at different S and G

As discussed in section 5.3.2 an important subject is the balance between gravity forces and image forces from the upper wall that results in the longest deposition distance. Referring to section 5.3.1 and taking S, Q and G at the same magnitude, i.e. S/G=1 and

Q/G=1, the curves with longest deposition distance is shown in figure 5.12 for S=Q=G=0.01, 0.1, 1, 10 and 100. From figure 5.12 it is found that deposition distance curve of G=0.01 is symmetric with respect to the center line of channel and less deposition as discussed in section 5.3.2. From figure 5.12 the longest deposition distance Xd is 40, 8.1, 6.9 and 6.85 for S=Q=G=0.1, 1, 10 and 100 respectively. It is concluded that, although the balance of gravity force and image force from the upper wall results in the longest deposition distance, as S, Q and G increase to certain magnitude, i.e. S=Q=G=1, the deposition distance decreases dramatically. As S, Q and G further increases the deposition distance decreases slightly. The upward image force that counteracts the gravity force affects particle deposition distance greatly if S and G are small.

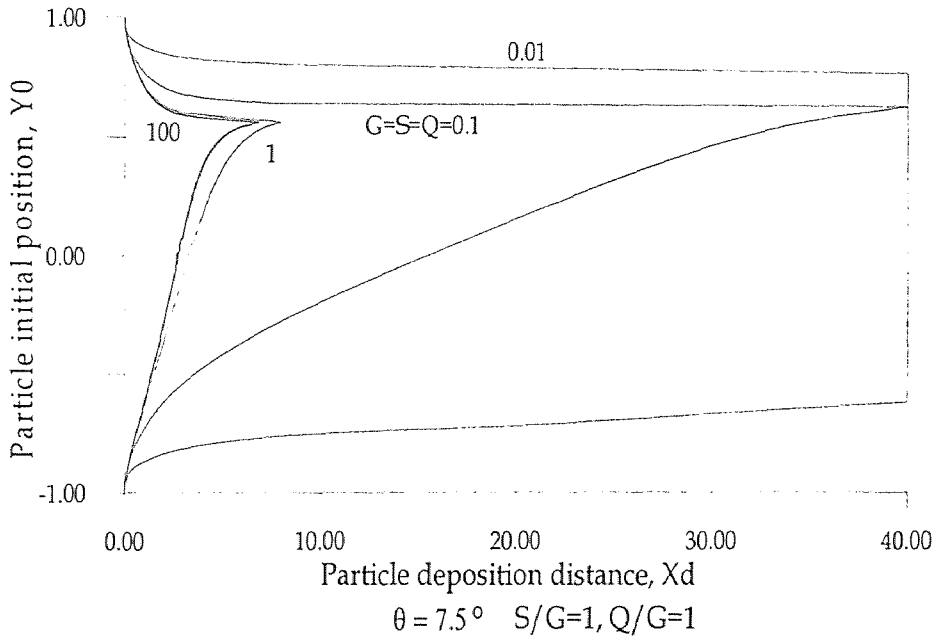

Figure 5.12 The longest deposition for S/G=1 and Q/G=1

In addition, from figure 5.11 it is interesting to find that the deposition distance decreases as Q either increases or decreases from the point of Q/G=1. As mentioned in the beginning of section 5.3, that gravity force is a constant and image force depends on the distance between a particle and the channel wall. Therefore increased Q breaks equilibrium, improves deposition and makes the deposition distance curve symmetric while decreased Q lets the gravity force take over and equilibrium disappears but makes deposition distance curve asymmetric. Observing figure 5.10 it can be considered that symmetric deposition distance curves with Q/G > 1 means deposition distributes on both upper and lower walls. The asymmetric deposition distance curve with Q/G < 1 means deposition mainly distributes on the lower channel wall. Observing figure 5.9 it is noted that when S and G are different the longest deposition distance does not occur for Q/G=1. From figure 5.9(d) the curve with Q=10, S=10 and G=1 has the longest deposition distance rather than that with Q=1, S=10 and G=1. This suggests that the ratio Q/G or Q/S determines the longest deposition in a divergent channel and it depends on S or G whichever is greater.

In conclusion, the image force is a crucial factor on particle deposition in a divergent channel and plays an important role in the mechanism of particle motion for particle with smaller S and G. For G=0.01 the image force is the dominant force on particle deposition. For S=G=0.1 the ratio Q/G is critical in terms of longest deposition distance.

According to the definition of parameters S, Q and G, referred to section 5.3.1, a smaller S can either mean smaller inertia force or larger viscous force and so forth. Therefore, the effect from the flow field in terms of viscous force has been covered in the

previous discussion already. The next section concentrates on particle deposition distance in different divergent channels.

5.3.5 Effects of Divergent Angles

As mentioned in section 5.2, the effect of a divergent channel on the mechanism of particle motion can be obtained by comparing particle deposition in a divergent channel with that in a parallel-plate channel. In addition, by comparing particle deposition in divergent channels with different divergent angles and different geometry, a better understanding of the mechanism of particle motion can be obtained. The difference between parallel-plate channels and divergent channels on particle deposition are flow field, image force and channel width in the downstream direction.

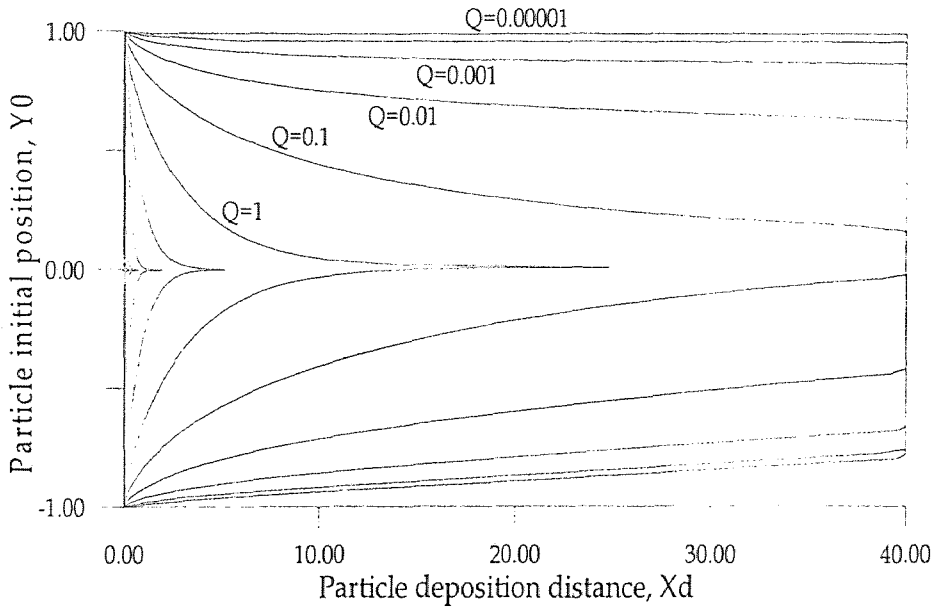

(a)

Figure 5.13 Deposition distance curves in a parallel-plate channel

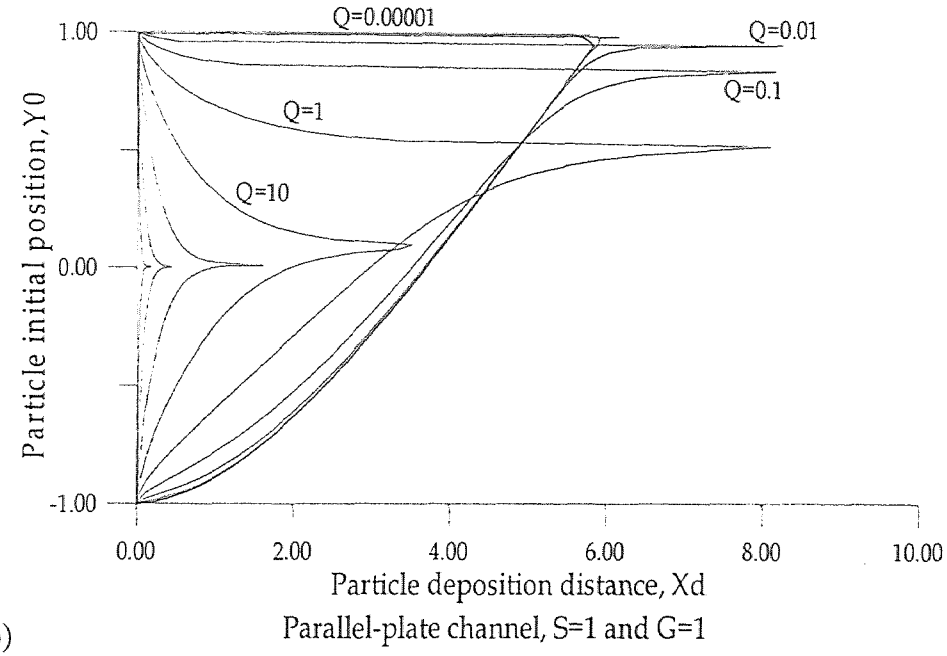

(b) Parallel-plate channel, S=1 and G=1

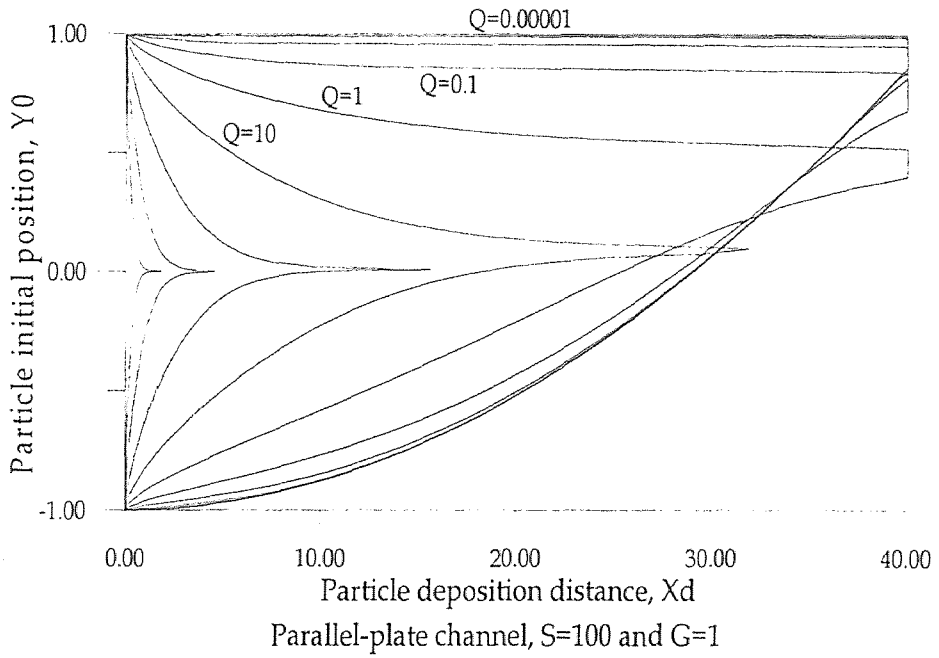

(c) Parallel-plate channel, S=100 and G=1

Figure 5.13 (*continue*) Deposition distance curves in a parallel-plate channel

Figure 5.13(a) through 5.13(c) show deposition distance curves in a parallel-plate channel with different combinations of parameters. Observing figure 5.13(a) and 5.6(a) which have the same value of S=1 and G=0.01 they are both symmetric with respect to the

centerline of the channel but one difference is found. For Q=1 the deposition distance in a parallel-plate channel is much shorter than that in a divergent channel. This is understood to be the contribution of a stronger image force in a parallel-plate channel. From figure 5.13(b) and figure 5.8(c) which have the same value of S=1 and G=1, it is noted that the longest deposition distance in a parallel-plate channel is not the curve with Q/G=1 but Q/G=0.01. This is understood as the result of a stronger image force in a parallel-plate channel. From figure 5.13(c) and figure 5.8(e) the difference is much more pronounced that under the same condition of S=100 and G=1 deposition distance in a parallel-plate channel with $Q \leq 1$ are very different from that in a divergent channel. In figure 5.8(e) all curves are symmetric while in figure 5.13(c) only curves with $Q \geq 10$ are symmetric and curves with $Q \leq 1$ are asymmetric. In conclusion, under same conditions particle deposition in a parallel-plate channel is better than that in a divergent channel and the main factor is the image force.

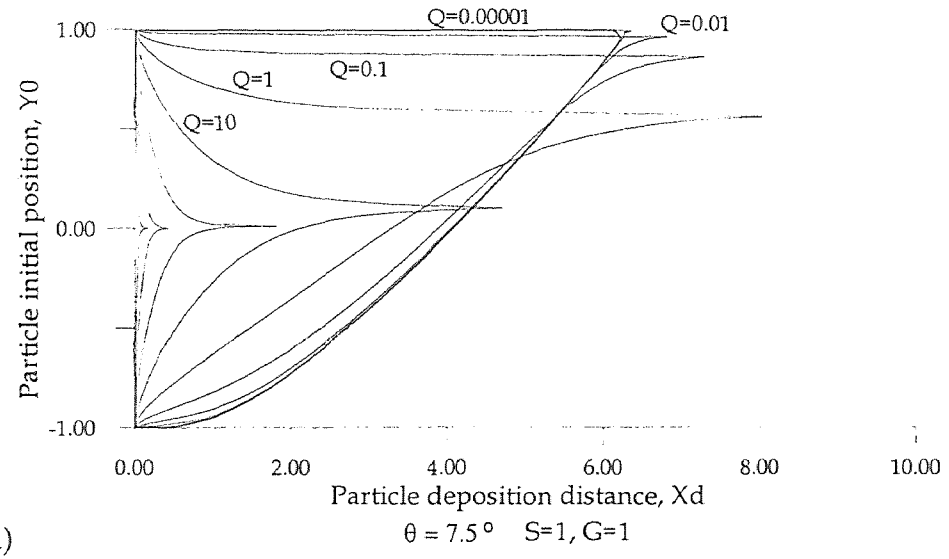

(a)

Figure 5.14 Deposition distance curves in divergent channels with different angles

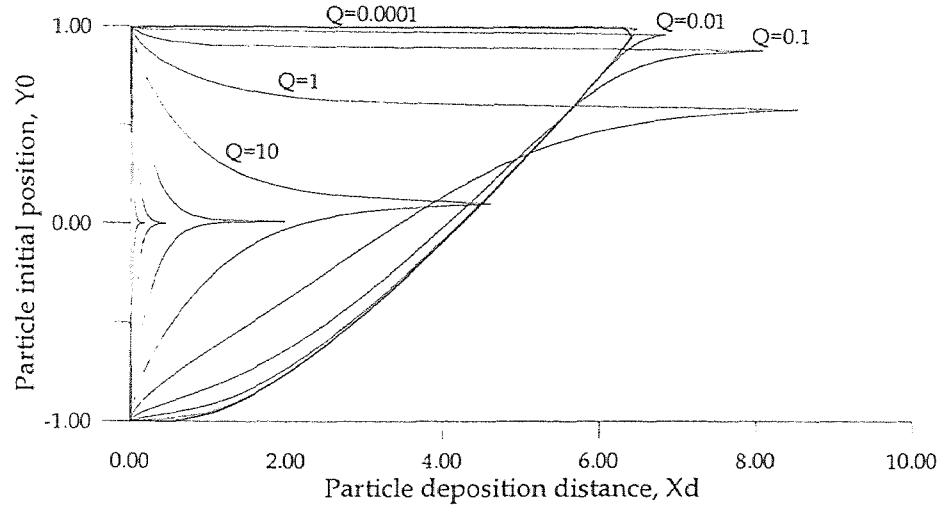

(b)

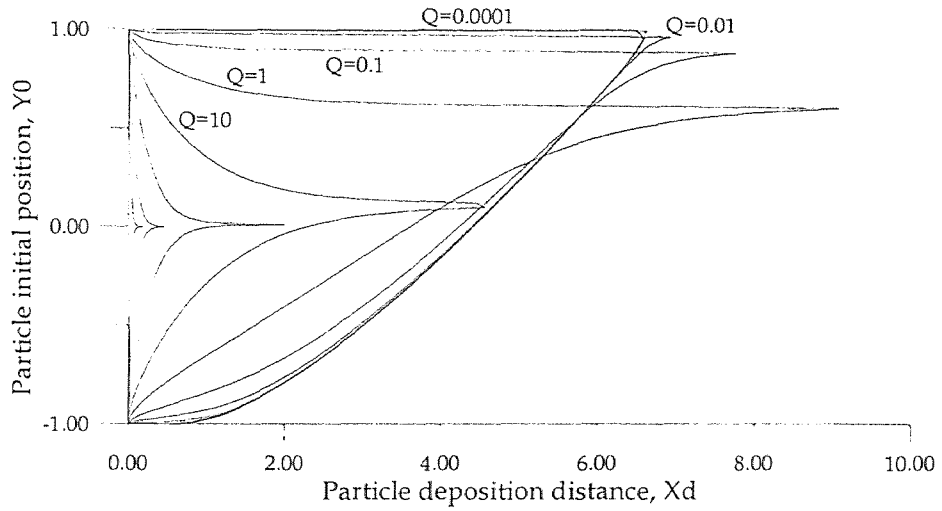

(c)

Figure 5.14 (*continue*) Deposition distance curves in divergent channels with different angles

Figure 5.14(a) through 5.14(c) show deposition distance curves with S=1 and G=1 in divergent channels of different angles. It is noted that the larger divergent angle have the longer deposition distance for curves with $Q \leq 1$. For example, the longest deposition distance for Q=1 is 8.1, 8.55 and 9.1 for θ=7.5°, 10° and 12.5° respectively and the longest deposition distance for Q=0.1 is 7.3, 8.1 and 7.8 for θ=7.5°, 10° and 12.5° respectively. This

is understood that the larger divergent angle results in wider channel width at the same axial distance and weaker image force. Considering particle in a turbulent flow with high initial momentum entering a divergent channel, although the flow velocity in a divergent channel with larger divergent angle is smaller than that with a smaller divergent angle, the reversed flow region must be considered to be subtracted from the total channel area. As dicussed in section 5.2, a divergent channel with $\theta=10^{\circ}$ has the smallest core flow region in these three cases such that for $Q \leq 1$, the longest deposition distance in it is more than that in other divergent channels. However, a larger divgergent angle increases the image force in the axial direction (backward). Therefore a divergent channel with a larger divergent angle is in favor with greater image force. For example, in figure 5.14 the longest deposition distance for Q=10 is 4.7, 4.6 and 4.55 for $\theta=7.5^{\circ}$, 10° and 12.5° respectively.

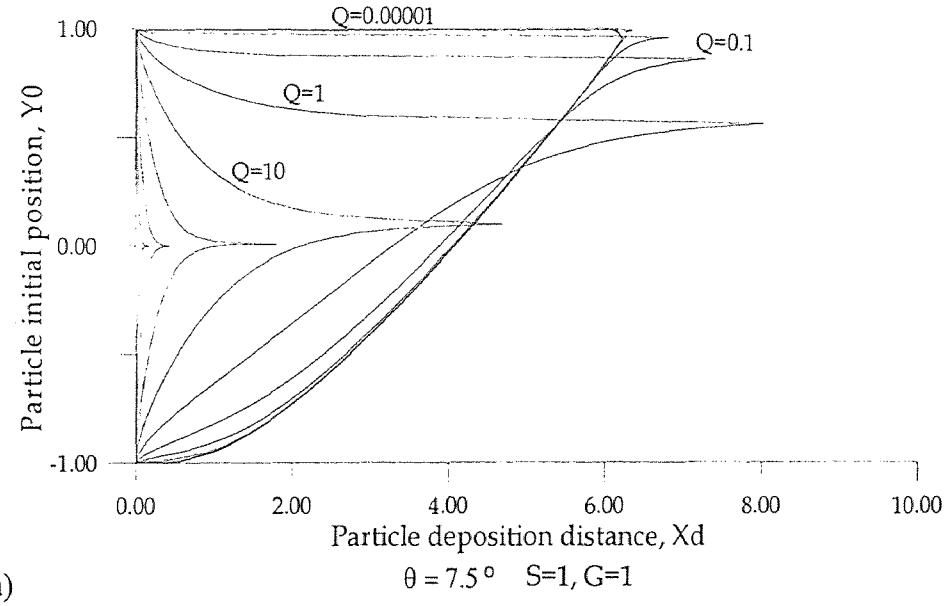

Figure 5.15 Deposition distance curves in a second type of divergent channel (with parallel section)

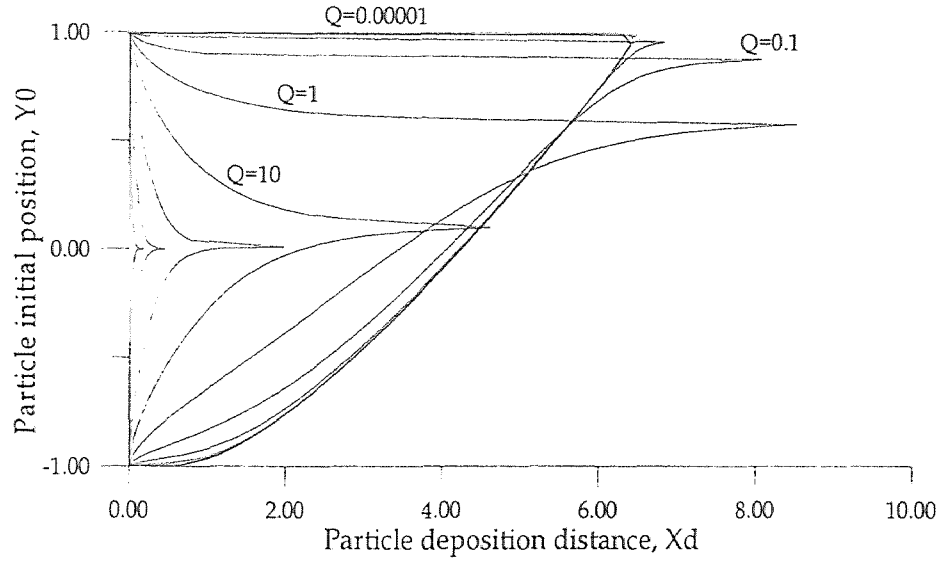

(b)

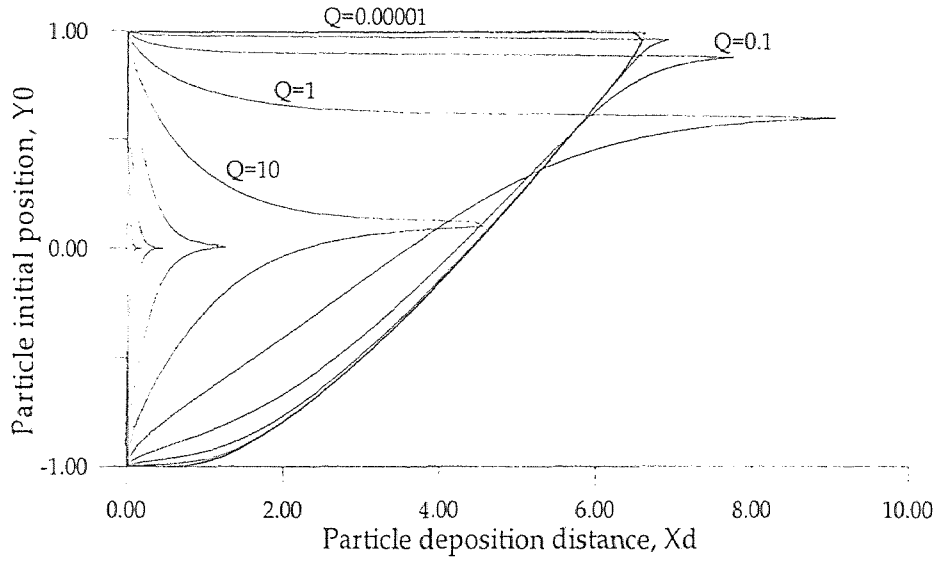

(c)

Figure 5.15 (*continue*) Deposition distance curves in a second type of divergent channel (with parallel section)

Figure 5.15 shows deposition distance in a second type divergent channel with S=G=1 and variable divergent angles. From figure 5.14 and 5.15, the difference made by the different channel configuration is very small. Considering the longest deposition as the index that table 5.1 shows the difference in two types of divergent channel under different

conditions. It is concluded that the difference made by different channel configuration is negligible.

Table 5.1 Longest deposition distance in two types of divergent channel

Q	0.1			1		
θ	7.5°	10°	12.5°	7.5°	10°	12.5°
First type	7.3h	8.1h	7.8h	8.1h	8.55h	9.1h
Second type	7.25h	8.1h	7.8h	8.05h	8.55h	9.1h

In conclusion, the electrostatic image force and divergent angle are the main factors on particle deposition in a divergent channel. Analysis of particle deposition distance curves only gives part of the understanding on the mechanism of particle motion. A proper conclusion is drawn after the discussion of deposition fraction in the next section.

5.4 Fraction of Deposition

The deposition distances presented in previous section 5.3 were obtained by solving the governing equations numerically. From these deposition distance plots one was able to compare the effects of each parameter on the particle motion and on the rate of deposition in different channels. However the exact amount of fraction of deposition can not be read from these deposition distance curves.

As discussed in chapter 4, the fraction of particle deposition is defined as the ratio of total number of particles deposited on the channels walls at an axial distance to the total number of particles entering the channel. The fraction of deposition is defined as follows:

$$\left[\begin{array}{l}\text{Fraction of deposition at}\\ \text{given axial distance X}\end{array}\right] = \frac{\left[\begin{array}{l}\text{total number of particles deposited on}\\ \text{the wall from inlet to X}\end{array}\right]}{\left[\begin{array}{l}\text{total number of particles entering}\\ \text{the channel at inlet}\end{array}\right]} \qquad (4.20)$$

The fraction of deposition is, therefore, equal to zero at the inlet of channel and increases to unity at an axial location where all particles entering the channel are completely deposited.

One can compute the fraction of deposition from each deposition distance curve. For example from figure 5.6(b) to find the fraction of deposition for S=0.1 and G=1 in a divergent channel with $\theta=7.5^{\circ}$ at Xd=1 and Q=1 one can draw a vertical line through Xd=1. The line intersects with curve of Q=1 at $Y0_1$= -0.21 and $Y0_2$=0.57. The fraction of deposition is then equal to

$$1-\frac{Y0_2-Y0_1}{2}=1-\frac{0.57-(-0.21)}{2}=0.61$$

This is explained in the following.

Particles entering the channel at $Y0_1 < Y0 < Y0_2$ are still suspended in the fluid and will penetrate through the channel section at Xd=1. Particles entering the channel at $-1 \le Y0 \le Y0_1$ and $1 \ge Y0 \ge Y0_2$ will deposit on the lower and upper wall respectively since particles entering the channel in these range of $Y0$ have deposition distance less than 1. The incoming particles are assumed to be uniformly distributed along the inlet plane at constant velocity of U_o=1 (dimensionless). Therefore the number of particles penetrated is $Co(Y0_2-Y0_1)$ and the number of particles entering the channel is Co[1-(-1)]=2 where Co is the particle number density. Thus

$$\text{Fraction of deposition} = \frac{2Co - Co(Y0_2 - Y0_1)}{2Co} = 1 - \frac{Y0_2 - Y0_1}{2}$$

Two type of channel configurations are considered in this work. Referring to section 5.2, the first type of divergent channel has a length (from inlet to outlet) of $40h$ and the second type of divergent channel has a parallel-plate section of $10h$ connected to the outlet plane of the first type of channel. The fraction of deposition for both types of channel are computed from Xd=0 to Xd=40. Both types of channel are exhausted into a large reservoir.

It should be pointed out that the fraction of deposition includes particles deposited on the top wall and that on the bottom wall of the channel. Unlike in figures on deposition distances where one can discern on which (top or bottom) wall these particles are deposited , figures on the fraction of deposition do not separate the top wall from the bottom. Therefore a skewed curve and a symmetric curve in two different deposition distance figures may produce the same amount of fraction of deposition.

In order to see how the dimensionless parameters, S, G and Q, are affected by physical properties including particle density ρ_p, particle diameter d_p, inlet velocity Uo, half channel width h, and dynamic viscosity of the fluid μ, we may express these parameters as being proportional to the above physical properties as follows. The inertia parameter S is proportional to $(\rho_p d_p^2 Uo) / (\mu h)$. The charge parameter Q is proportional to $q^2 / (\mu d_p h^2 Uo)$ or $d_p^3 / (\mu h^2 Uo)$ if q is assumed to be proportional to the surface area of the spherical particle. The gravity parameter G is proportional to $(\rho_p d_p^2 g) / (\mu Uo)$.

The effects of each dimensionless parameter and each physical property on the fraction of deposition are discussed in the following sections.

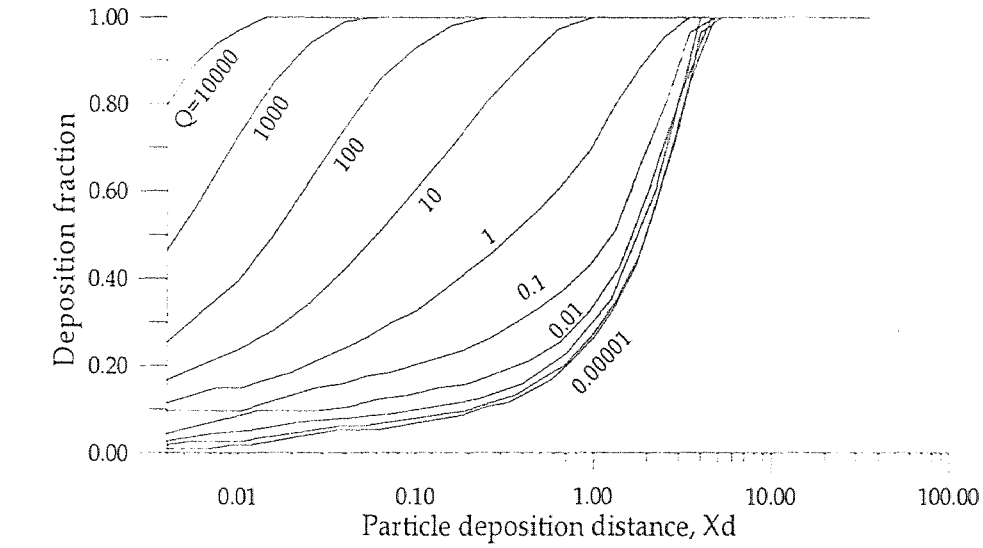

(a)

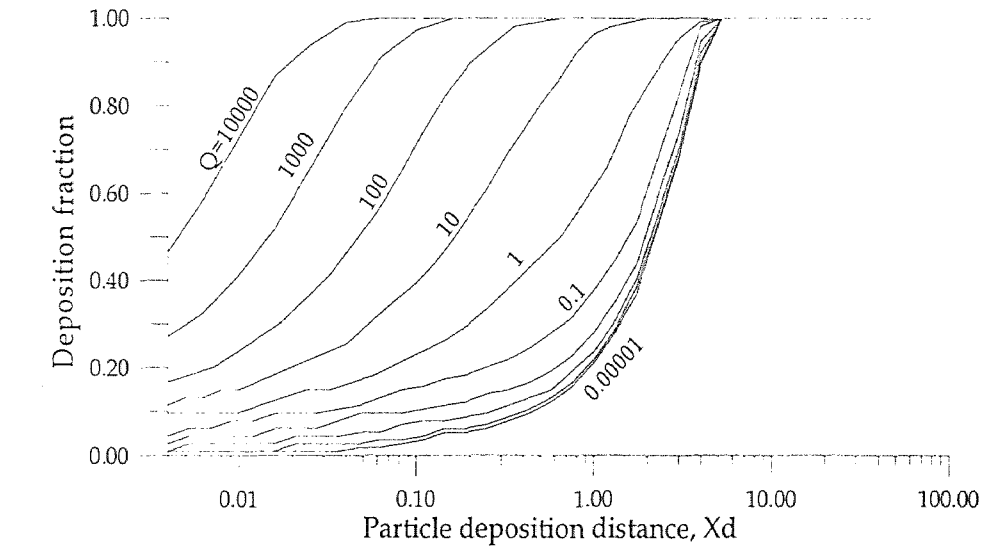

(b)

Figure 5.16 Fraction of deposition for G=1 and variable S and Q

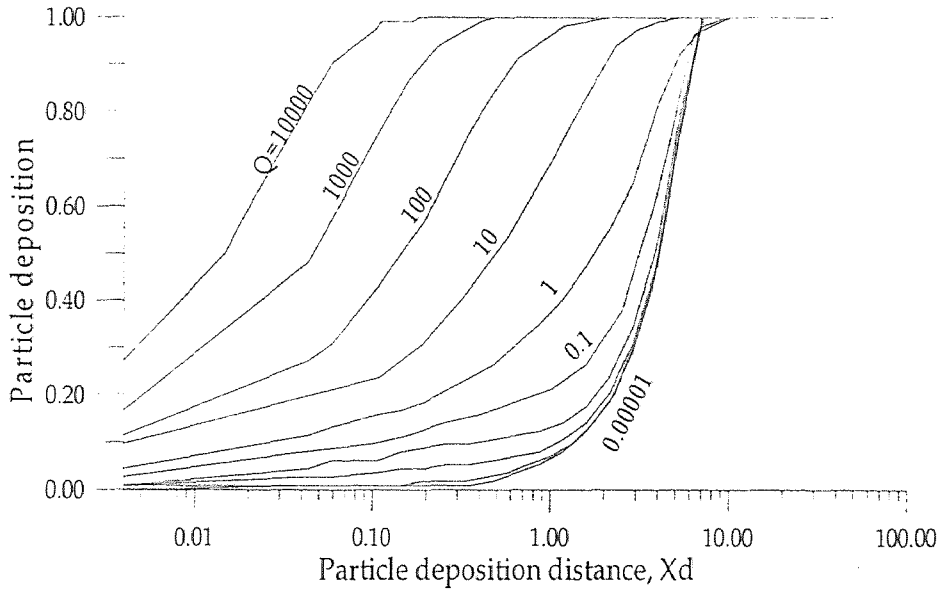

(c) θ = 7.5° S=1, G=1

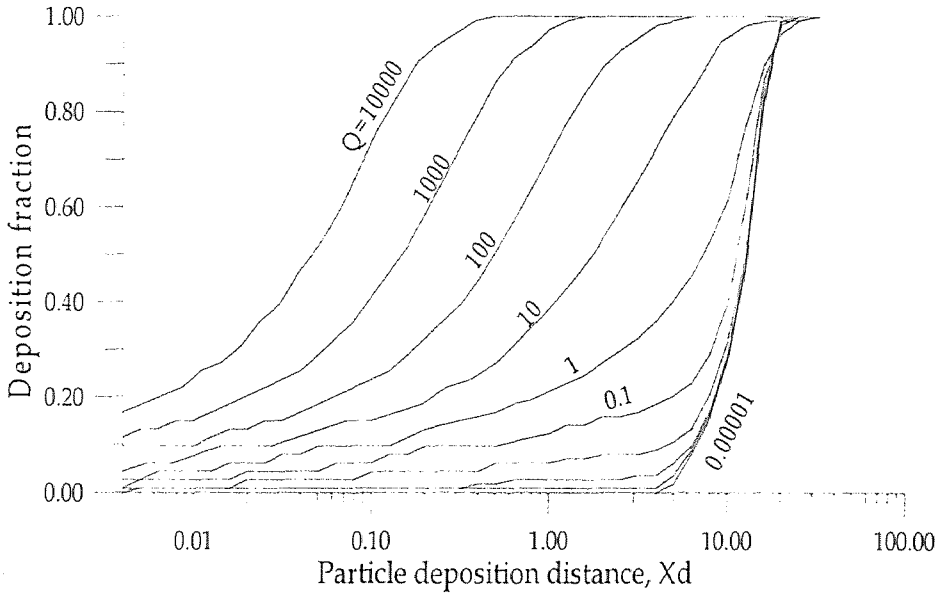

(d) θ = 7.5° S=10, G=1

Figure 5.16 (*continue*) Fraction of deposition for G=1 and variable S and Q

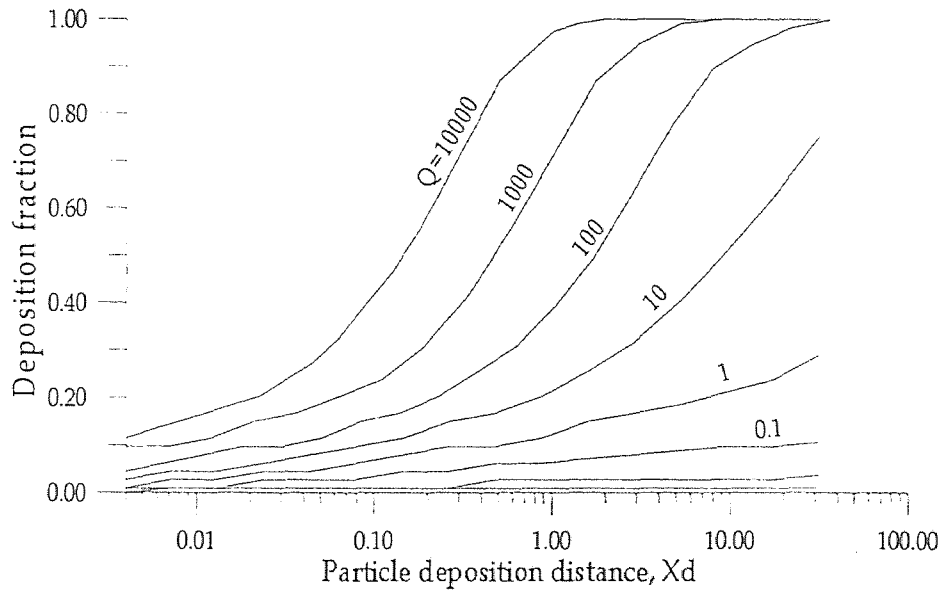

(e)

Figure 5.16 (*continue*) Fraction of deposition for G=1 and variable S and Q

5.4.1 Effects of S on Deposition

As the inertia parameter S is increased while G and Q are maintained constant, the deposition is decreased. This can be seen from figures 5.16 (a) through 5.16(e) in which the fraction of deposition in a 7.5° divergent channel at G=1 and $10000 < Q < 0.00001$ for S = 0.01, 0.1, 1, 10 and 100 are presented respectively. For example for Q=1 and G=1 the deposition at Xd=1 is 0.71, 0.61, 0.365, 0.21 and 0.11 for S=0.01, 0.1, 1, 10 and 100 respectively. Moerover, figure 5.16(e) and 5.17 have the same ratio of S/G=100 and the deposition curves look alike in these two figures. It can be seen that curves with $Q/S \leq 0.1$ have less deposition but the deposition in figure 5.16(e) with S=100 and G=1 is better than that in figure 5.17 with S=1 and G=0.01 under the same ration of Q/S. For example, the deposition at X=10 is 0.21, 0.52, 0.92 and 1.0 for Q/S=0.01, 0.1, 1 and 10 in figure 5.16(e) respectively and the deposition at X=10 is 0.2, 0.44, 0.85 and 0.985 for Q/S=0.01, 0.1, 1

and 10 in figure 5.17 respectively. The effects of S on particle deposition is understood better with the gravity effect G and charge effect Q that is discussed in the next two sections.

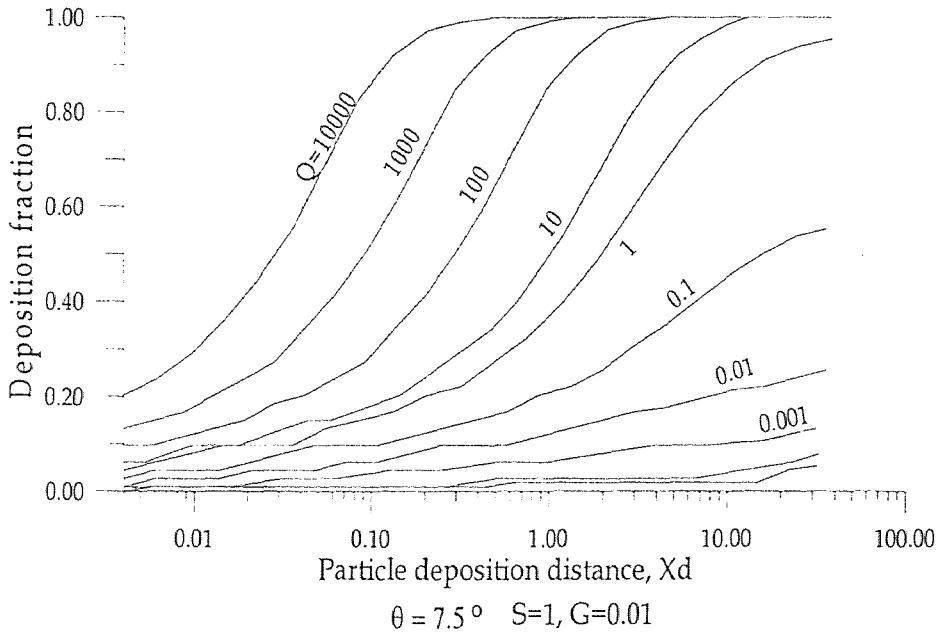

Figure 5.17 Fraction of deposition for S=1, G=0.01 and variable Q

5.4.2 Effects of Q on Deposition

The charge parameter Q increases deposition and its effects on deposition is pronounced when S and G are small. This can be seen from figures 5.18 (a), (b) and (c) in which the deposition in a 7.5° divergent channel with Q ranged from 10000 to 0.00001 are presented for S=G=0.1, 10 and 100 respectively. The following table is a comparison of the deposition at Xd=1 for different values of Q at several sets of S=G.

Table 5.2 Comparison of Deposition in a 7.5° Divergent Channel at S=G =0.1, 1 and 10.

Figure	S=G	Q=0.001	0.01	0.1	1	10	100	1000
5.18(a)	0.1	0.11	0.185	0.31	0.585	0.92	1	1
5.17(c)	1		0.13	0.21	0.365	0.68	0.96	1
5.18(b)	10			0.13	0.22	0.395	0.7	0.97

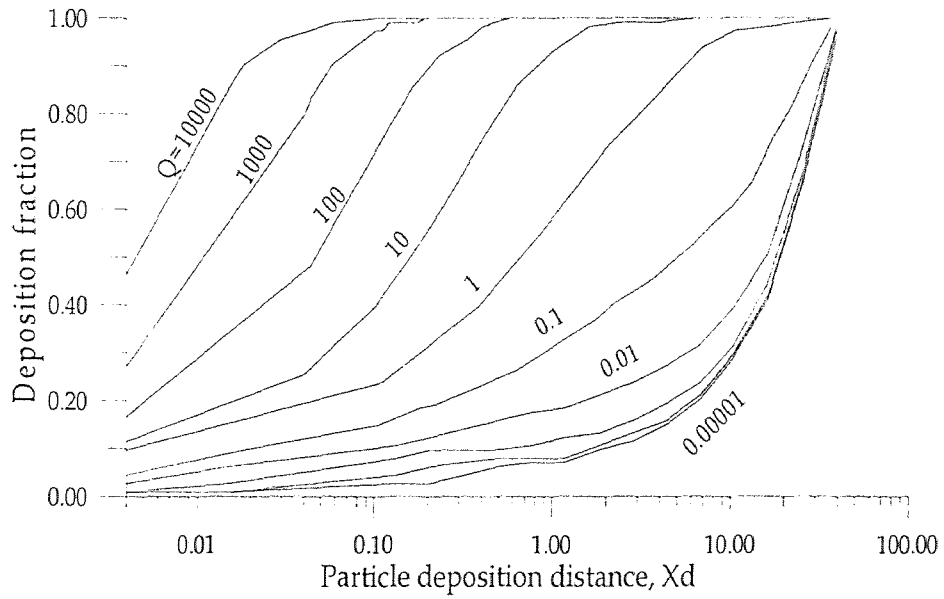

(a)

Figure 5.18 Fraction of deposition for S/G=1

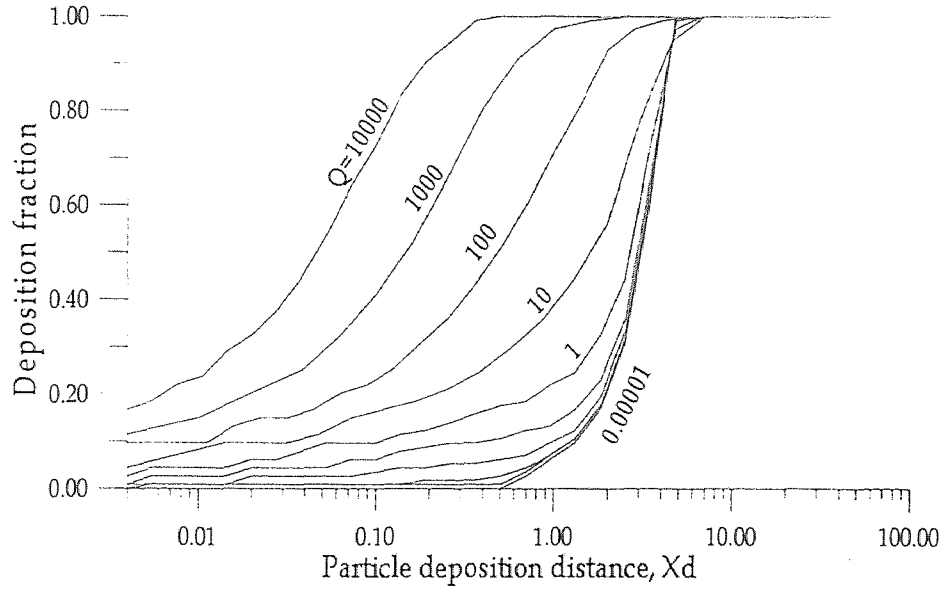

(b) θ = 7.5° S=10, G=10

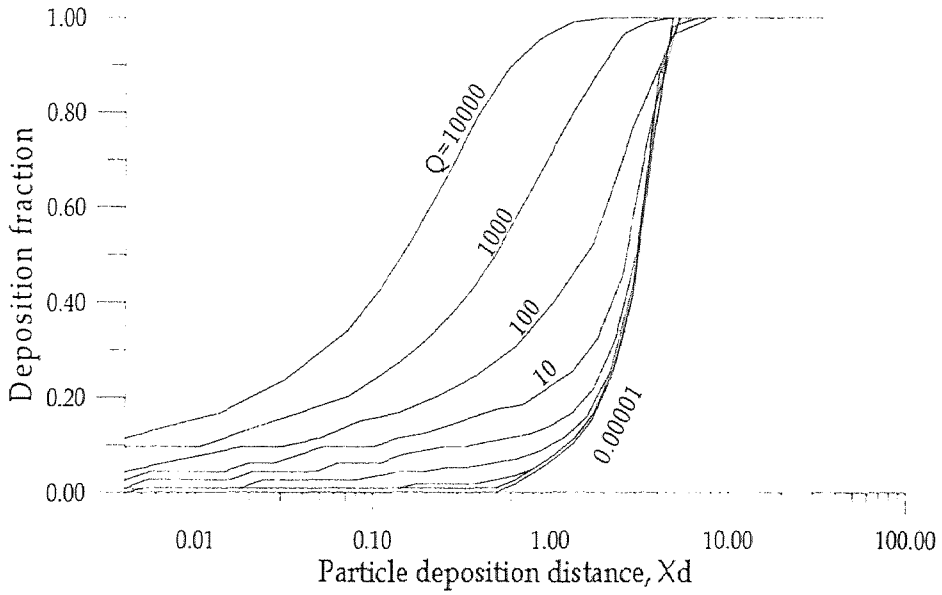

(c) θ = 7.5° S=100, G=100

Figure 5.18 (*continue*) Fraction of deposition for S/G=1

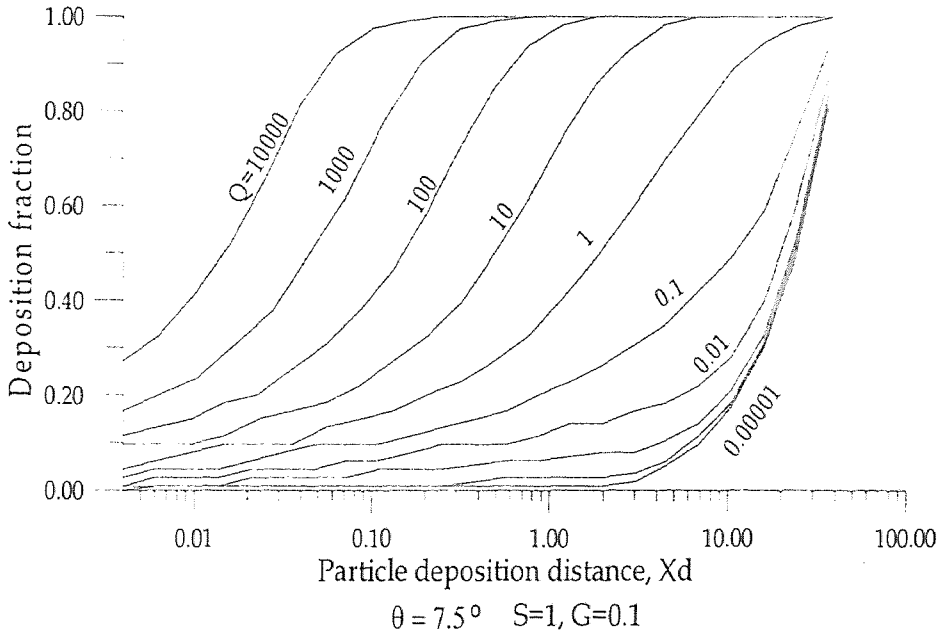

Figure 5.19 Fraction of deposition for S=1 and G=0.1

Figure 5.19 depicts the fraction of deposition for S=1 and G=0.1. From figure 5.19 and figure 5.16(c) it can be seen that the deposition curves with $Q \geq 10$ are very alike disregarding the difference of parameter G. This is understood that, as discussed in section 5.3.2, for $Q/G \geq 10$ the gravity force can be neglected. Moreover, from figure 5.18(b) and 5.18(c) it is interesting to note that the deposition curves with small Q, i.e. $Q \leq 0.1$, are very much alike beyond Xd=2 for different S and G. This is understood that for $Q/G < 0.01$ the electrostatic charge force can be neglected after axial distance longer than $2h$ and, referring to section 5.3.2 and 5.3.4, the particle deposition distributed along the lower channel wall. It need to be mentioned that small Q does make a difference in deposition near the channel entrance. For example, from figure 5.18(c) at Xd=0.5 the deposition with Q=0.1 is about twice of deposition with Q=0.01.

5.4.3 Effects of G on Deposition

The introduction of the gravity parameter G into the flow results in more particles deposited on the bottom wall and make the deposition distance curve skewed. However the changes in the fraction of deposition are gradually increasing and are not as dramatic as the production of skewed deposition distance curves. As shown in figure 5.16 and figure 5.17 all particles are deposited in the channel if $G \geq 1$. Due to the equilibrium condition between the charge force and gravity force a complete deposition may occur earlier at Q=0 than those cases for which Q is > 0. For example in figure 5.16(c) the curves for Q=100 and Q=0.00001 intersect at 0.97 deposition and Q=0.00001 is completely deposited at Xd=6.8 while Q=100 is completely deposited at Xd=9.9.

In most cases, increases in G produce higher deposition but there are some exceptions. For example for flow in a 7.5° divergent channel at S=1 and Q=1 the deposition at Xd=1 is 0.385, 0.39, 0.365, and 0.63 for G=0.01, 0.1, 1 and 10 respectively. It is seen that there is a small dip in deposition at G=Q=1. This is due to the effects of balance of upward charge force and downward gravity force in the upper half of the channel.

5.4.4 Effects of the Particle Diameter d_p on Deposition

When the particle diameter is increased by 10 times, both S and G increase 100 times. However Q will be reduced by a factor of 10 if q remains constant. From figure 5.18(a) and figure 5.18(b) we can find that if S=G=0.1 and Q=10, the deposition at X=1 is 0.92. If we increase d_p by 10 times then S=G=10 and Q=1 and the deposition at X=1 is only 0.24 which means the deposition decreases as d_p is increased in this case. Figure 5.19 also indicates that when S=G=1 is changed to S=G=100 then Q/S will change from Q/S=10/1=10 to

Q/S=Q/S=1/100=0.01 and the deposition decreases. The decrease will be smaller as Q becomes smaller and eventually the deposition will increase when Q=0. The deposition at Q=0 for uniform velocity in a parallel-plate channel can be found by solving the governing equation and the solution is:

Fraction of Deposition = [G X - S G + S G Exp(-X/S)]/2. for U=1 and θ=Q=0. This equation shows that for S=G=0.1 the deposition at X=1 is 0.045 and that for S=G=10 is 0.242. Therefore when the deposition mechanism is dominated by the charge effect and increase in diameter without increase in charge will reduce the deposition.

Next we assume that the charge is to be proportional to the surface area of the spherical particle. Then at S=G=0.1 and Q=10, the deposition at X=1 is 0.92 while at S=G=10 and Q=10000 (since Q is proportional to d_p^3) the deposition increases to 1.

5.4.5 Effects of Uo, h, μ, ρ_p and q on Deposition

Since S and G are proportional to Uo and Q is inversely proportional to Uo if we increase the fluid velocity Uo then S and G increase and Q is reduced. In this situation the deposition decreases. Therefore increases in Uo decrease deposition.

It can also seen from the definition of S, G and Q parameters that increase in the channel width h and/or dynamic viscosity μ will reduce the deposition. Increasing the particle density ρ_p will increase S and G at the same time. Figure 5.18 shows that at high Q increasing ρ_p will decrease the deposition but at low Q increase in ρ_p will increase the deposition due to gravitational sedimentation. The charge effects is very clear. It will increase the deposition as q is increased.

5.4.6 Effects of Divergent Channel on Deposition

The discussion in this section is continued from section 5.3.5 to give a better understanding of mechanism of particle motion in different channel flow field. First the fraction of deposition in a divergent channel with $\theta=7.5^{\circ}$ is compared with that in a parallel-plate channel. Second the effect of different divergent angles on particle deposition in a divergent channel is presented. The third issue is the difference of particle deposition between two type of divergent channel configurations.

Figure 5.20(a) through (c) show the fraction of deposition in a parallel-plate channel with different parameters. Figure 5.17, 5.16(c) and 5.16(e) have the same value of parameters respectively that from these figures one can find the result as shown in table 5.3.

Table 5.3 Deposition at X=1: (=) parallel-plate channel and (<) 7.5° divergent channel

Figure	S	G	0.001	0.01	0.1	Q=1	10	100	1000	10000
5.17 (<)	1	0.01	0.065	0.12	0.21	0.375	0.5			
5.20(a) (=)	1	0.01	0.125	0.155	0.24	0.4	0.725	0.975		
5.16(c) (<)	1	1			0.215	0.385	0.7	0.965	1	
5.20(b) (=)	1	1			0.24	0.4	0.73	0.98	1	
5.16(e) (<)	100	1				0.11	0.22	0.39	0.72	0.98
5.20(c) (=)	100	1				0.16	0.24	0.415	0.74	0.98

Table 5.3 is a comparison of deposition in a parallel-plate channel and that in a 7.5° divergent channel at three sets of S and G for various values of Q. It is easily seen that the deposition is higher in a parallel-plate channel under the same conditions of small Q and G.

When $G \geq 1$ and $Q \geq 10$ the difference of deposition in two channels is very small. This can be seen in figure 5.21.

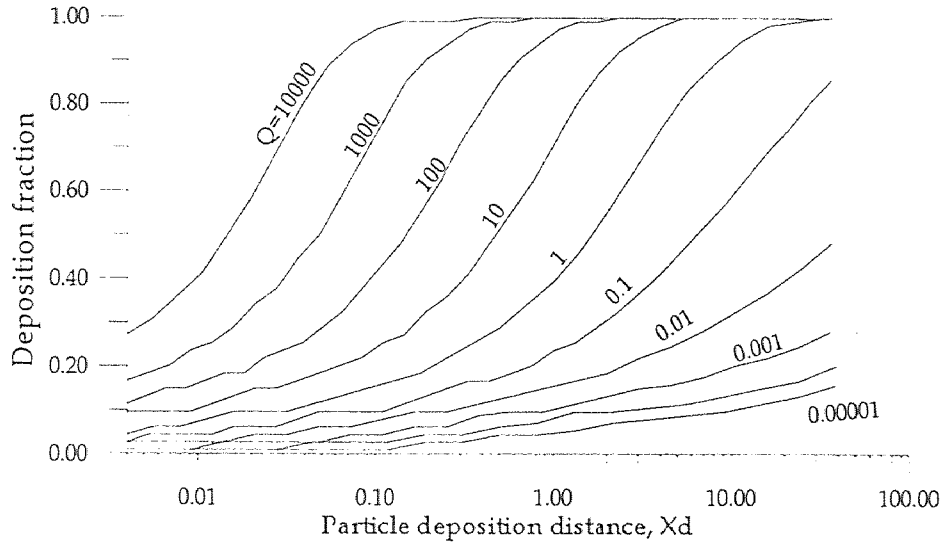

(a) Parallel-plate channel, S=1 and G=0.01

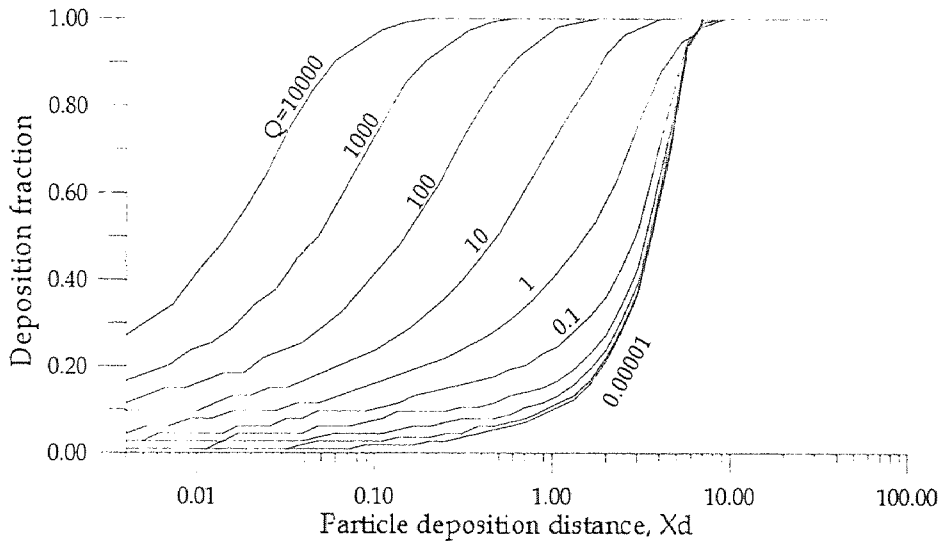

(b) Parallel-plate channel, S=1 and G=1

Figure 5.20 Fraction of deposition in a parallel-plate channel

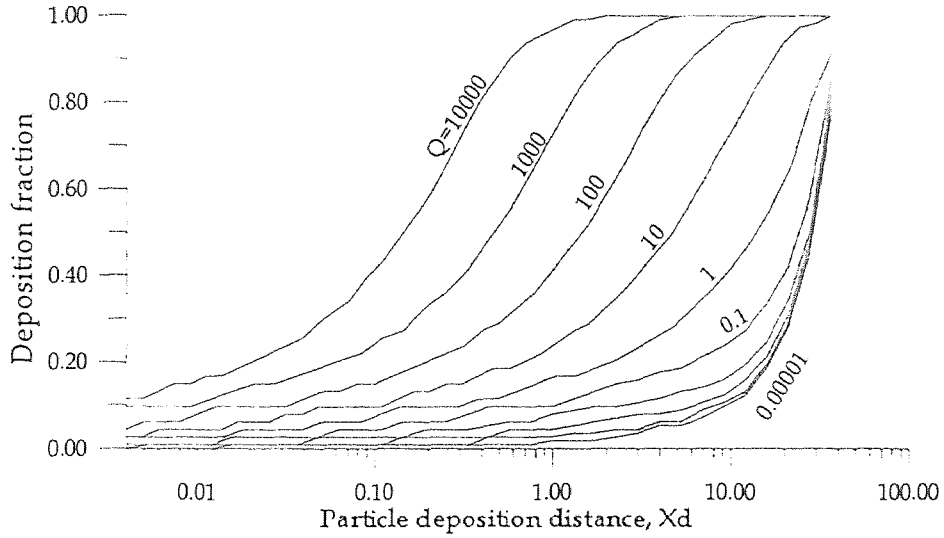

(c) Parallel-plate channel, S=100 and G=1

Figure 5.20 (*continue*) Fraction of deposition in a parallel-plate channel

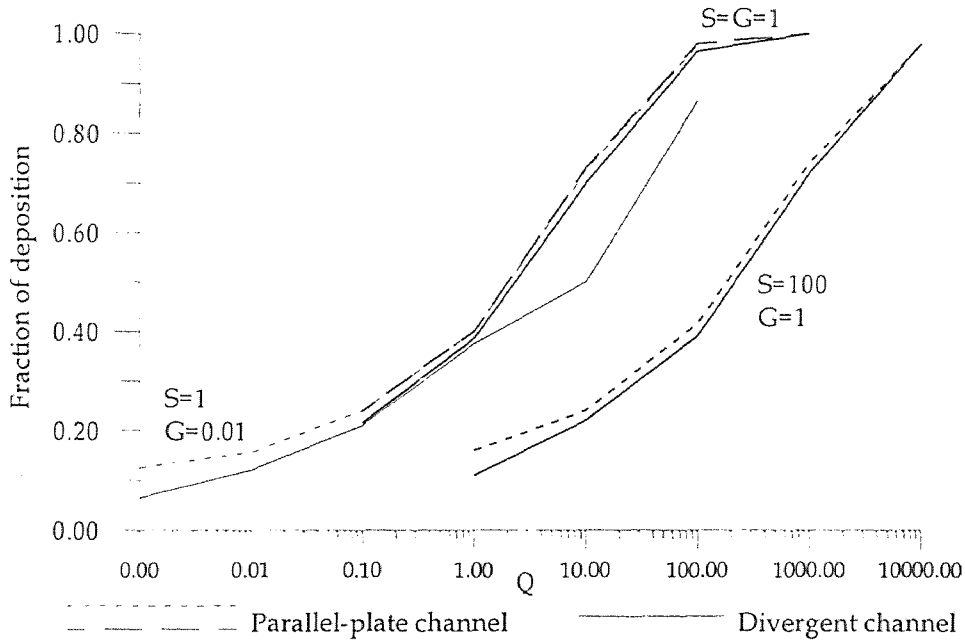

Figure 5.21 Deposition at Xd=1 in a parallal-plate channel and a divergent channel with $\theta=7.5^{\circ}$.

Figure 5.21 depicts the results discussed above by taking Q/G against particle deposition. It can be concluded that particle deposition in a parallel-plate channel is slightly better than that in a divergent channel with the same parameters. The significant difference in figure 5.21 is the curve with S=1 and G=0.01 at Q/G=100 that the deposition in a parallel-plate channel increases substantially, while that occurs in a divergent channel at Q/G=1000. This is due to the advantage of parallel-plate channel with a greater image force at a given Xd. Considering the flow velocity profile, referring to section 5.2, a particle in a parallel-plate channel carries a greater S than in a divergent channel. From figure 5.21 one can take curve with S=G=1 as a divergent case and curve with S=100 and G=1 as a parallel-plate case. At the same Q/G it is clear that deposition in a parallel-plate channel is better than that in a divergent channel. This draws a conclusion that the effectiveness of image forces on particle deposition is greater than that from the flow field.

5.4.7 Effects of Channel Configuration on Deposition

The effects of divergent angle on the deposition is insignificant as can be seen from figures 5.16(c) and figure 5.22(a) and (b) which show the fraction of deposition with S=G=1 and variable Q in a divergent channel with $\theta=7.5^{\circ}$, 10° and 12.5° respectively. As discussed in section 5.3.5, a divergent channel with a larger divergent angle is in favor with the image force. From figure 5.16(c) and figure 5.22(a) and (b) the deposition distance for 50% deposition is 0.028, 0.045, 0.14 and 0.5 for $\theta=7.5^{\circ}$, 0.014, 0.044, 0.14 and 0.53 for $\theta=10^{\circ}$ and 0.013, 0.044, 0.14 and 0.53 for $\theta=12.5^{\circ}$ respectively. Figure 5.23 depicts the result of this comparison that one can find the axial distance for 50% deposition with $Q \geq 1000$

decreases as the divergent angle increases. However the amount of increase in deposition diminishes as Q is decreased.

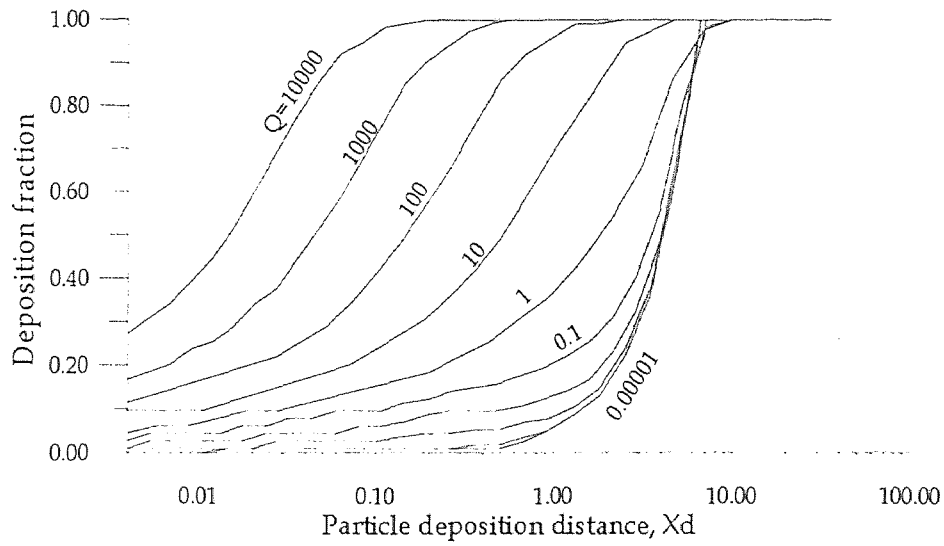

(a)

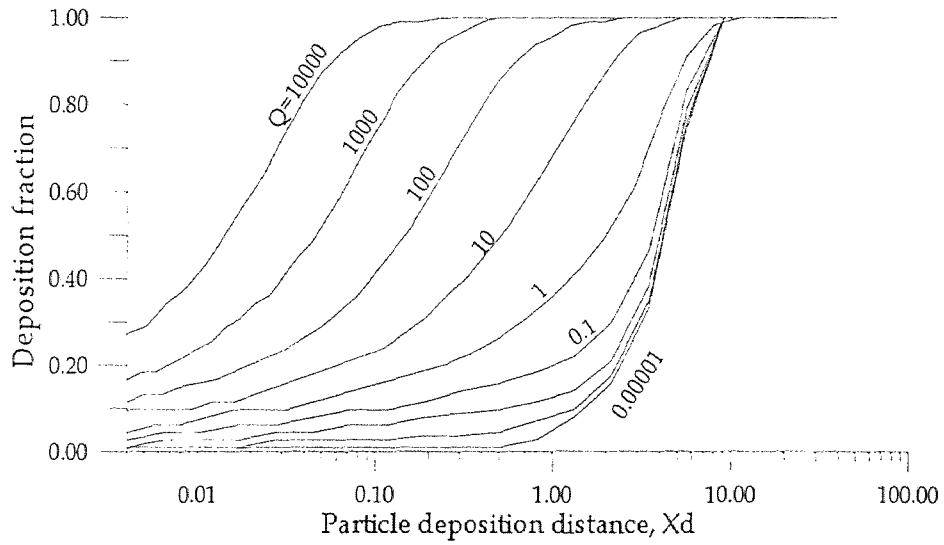

(b)

Figure 5.22 Fraction of deposition in divergent channels with S=1, G=1, θ=10° and 12.5°

Table 5.4 Deposition with S=G=1 at X=1 Vs. different divergent angle

	X=1				X=3		
	Q=0.1	Q=1	Q=10	Q=100	Q=0.1	Q=1	Q=10
$\theta=7.5^{\circ}$	0.21	0.365	0.7	0.965	0.49	0.675	0.97
$\theta=10^{\circ}$	0.205	0.355	0.68	0.96	0.42	0.65	0.96
$\theta=12.5^{\circ}$	0.2	0.355	0.68	0.96	0.41	0.64	0.96

As shown in Table 5.4 the deposition decreases for $Q \leq 10$. Table 5.4 lists depositions in divergent channels at X=1 and X=3 for $0.1 \leq Q \leq 100$.

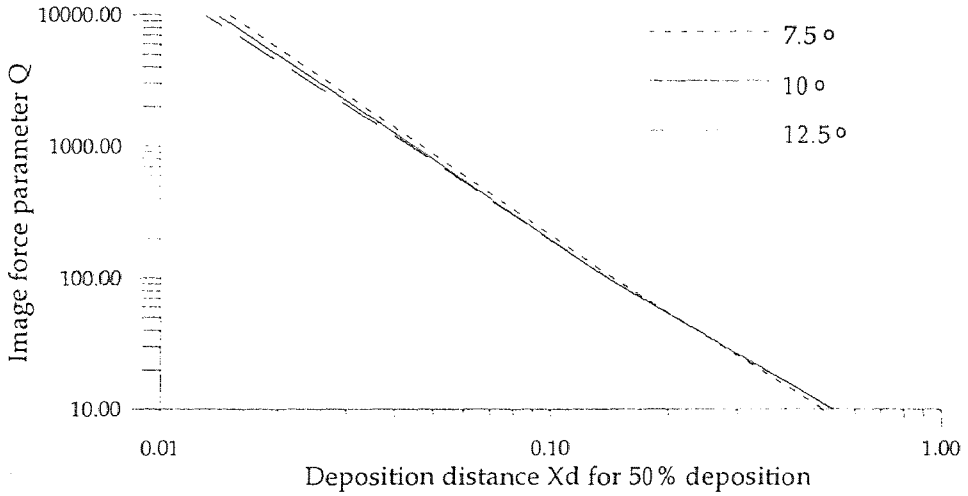

Figure 5.23 Deposition distance for 50% deposition in divergent channels with different divergent angles and Q

Figure 5.24(a) through (c) show the fraction of deposition with S=G=1 and variable Q in the second type of divergent channels for $\theta=7.5^{\circ}$, 10° and 12.5° respectively. It was discussed previously that the divergent channels connected with a parallel-plate section

produce more deposition under the same condition but the difference is insignificant. From figure 5.16(c), figure 5.22 and figure 5.24 the change of deposition at X=1 due to different channel configuration is shown in table 5.5.

Table 5.5 Deposition at X=1 in two types of divergent channel

	First type divergent channel				Second type divergent channel			
	Q=0.1	Q=1	Q=10	Q=100	Q=0.1	Q=1	Q=10	Q=100
θ=7.5°	0.21	0.365	0.7	0.965	0.215	0.39	0.71	0.97
θ=10°	0.205	0.355	0.68	0.96	0.2	0.36	0.695	0.96
θ=12.5°	0.2	0.355	0.68	0.96	0.195	0.38	0.68	0.965

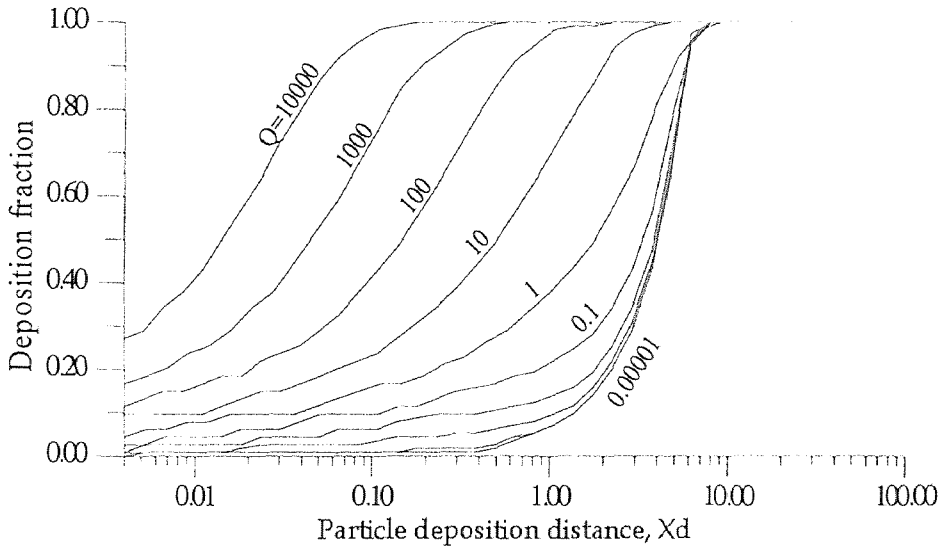

(a)

Figure 5.24 Fraction of deposition in a second type of divergent channel

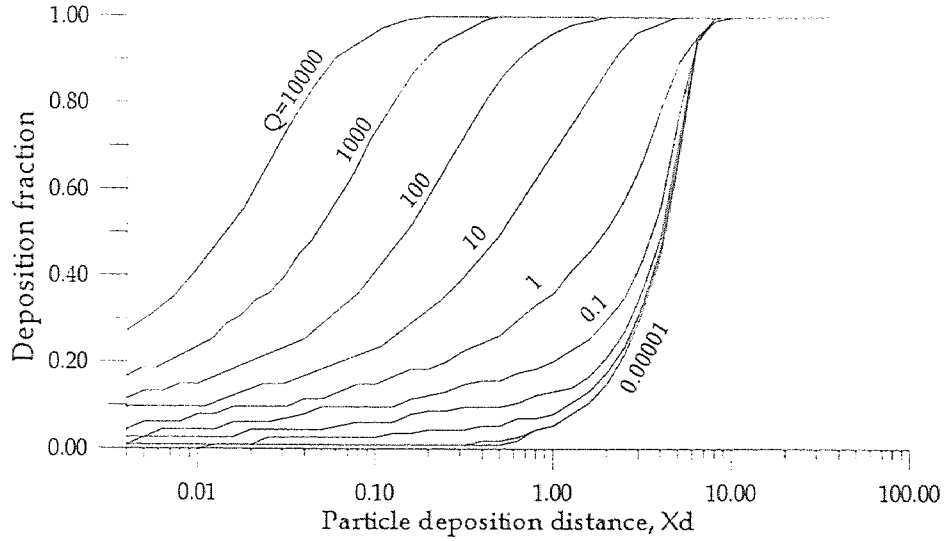

(b) $\theta = 10^{o}$ S=1, G=1

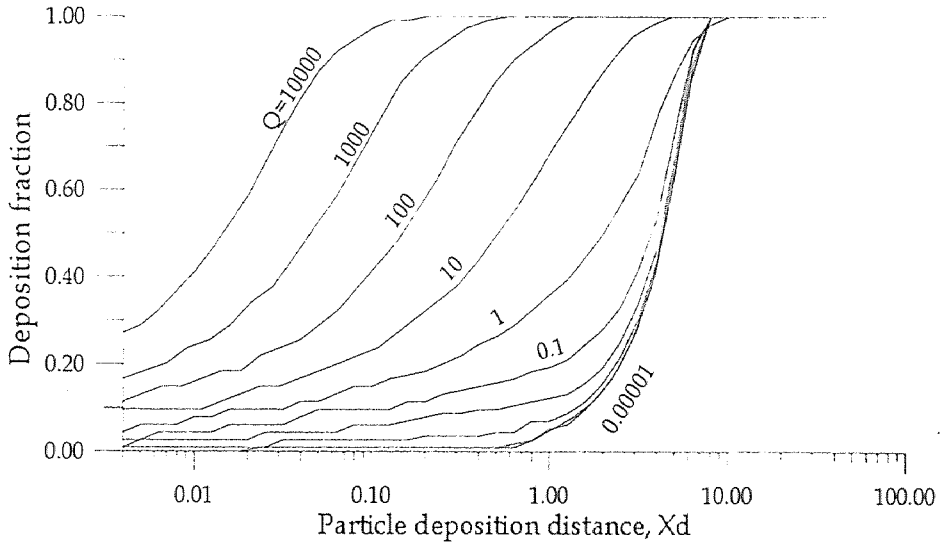

(c) $\theta = 12.5^{o}$ S=1, G=1

Figure 5.24 (*continue*) Fraction of deposition in a second type of divergent channel

CHAPTER 6

CONCLUSION

The summary of above discussion is presented in this section that includes the primary factor of particle motion, the performance of different channels on particle deposition and determinant parameters on particle deposition in a divergent channel.

A numerical simulation model for turbulent channel flow is built by using software *FIDAP* and the result is tested in comparison with experimental measurement. Different turbulent channel flow problems are solved numerically by this model and the results are investigated and the influence from flow fields on particle deposition is distinguished and discussed.

A computational program is developed to solve the motion of particle in a turbulent channel flow and particle deposition is calculated under different conditions. Particle deposition distance and fraction of deposition are studied in detail for the need of better understanding on the mechanisms of particle motion in a turbulent channel flow under the effect of coupled forces which are gravity, electrostatic image, fluid viscous and particle inertia forces. A conclusion is drawn according to these aspects.

The ranges of parameters used in this analysis are

$\theta = 0^{o}, 7.5^{o}, 10^{o}, 12.5^{o}$

S = 0.01, 0.1, 1, 10, 100

G = 0.01, 0.1, 1, , 100

Q = 10000, 1000, 100, 10, 1, 0.1, 0.01, 0.001, 0.0001, 0.00001

$L/h = 40$

$Re = 7500$

As a flow enters a channel with uniform velocity profile, the flow undergoes a developing process in a channel and the velocity profile changes according to the channel geometry. In a parallel-plate channel the production of turbulence is limited and less instability is added into the fluid phase. In a divergent channel, flow undergoes a diffusion process or relaminarization along with the production of turbulence and generation of instability which depend on the divergent angle. Smaller divergent angle forms a slowly changed geometry that is considered as a smaller source of turbulence which generates less instability than that being eliminated by the diffusion effect. Larger divergent angle forms a rapidly changed geometry that is considered as a greater source of turbulence which produces instability faster than that being eliminated by diffusion effect. Therefore a divergent channel with a smaller divergent angle has a small reversed flow area and it can be reduced by changing the channel geometry while a divergent channel with a larger divergent angle has a greater reversed flow area and it can not be reduced by changing channel geometry.

A dilute solid suspension in a turbulent flow field results in a solid phase with high velocity. As this two-phase flow enters a channel the particle motion depends on the forces applied on the particle itself which includes gravity, electrostatic image, viscous, and inertia forces. In a parallel-plate channel a particle depends on constant gravity and image forces and variable viscous forces which are due to the developing flow field in that channel to change its momentum. In a divergent channel, a particle is under a constant

gravity force and a gradually decreased image force as it moves downstream and a variable viscous force. Therefore a particle in a parallel-plate channel experiences an constant acceleration toward earth produced by constant gravity and image forces while a particle in a divergent channel experiences a gradually decreased acceleration toward earth produced by constant gravity and gradually decreased image forces. Hence a particle in a parallel-plate channel has a greater acceleration toward earth and a particle in a divergent channel has a smaller acceleration toward earth.

Furthermore a particle in a parallel-plate channel needs to travel less distance in order to reach the lower wall while a particle in a divergent channel needs to travel a longer distance in order to reach the lower walls. In conclusion, under the same combination of S, G and Q parameters a parallel-plate channel yields a better performance on particle deposition. However a divergent channel accompanied with greater image force, i.e. $Q \geq 1000$ gives a better particle deposition. It is also concluded that the electrostatic image force is a crucial factor on particle deposition in a divergent channel.

Parameters G, S and Q depend on particle size, particle composition, channel width and viscosity of the fluid phase. Thus, G, S and Q are correlated and the ratio of Q/G, S/G and Q/S are determinant factors on the deposition distance and deposition pattern. A larger viscous force reduces the momentum of a particle but also reduces G, S and Q. Smaller viscous forces affect particle momentum slightly but keeps parameters G, S and Q at certain magnitude.

The ratio G/Q is critical in terms of the longest particle deposition distance and deposition pattern. The magnitudes of G and S are associated to each other such that the effect of the inertia force is usually reduced by the gravity force and improves particle

deposition. Parameter Q is a crucial factor for particle deposition in a divergent channel because it can be enhanced artificially to reach Q > 100 that will produce a successful deposition even in an unfavorable condition like S/G ≥ 10. It is certain that for Q/G ≥ 10 and S/G ≥ 10 the gravity force is negligible. For S/G ≥ 10 it needs Q/S ≥ 1 to ensure a complete deposition. As far as the divergent channel is concerned, the image force is the determinant factor in the mechanism of particle deposition.

Different channel configurations only slightly affect the particle deposition in terms of deposition distance and deposition fraction. It can be considered as unnecessary to change the channel configuration. The increase of the divergent angle with a larger image force, i.e. Q ≥ 100, improves the particle deposition because the image force in the negative x-direction increases with increasing divergent angle. Without the sufficient image force the particle deposition decreases with increasing divergent angle. The effectiveness from the flow field with increasing divergent angle to the particle motion is negligible.

The following conclusions are based on this analysis.

(1) As shown below the point of separation, Xs, decreases with increasing divergent angle. The area of reversed flow region increases with increasing divergent angle.

θ	7.5°	10°	12.5°
Xs	10*h*	4*h*	2*h*

(2) Deposition decreases with increasing inertia force.

(3) Deposition increases with increasing gravity force.

(4) Deposition increases with increasing electrostatic image force.

(5) Among parameters S, G and Q, the electrostatic charge parameter Q has the greatest effect on deposition and is followed by the gravity parameter G.

(6) For $Q < 10$, the deposition decreases with increasing divergent angle.

For $Q \geq 100$, the deposition increases with increasing divergent angle due to higher image force in the negative x-direction.

For $100 \geq Q > 10$ the difference made by difference divergent angle is negligible.

(7) For a given condition of S and G, the distance required for a complete deposition in a divergent channel is greatest when $Q=G$.

(8) For $Q/S \geq 10$ and $Q/G \geq 10$, the deposition distance curve is symmetric with respect to the center line of the channel and, therefore, deposited particles are evenly distributed on both channel walls within $x \leq 5h$.

(9) For $Q/G > 10$ and $S/G > 10$ the gravity effect can be neglected.

(10) For $Q/G \leq 0.01$, the electrostatic image force can be neglected.

(11) The difference in deposition in a divergent channel due to different channel configuration (with or without parallel section at the channel exit) is negligible.

(12) The effect of reversed flow on particle deposition is negligible.

The following suggestion is made to be the direction of future research on this subject:

(1) Investigation of different fluid media and particle phase.

(2) Particle trace in conjunction with flow field.

(3) Deposition in a channel with complex geometry configuration.

APPENDIX A

CORRECTION FACTOR FOR IMAGE FORCE IN A DIVERGENT CHANNEL

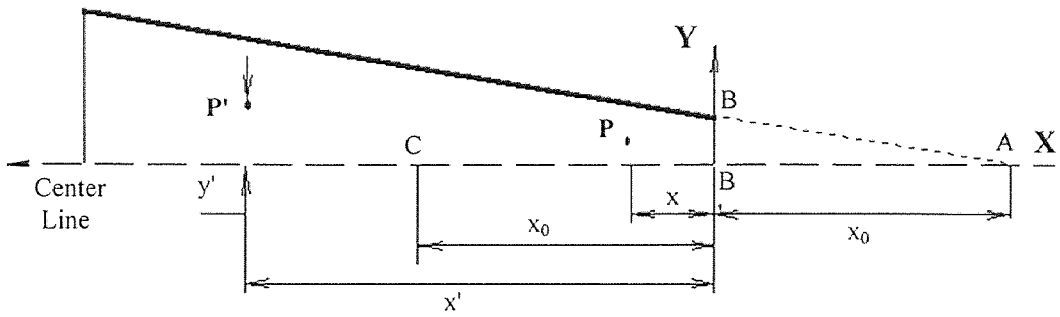

Figure A.1 A point charge in a divergent channel

As shown in figure B channel section AB does not exist. There should be no image force on a point charge at inlet plane BB'. As a point charge moves downstream the induced electrostatic image gradually increases until the point charge travels a certain distance the absence of section AB is negligible. Chiou el al [30] ploted several systems of image pairs that is used to explain this situation.

Figure A.2 is the system of image pairs for two planes intersecting at angle $2\theta=15^{\circ}$. As a point charge moves downstream the induced image points gradually increases. For example, when a point charge just enter the channel the only induced image point is number 1. When it travels at $x=0.2x_0$ the image points are number 1, 2, and 1'. When the point charge travels at $x=x_0$ the image points are number 1, 2, 3, 4, 1', 2' and 3'. Referring to the equations (3.3.6) and (3.3.7), considering a point charge at $x=x_0$ as shown in figure A.2 the image force on that point charge in the x direction are

without AB section: $F_x=5.33531q^2/4\pi\varepsilon_o x_o^2$

with AB section : $F_x=5.40477q^2/4\pi\varepsilon_o x_o^2$

% difference : 1.2852 %

Therefore the image force at $x=x_o$ can be considered as without the absence of section AB.

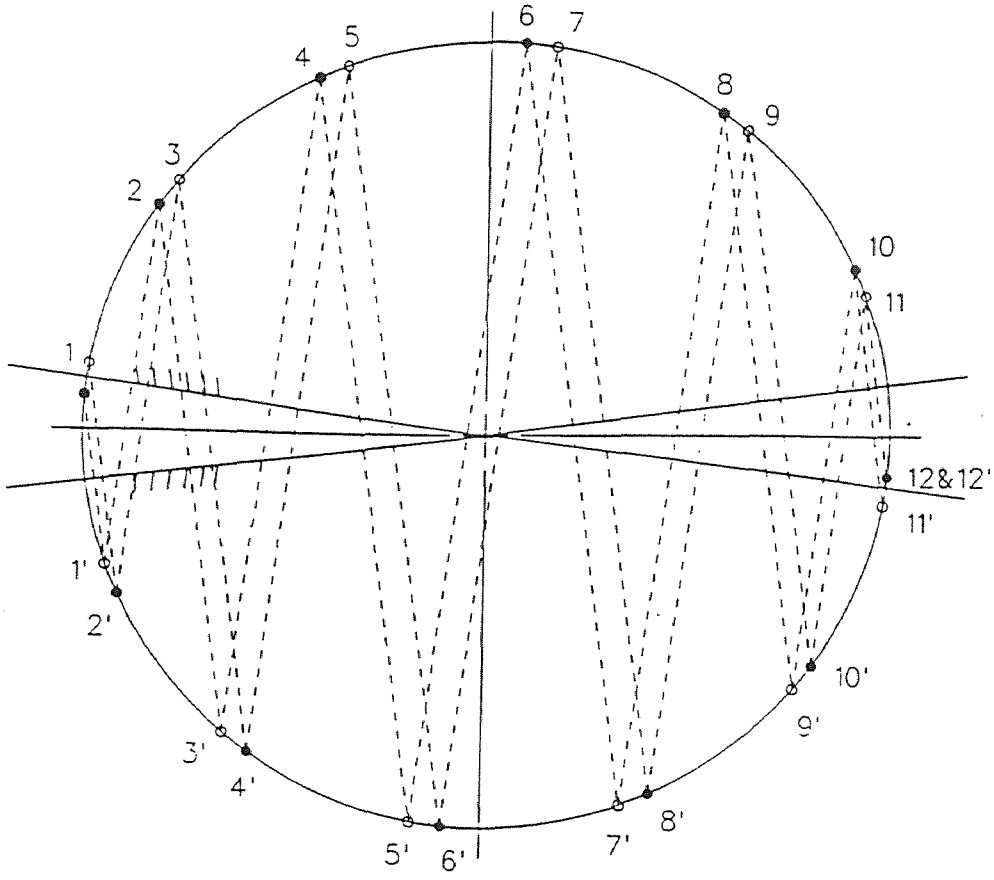

Figure A.2 The system of image pairs for two planes intersecting at angle $2\theta=15^o$

APPENDIX B

SCHEME OF NUMERICAL METHOD IN CFD *FIDAP*

B.1 Successive Substitution

The *successive substitution* method used in the CFD *FIDAP* is an iterative method to solve a large system of linear equations by employing the *successive overrelaxation* algorithm. The *successive overrelaxation* algorithm is developed from the finite-difference techniques for elliptic equations. The introduction of development of this algorithm is described as follows.

Considering a boundary-value problem:

$$\frac{\partial^2 u(x,y)}{\partial x^2} + \frac{\partial^2 u(x,y)}{\partial y^2} + f(x,y)u(x,y) = g(x,y) \qquad \text{(B.1)}$$

with $\quad 0 < x < L$ and $0 < y < K$

where $u(x,y)$ is specified on the boundary by $u(x,y) = h(x,y)$ and $g(x,y)$ are given functions with $f(x,y) \leq 0$. By letting $h = L/M$ and $k = K/N$ for two positive integers M and N and $x_i = ih$ with $0 \leq i \leq M$ and $y_j = jk$ with $0 \leq j \leq N$, and denoting $u(x_i,y_j)$ as u_{ij}, $f(x_i,y_j)$ as f_{ij} and $g(x_i,y_j)$ as g_{ij}, one can use central-difference approximations for u_{xx} and u_{yy} on equation (B.1) and obtains

$$\frac{(u_{i+1,j} - 2u_{ij} + u_{i-1,j})}{h^2} + \frac{(u_{i,j+1} - 2u_{ij} + u_{i,j-1})}{k^2} + f_{ij}u_{ij} - g_{ij}$$

$$= -\frac{h^2}{12}\frac{\partial^4}{\partial x^4}u(x_i + \xi_i h, y_j) - \frac{k^2}{12}\frac{\partial^4}{\partial y^4}u(x_i, y_j + \xi_j k) \qquad \text{(B.2)}$$

with $\quad -1 < \xi_i$ and $\xi_j < 1$.

For simplicity one can assume $h = k$ and an approximation v_{ij} for u_{ij} with the discretization error of order h^2 can be found from the so-called *five-point formula* as shown below.

$$-v_{i-1,j} - v_{i+1,j} + \left(4 - h^2 f_{ij}\right) v_{ij} - v_{i,j-1} - v_{i,j+1} = -h^2 g_{ij} \qquad \text{(B.3)}$$

The coefficients and the relative positions of the points of this approximation are shown schematically in figure B.1.

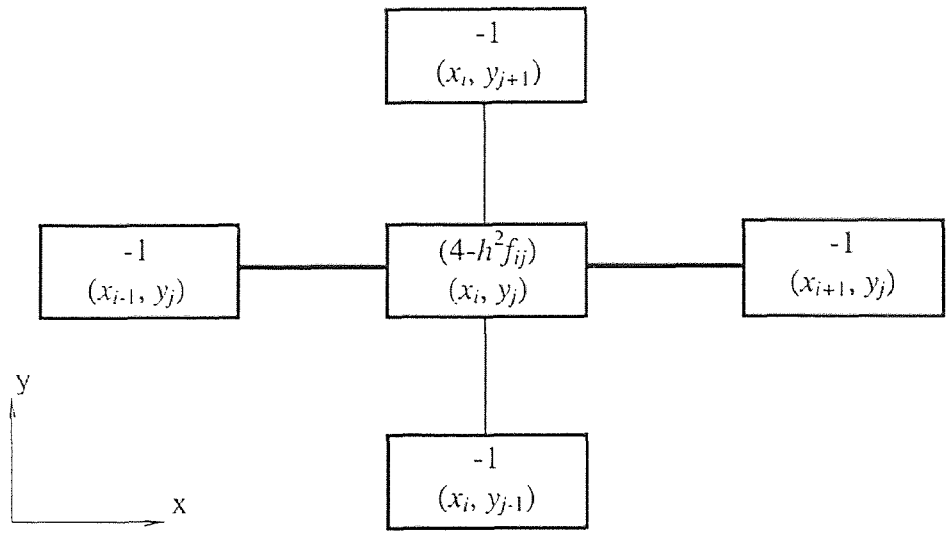

Figure B.1 Relative positions of points in the approximation of *five-point formula*

Since this approximation is made at each interior grid point, equation (B.3) gives a $[(M\text{-}1)(N\text{-}1)\times(M\text{-}1)(N\text{-}1)]$ system of equations and it can be expressed as $Av = g$

where $v = \begin{bmatrix} v_1 \\ v_2 \\ \vdots \\ v_{N-1} \end{bmatrix}$, $g = -h^2 \begin{bmatrix} g_1 \\ g_2 \\ \vdots \\ g_{N-1} \end{bmatrix}$, $v_j = \begin{bmatrix} v_{1j} \\ v_{2j} \\ \vdots \\ v_{M-1,j} \end{bmatrix}$ and $g_j = \begin{bmatrix} g_{1j} \\ g_{2j} \\ \vdots \\ g_{M-1,j} \end{bmatrix}$.

To solve this large system $Av = g$, the direct method may not be appropriate and the iterative method is the effective alternative. One can apply the Gauss-Seidel iteration method on equation (B.3) and obtains

$$\left(4 - h^2 f_{ij}\right) v_{ij}^{(n+1)} = v_{i-1,j}^{(n+1)} + v_{i,j-1}^{(n+1)} + v_{i+1,j}^{(n)} + v_{i,j+1}^{(n)} - h^2 g_{ij} \qquad \text{(B.4)}$$

where initial values $v_{ij}^{(0)}$ are initially given for all variables and the superscripts denote the iteration number.

Unfortunately convergence of this algorithm of equation (B.4) is often rather slow. One can divide equation (B.4) by $(4\text{-}h^2 f_{ij})$, add and subtract the term $v_{ij}^{(n)}$ and obtain

$$v_{ij}^{(n+1)} = v_{ij}^{(n)} + \frac{\left[v_{i-1,j}^{(n+1)} + v_{i,j-1}^{(n+1)} + v_{i+1,j}^{(n)} + v_{i,j+1}^{(n)} - \left(4 - h^2 f_{ij}\right) v_{ij}^{(n)} - h^2 g_{ij}\right]}{\left(4 - h^2 f_{ij}\right)} \qquad \text{(B.5)}$$

Since the Gauss-Seidel method is convergent, i.e. $v_{ij}^{(n+1)} \to v_{ij}$ and $v_{ij}^{(n)} \to v_{ij}$ as $n \to \infty$, the term in braces can be considered as a correction factor which approaches zero as $n \to \infty$. One can multiply this correction factor by a constant ω to accelerate the

convergence which is the idea of *successive overrelaxation* algorithm. Therefore from equation (B.5) the *successive overrelaxation* iteration is given as

$$v_{ij}^{(n+1)} = v_{ij}^{(n)} + \frac{\omega\left[v_{i-1,j}^{(n+1)} + v_{i,j-1}^{(n+1)} + v_{i+1,j}^{(n)} + v_{i,j+1}^{(n)} - \left(4 - h^2 f_{ij}\right) v_{ij}^{(n)} - h^2 g_{ij}\right]}{\left(4 - h^2 f_{ij}\right)} \qquad \text{(B.6)}$$

where the acceleration constant is within the range $1 < \omega < 2$.

The detail of the formulation and description of successive overrelaxation algorithm can be found in the articles about the numerical solution of partial differential equations like [43].

B.2 Upwinding

Upwinding is an algorithm developed from finite difference approach for finite element analysis on fluid dynamics. Because the finite element analysis by using standard Galerkin algorithm on the fluid dynamics will have difficulties of oscillatory solution when the mesh size exceeds a critical value, the result is not convergent or the accuracy of approximation is not appreciated. A detailed description of the derivation of finite element method by using the upwinding algorithm can be found in reference [44].

APPENDIX C

DATA INPUT FOR CFD *FIDAP*

The input program for CFD software *FIDAP* used in this analysis is presented in this section as shown in italic character. The description of the program follows the command line. The channel geometry setup depends on the channel type. The value of boundary conditions and initial conditions are the same for every case.

The first part is to create the domain of problem and generate the mesh and elements. It is described as following:

FIMESH(2-D,IMAX=121,JMAX=41)

Initiating the mesh generator, specifying the problem type as two-dimensional and setting the maximum node number in X and Y direction.

$XGRAD=1
$YGRAD=1
$HGRAD=1
$VGRAD=1

Setting element parameters which is used to control the element size.

POINT(SYSTEM=1)

Initiating the coordinate system command and setting the following system as system number one.

1, 1,1,1, 0 ,0
2, 1,41,1, 0 ,0.005
3, 121,41,1, 0.2 ,0.03133
4, 121,1,1, 0.2 ,0

Specifying the node coordination in the following format:

point number; I, J and K node numbers; x, y and z coordination

There are three sets of *I*, *J* and *K* node number representing the node number in the x, y z direction respectively. Because the problem is two-dimensional, the *K* node number is always 1. There are three sets of x, y and z coordination representing the coordination of corresponding *I*, *J* and *K* node respectively. The z coordination is eliminated because of two-dimensional problem.

LINE

Initiating line command and ending the coordinate system command.

1, 2, $YGRAD, 0

Connecting point 1 and 2 at ratio $YGRAD.

2, 3, $XGRAD, 0

Connecting point 2 and 3 at ratio $XGRAD.

3, 4, $VGRAD, 0

Connecting point 3 and 4 at ratio $VGRAD.

4, 1, $HGRAD, 0

Connecting point 4 and 1 at ratio $HGRAD.

SURFACE
1, 3

Initiating surface command to specify the flow domain, ending line command and selecting point 1 to 3 as the flow domain

ELEMENTS(QUADRILATERAL, NODE=9, ENTITY="fluid")
1, 3

Initiating element command, setting element type as quadrilateral of 9 nodes, ending surface command and specifying the flow domain to apply this element type.

ELEMENTS(BOUNDARY, FACE, ENTITY="topwall")
2, 3

Specifying the element type, the associated entity and the flow domain.

ELEMENTS(BOUNDARY, FACE, ENTITY="outlet")
3, 4

Specifying the element type, the associated entity and the flow domain.

ELEMENTS(BOUNDARY, FACE, ENTITY="symmetry")
4, 1

Specifying the element type, the associated entity and the flow domain.

ELEMENTS(BOUNDARY, FACE, ENTITY="inlet")
1, 2

Specifying the element type, the associated entity and the flow domain.

PLOT(MESH)

Initiating plot command to create the mesh.

END

Ending mesh generation procedure.

After completing the mesh generation, the boundary conditions, initial conditions, and several control commands must be given in order to assemble the global matrix and calculate the solution under the criteria of specified algorithm and given accuracy. It is described as following:

FIPREP

Initiating FIPREP command to setup the boundary and initial conditions and control parameters.

PROBLEM(STEADY, NONLINEAR, 2-D, TURBULENT)

Specifying the flow problem.

EXECUTION(NEWJOB)

Initiating the control and condition command for a new procedure.

ENTITY(FLUID, NAME="fluid")
ENTITY(WALL, NAME="topwall")
ENTITY(PLOT, NAME="inlet")
ENTITY(PLOT, NAME="symmetry")
ENTITY(PLOT, NAME="outlet")

Specifying the flow entity with the associated domain name.

ICNODE(UX, CONSTANT=11.536, ENTITY="inlet")

Initial velocity of incoming flow.

ICNODE(KINETIC, CONSTANT=0.13308, ENTITY="inlet")

Initial condition of turbulence kinetic energy.

ICNODE(DISSIPATION, CONSTANT=97.0955, ENTITY="inlet")

Initial condition of turbulence dissipation

SOLUTION(S.S.=300, VELCONV=0.00015, RESCONV=0.00015)

Specifying solution algorithm, maximum number of iteration and convergence tolerance for velocity and residue.

RELAX
.3 .35 0 0 0 0 .5 .5

Specifying change of relaxation coefficient u, v, K and ε used in the solution procedure.

OPTIONS(UPWINDING)

Initiating additional solution control command

UPWINDING
5 5 0 0 0 0 5 5

Initiating additional solution control command and changing the upwinding coefficient for u, v, K and ε used in the solution procedure.

POSTPROCESS

Initiating postprocess control command

VISCOSITY(K.E., CONSTANT=1.835E-5)
DENSITY(CONSTANT=1.193)

Specifying solution model, i.e. K–ε model, and giving the fluid viscosity and density.

BCNODE(UX, CONSTANT=11.536, ENTITY="inlet")
BCNODE(UY, ZERO, ENTITY="inlet")
BCNODE(KINETIC, CONSTANT=0.13308, ENTITY="inlet")
BCNODE(DISSIPATION, CONSTANT=97.0955, ENTITY="inlet")

Specifying boundary condition at the inlet plane of the channel.

BCNODE(VELOCITY, ZERO, ENTITY="topwall")

Specifying boundary condition of channel wall.

BCNODE(UY, ZERO, ENTITY="symmetry")

Specifying boundary condition of centerline of the channel

RENUMBER

Initiating optimization of element numbers for the assembly of the element matrix.

END

Ending current procedure.

CREATE(FISOLV)

Initiating global matrix generation and generating the database for iteration solution procedure.

After this database for solution is complete the solution command *FISOLV* is used to start the solution procedure.

REFERENCES

1. Copper, D. W., "Particulate Contamination and Microelectronics Manufacturing: An Introduction", *Aero. Sci. Technology*, vol. 5, pp. 287-299, 1986.

2. White, F. M., *Viscous Fluid Flow*, McGraw-Hill Inc., New York, w1991.

3. Friedlander, S. K. and Johnstone, H. F., "Deposition of Suspended Particle from Turbulent Gas Streams", *Indus. Engng. Chem.*, vol. 49, pp. 1151-1156, 1957.

4. Corn, M., "The Adhesion of Solid Particles to Solid Surfaces", *J. Air Pollution Control Assoc.*, vol. 11(1), pp. 523-528 and vol. 11(12), PP. 566-575, 1961.

5. Stukel, J. J. and Soo, S. L., "Turbulent Flow of a Suspension into a Channel", *Powder Technology*, vol. 2, pp. 278-289, 1968/1969.

6. Soo, S. L. and Rodgers, L. W., "Further Studies on the Electro-Aerodynamic Precipitator", *Powder Technology*, vol. 5, pp. 43-50, 1971.

7. Soo, S. L. and Tung, S. K., "Pipe Flow of Suspensions in Turbulent Fluid, Electrostatic and Gravity Effects", *Appl. Sci. Res.*, vol. 24, pp. 83-97, 1971.

8. Soo, S. L. and Tung, S. K., "Deposition and Entrainment in Pipe Flow of a Suspensions", *Powder Technology*, vol. 6, pp. 283-294, 1972.

9. Pich, J. J., "Theory of Gravitational Deposition of Particles from Laminar Flows in Channel", *J. Aerosol Sci.*, vol. 6, pp. 351-361, 1972.

10 Peddieson, J. Jr., "The Hydrodynamics of Dust Collection", *Proceedings of the Annual Technical Meeting of the Institute of Environmental Sciences*, 1972.

11 Peddieson, J. Jr., "Dust Collection at Moderate Void Fractions", *Proceedings of the Annual Technical Meeting of the Institute of Environmental Sciences*, 1973.

12 Wang, C., "Gravitational Deposition of Particle from Laminar Flows in Inclined Channels", *J. Aerosol Sci.*, vol. 6, pp. 191-204, 1975.

13. Eldighidy, S. M., Chen, R. Y., and Conparin, R. A., "Deposition of Suspensions in the Entrance of a Channel", *presented at ASME Winter Annual Meeting, New York*, 1976, *J. of Fluids Engng., Trans. ASME*, vol. 99, pp. 365-370, 1977.

14. Taulbee, P. B. and Yu, C. P., "Simultaneous Diffusion and Sedimentation of Aerosols in Channel Flow", *J. of Aerosol Sci.*, vol. 6, pp. 433-438, 1975.

15. Yu, C. P., and Chandra, K., "Deposition of Charged Particles from Laminar Flows in Rectangular and Cylindrical Channels by Image Force", *J. Aerosol Sci.*, vol. 9, pp. 175-180, 1978. .

16. Thiagarajan, V., and Yu, C. P., "Sedimentation from Charged Aerosol Flows in a Parallel-Plate and Cylindrical Channels", *J. Aerosol Sci.*, vol. 10, pp. 405-410, 1979.

17. Chen, R. Y., "Deposition of Aerosol Particles in a Channel due to Diffusion and Electric Charge", *J. Aerosol Sci.*, vol. 9, pp. 253-260, 1978

18. Chen, R. Y., and Gelber, M. W., "Deposition of Particles in a Parallel Plate Channel due to Electrostatic Charge, Diffusion and Gravitational Effects", *Powder Technology*, vol. 28, pp. 229-234, 1981.

19. Chen, R.Y., Pawel, H. E., and Chen, W. C., "Inertia Effect on Deposition of Charged Particles in a Parallel-Plate Channel", *Powder Technology*, vol. 38, pp. 249-253, 1983.

20. Cooper, D. W., Peters, M. H., and Miller, R. J., "Predited Deposition of Submicron Particles due to Diffusion and Electrostatic in Viscous Axisymmetric Stagnation-Point Flow", *Aerosol Sci. Technology*, vol. 11, pp. 133-142, 1989.

21. Ferziger, J. H., "Higher-level Simulations of Turbulent Flows", *Computational Methods for Turbulent, Transonic and Viscous Flows*, vol. 9, pp. 93-182, 1986.

22 Fichman, M., Gutfinger, C., and Pnueli, D., "A Model for Turbulent Deposition of Aerosols", *J. Aerosol Sci.*, vol. 19, No. 1, pp. 123-136, 1988.

23. Yu, C. P., "Theories of Electrostatic Lung Deposition of Inhaled Aerosols", *Ann. Occup. Hyg.*, vol. 29, No. 2, pp.219-227, 1985.

24. McLaughlin, J. B., "Aerosol Particle Deposition in Numerically Simulated Channel Flow", *Phys. Fluids A 1*, vol. 7, pp. 1211-1224, 1989.

25. Ramarao, B. V., and Tien, C., "Aerosol Deposition in Two-Dimensional Laminar Stagnation Flow", *J. Aerosol Sci.*, vol. 20, pp. 775-785, 1989.

26. Chen, R. Y., Hui, K. W., and Lu, C. H., "A Theoretical Study of Deposition of Charged Particles in a Convergent Channel Due to Image Forces", *Powder Technology*, vol. 61, pp. 225-229, 1990.

27. Arastoopour, H., Pakdel, P. and Adewumi, M., "Hydrodynamic Analysis of Dilute Gas-Solids Flow in a Vertical Pipe", *Powder Technology*, vol. 62, pp. 163-170, 1990.

28. Abuzeid, S., Busnaina, A. A. and Ahmadi, G., "Wall Deposition of Aerosol Particles in a Turbulent Channel Flow", *J. of Aerosol Sci.*, vol. 22, No. 1, pp. 43-62, 1991.

29. Li, A., and Ahmadi, G., "Deposition of Aerosols on Surfaces in a Turbulent Channel Flow", *Int. J. Engng Sci.*, vol. 31, pp. 435-451, 1993.

30. Chen, R. Y., Chiou, H. C., and D. Sun, "Deposition of Particles in a Convergent Channel", *Powder Technology*, vol. 87, pp. 83-86, 1995.

31. Goldberg, U. C., "Toward a Pointwise Turbulence Model for Wall-Bounded and Free Shear Flows", *J. of Fluids Engng., Trans. ASME*, vol. 116, pp. 72-76, 1994.

32. Squires, K. D. and Eaton, J. K., "Effect of Selective Modification of Turbulence on Two-Equation Models for Particle-Laden Turbulent Flows", *J. of Fluids Engng., Trans. ASME*, vol. 116, pp. 778-784, 1994.

33. Bertodano, M. L., Lahey, R. T. Jr., and Jones, O. C., "Development of a K–ε Model for Bubbly Two-Phase Flow", *J. Fluids Engng., Trans. ASME*, vol. 116, pp. 128-134, 1994.

34. Sun, D. and Chen, R. Y., "Particle Deposition on Surfaces in a Divergent Channel", *Doctoral Dissertation, New Jersey Institute of Technology, Newark, New Jersey*, 1995.

35. Graham, D. I., "An Improved Eddy Interaction Model for Numerical Simulation of Turbulent Particle Dispersion", *Gas-Particle Flows, ASME*, vol. 228, pp.161-167, 1995.

36. Soo. S. L. and Zhu, C., "Statistical Proporties of Unsteady Gas-Solid Suspension with Strong Particle-Particle Interactions in Horizontal Pipe Flows", *Powder Technology*, vol. 73, pp. 51-60. 1992.

37. Klinzing, G. E., *Gas-Solid Transport*, McGraw-Hill Inc., New York, 1981.

38. Jones, W. P. and Launder, B. E., "The Predicition of Laminarization with a Two-Equation Model of Turbulence", *Int. J. Heat Mass Transfer*, vol. 15, pp. 301-314, 1972.

39. Narashimha, R. and Sreenivasan, K. R., "Relaminarization of Fluid Flows", *Adv. Appl. Mech.*, vol. 19, pp. 221-309, 1979.

40. Sreenivasan, K. R., "Laminarescent, Relaminarizing, and Retransitional Flows", *Acta Mech.*, vol. 44, pp. 1-48, 1982.

41. Sreenivasan, K. R. and Narashimha, R., "Equilibrium Parameters for Two-Dimensional Turbulent Wakes", *J. Fluids Engng.*, vol. 104, pp. 167-170, 1982.

42. Acharya, S., Dutta, S., Myrum, T. A., and Baker, R. S., "Turbulent Flow Past a Surface Mounted Two-Dimensional Rib", *J. Fluids Engng., Trans. ASME*, vol. 116, pp. 238-246, 1994.

43. Johnson, L. W. and Riess, R. D., *Numerical Analysis*, Addison-Wesley Publishing Company, Blacksburg, Virginia, 1982.

44. Mitchell, A. R. et al, "An Upwind Finite Element Scheme for Two-Dimensional Convective Transport Equation", *Int. J. Numerical Methods Engng.*, vol. 11, pp. 131-143, 1977.